ON THE PENETRATION AND DISTRIBUTION OF DRUGS INTO BIOLOGICAL TISSUES: A MULTISCALE APPROACH

KULDEEP SINGH YADAV

DEPARTMENT OF MATHEMATICS

INDIAN INSTITUTE OF TECHNOLOGY GUWAHATI

GUWAHATI – 781039, INDIA

May, 2022

ON THE PENETRATION AND DISTRIBUTION OF DRUGS INTO BIOLOGICAL TISSUES: A MULTISCALE APPROACH

A thesis submitted

in partial fulfilment of the requirements

for the degree of

DOCTOR OF PHILOSOPHY

by

KULDEEP SINGH YADAV

(Roll No.–176123004)

DEPARTMENT OF MATHEMATICS

INDIAN INSTITUTE OF TECHNOLOGY GUWAHATI

GUWAHATI – 781039, INDIA

May, 2022

DEDICATED TO MY PARENTS

Late Rajpal Yadav

&

Ramesh Devi

Declaration

I hereby declare that the work presented in this thesis, titled "**On the penetration and distribution of drugs into biological tissues: A multiscale approach**," is accomplished under the supervision of **Dr. D. C. Dalal**, Professor, Department of Mathematics, Indian Institute of Technology Guwahati for the award of the degree of Doctor of Philosophy, and that it has not been submitted for a degree elsewhere.

May, 2022

Kuldeep Singh Yadav
Roll No. 176123004
Department of Mathematics
Indian Institute of Technology Guwahati

Certificate

It is to certify that the work contained in this thesis entitled "**On the penetration and distribution of drugs into biological tissues: A multiscale approach**" has been carried out by **Mr. Kuldeep Singh Yadav**, a student in the Department of Mathematics, Indian Institute of Technology Guwahati, under my supervision for the award of the degree of Doctor of Philosophy, and that this work has not been submitted for a degree elsewhere.

May, 2022

Dr. Durga Charan Dalal
Professor
Department of Mathematics
Indian Institute of Technology Guwahati

ACKNOWLEDGEMENTS

This thesis would not have been possible without the help of many wonderful people who were present in some way, either directly or indirectly. This is the place where I can thank at least some of them, if not all.

First and foremost, I would like to express my gratitude to Prof. Durga Charan Dalal, my thesis supervisor, for his constant encouragement and generous guidance throughout my PhD tenure. I owe him a great debt of gratitude for sharing his expertise and unwavering care throughout the process. I am truly grateful for his invaluable suggestions and foresight, which enabled me in completing this research.

I would like to take this opportunity to thank the members of my doctoral committee, Prof. Rajen Kumar Sinha, Prof. Natesan Srinivasan, and Prof. Swaroop Nandan Bora, for their valuable suggestions and insightful comments, which have truly added value to the quality of my research work at various stages. I would also like to thank Prof. S. Chandra Sekhara Rao (Department of Mathematics, IIT Delhi), my master's thesis mentor, for sparking my interest in research. I would like to express my gratitude to all of the department's staff members for their help throughout my PhD tenure.

I would like to thank Nilay Mondal and Krishan Mudgal for their easy availability for discussion and selfless valuable inputs. I would also like to thank Gopinath Sadhu, who was very helpful, especially near the thesis submission process. At the location of my unforgettable journey, I found Ashish Kesarwany, Jogen Dutta, and Ankur Kanaujiya as my elder brothers. Finally, I would like to thank Ram Manohar, Uttam, Deepak, Naresh, Raman, Monu, and Gouranga for providing a stimulating, fun-filled, and homely environment in which I spent all of my joyous moments. There are many more, but it is difficult for me to express everyone's

part here.

Mrs. Rajni, my wife, has always been there for me in times of rage and frustration, and I can not thank her enough for that. I would like to thank my mother, Mrs. Ramesh Devi, who has always been there to help and has spent her treasures believing in my success. She has accepted my long absence from my lovely home while taking care of the family during my stay here. My father, Late Shri. Rajpal Yadav, whose values are deeply ingrained in my heart and mind, even in his absence, always encouraged me. I am fortunate to have my babies, Vartika and Arpita, who have always assisted me in reducing anxiety and providing an adorable environment.

ABSTRACT

Several chemotherapeutic drugs have been developed that show significant anticancer activities during the clinical trials; however, their treatment efficacy is limited in practice. The limited efficacy may be due to the inefficient delivery of chemotherapeutic drugs to the lesion site. It may be attributed to the lack of knowledge of the interplay between the drug and physicochemical properties of tissues. Numerous approaches have been employed to improve the penetration efficacy of drug delivery systems. Still, their strategic development is hindered by the lack of mechanistic understanding and assessment of drug transport. To optimize the efficiency of a drug delivery system, a detailed understanding of pharmacokinetics is necessary.

In this thesis, a finite volume heterogeneous multiscale method (FV-HMM) is propounded to study drug transport into biological tissues by considering cell scale heterogeneity. The model is improved continuously at several stages. The partition coefficient is incorporated in the diffusion-based drug transport model as the first objective. A new upscaling technique is devised to evaluate the effective drug transport at the macro level. It is observed that the partition coefficient of a drug is an important factor that may affect drug penetration.

Next, the FV-HMM is improvised (to FVHMM-p) to incorporate the passive diffusion across the cell membrane. The permeable cell membrane treated in the microscale model incorporates the solute diffusivity, membrane thickness, and partition coefficient. The microscale model is apparently a three compartmental model; the first compartment involves the diffusion in the extracellular space, the second one, the transport across the cell membrane, and the third one, the movement due to diffusion into the intracellular space. For the microscale model simulation, a novel permeable interface method (PIM) based on the central-type finite difference discretization is developed. Further, the FVHMM-p is reconstructed to investigate

the effects of biological cell orientation on the penetration and distribution of a drug in tissues. The simulation results reveal that the biological cell orientation is an important factor, which can potentially affect the drug penetration and distribution in the tissues.

In the next objective, the FVHMM-p incorporates the fluid flow and drug metabolism effects on drug transport. On treating the tissue as a porous medium, Darcy's law is used for fluid flow, and the drug metabolism is calculated using the Michaelis-Menten equation. It is observed that the particles of sizes 10 and 100 nm can penetrate the tissue in fluid flow regions. Furthermore, local sensitivity analysis is also performed to determine the model response to the input parameters. It is observed that the parameters such as fluid velocity, extracellular diffusivity, and microscale domain size are the most sensitive to the model outcome. The proposed model is simulated to determine the impact of biological cell geometry on drug penetration into the tissue domain. The cell is considered to be of elliptical shape, and the simulations with different configurations lead to the pronounced effects on drug penetration at the tissue scale.

Finally, the last multiscale model is employed to study the tissue penetration and distribution efficacy of chemotherapeutic agents, such as fluorouracil, carmustine, cisplatin, methotrexate, doxorubicin, and paclitaxel. The physical properties of drugs are incorporated in the model to understand the effects under different situations. It is observed that carmustine penetrates deeper into the tissue, followed by paclitaxel, methotrexate, fluorouracil, doxorubicin, while cisplatin penetrates least.

LIST OF FIGURES

1.1 Leading causes of death in the United States [3]. 2

1.2 Multiscale nature of an organism [55]. 4

2.1 Schematic of a tissue domain and a simplified zoomed-version at a point **P** consists of dispersed cells. 16

2.2 Schematic of (a) a control volume (CV) with microscale domain each of on its face centre and (b) a typical microscale domain. 19

2.3 An illustration to determine the position of a microscale computational domain (ω^{e_f}) in Ω. 21

2.4 A procedure to obtain the boundary condition for the microscale model constructed at the east face of the CV (k, l). 22

2.5 Schematic representation of interfacial point $(i + \theta, j)$, for fix j. 23

2.6 (a) Construction of microscale domains at the boundary faces of respective control volumes, and (b) an illustration of the reconstruction for the boundary microscale model. 25

2.7 A pictorial summary of the FV-HMM algorithm. 26

2.8 A two-dimensional physical domain with an immersed interface Γ that divides domain (ω) into two parts: ω_E and ω_I. 26

2.9 An illustration of the regular, irregular, and interfacial grid points. 28

2.10 Schematic of Cartesian grid point i which falls in between two interfacial points $i + \theta_1$ and $i - \theta_2$, for fixed j and m. 29

2.11 Surface plots of (a) numerical solution and (b) the error for Problem 1 at time $t = 1$. 31
2.12 Surface plots of (a) numerical solution and (b) the error for Problem 2 at time $t = 1$. 33
2.13 Surface plots of (a) exact and (b) the FV-HMM solutions at time $t = 1$. 34

3.1 The geometrical setup for the problem. The arrow inside the tissue domain shows the direction of interest for drug penetration. 37
3.2 Comparison of the FV-HMM results with the experimental results and one-dimensional analytical solution. Solid line with marker represents the FV-HMM simulation result, whereas the filled circles and the dashed line represent experimental data from Wong et al. [66], and analytical solution, respectively. . 39
3.3 Effects of partition coefficient on drug penetration. (a) For fixed constant diffusion in tissue for 10 nm particles and (b) for different diffusion coefficients in intra- and extra-cellular spaces for 1 and 10 nm particles. 40
3.4 Effects of particle size on drug penetration (a) with partitioning $(K = 0.1)$ and (b) without partitioning $(K = 1)$. 41
3.5 Schematic for the microscale problem to study concentration distribution at cell scale. The cell is chosen with the parameters $a_1 = a_2 = 3.1 \times 10^{-4}$ cm. 41
3.6 Simulation results for a typical microscale model. Results (a) with partitioning $(K = 0.1)$ and (b) without partitioning $(K = 1)$. (c) The concentration distribution along the arrows drawn in (a) and (b). (d) The ratio of concentration at first two consecutive x'-irregular Cartesian grid points (on arrow) vs. time (c'_E: concentration at extracellular grid point $(0.000503, 0.000805)$ and c'_I: concentration at intracellular grid point $(0.000503, 0.000812)$). The parameters are chosen as: $r = 1$ nm, $\mu_I = 5$ cP, $\mu_E = 1$ cP, and $t' = 10^{-5}$ h. 42
3.7 Effects of cell geometry on drug penetration (a) with partitioning $(K = 0.1)$ and (b) without partitioning $(K = 1)$. (c) The concentration at point $x' = 0.1214$. (d) Schematic for the cell height and cell width. 44
3.8 Effects of (a) cell height and (b) cell width with partition coefficient $K = 0.1$. . 44
3.9 Effects of fluid viscosities on drug penetration. Intracellular fluid viscosity variation (a) with $(K = 0.1)$ and (b) without partitioning $(K = 1)$. Extracellular fluid viscosity variation (c) with $(K = 0.1)$ and (d) without partitioning $(K = 1)$. 45

4.1 The hierarchy of the computational domain to couple the microscale model to the macroscale one. (a) A typical control volume, (b) a typical microscale domain, and (c) the zoomed-version of cell membrane of width ε. 49

4.2 Schematic diagram of ω and the elliptical interface Γ. Here, I is used to showing the intracellular quantity and E for the extracellular one. 51

4.3 Treatment of drug concentration at the interfacial point. (a) Single interfacial point $i + \theta$ around i and (b) two interfacial points $i + \theta_1$ and $i - \theta_2$ surrounds Cartesian grid point i. 52

4.4 Simulation results of PIM and Miyauchi et al. [39] along with the analytical solution. The parameters are (a) $D_l = D_r = 1$, $P = 0$ and (b) $D_l = 1$, $D_r = 0.5$, $P = 0.1$. The interface is located at $x_0 = 0.5$. 55

4.5 (a) Schematic of computational domain. The three-dimensional contour plots; (b) Miyauchi et al. [39], and (d) present work (PIM). (c) The concentration distribution along the line **AB**. 56

4.6 A comparison between the PIM (left) and the IIM (right) results. 57

4.7 (a) An illustration of the tissue computational domain and (b) the schematic of a single-cell computational domain. 59

4.8 Numerical results of the FV-HMM and FVHMM-p along with the experimental results of Huang et al. [23]. 60

4.9 Comparisons of the FV-HMM ($K = 0$) and FVHMM-p (for $P = 0$) results with the choice of (a) circular and (b) elliptical cells. 61

4.10 Simulation results of 1 nm particles for equal fluid viscosity ($\mu_I = \mu_E = 2.5$ cP) in intra- and extra-cellular spaces. (a) Single-cell model and (b) tissue scale model. 62

4.11 Effects of cell permeability on penetration and distribution of 1 and 10 nm drug particles (fluid viscosity as case-II). (a) A single-cell model and (b) tissue model. (c) Concentrations against the permeability at position $x' = 0.195$. (d) Concentration distribution for 10 nm size drug particles in the tissue domain. . 63

4.12 Effects of particle size on penetration. (a) $P' = 1$ cm/h and (b) permeability (in cm/h) for respective particle is shown in the legend. 64

4.13 Effects of cell size (or extracellular spatial volume) on drug penetration. (a) Results in tissue domain for $P' = 0.1$ cm/h and (b) the concentrations at point $x' = 0.195$ for different permeability values. 65

4.14 Effects of cell height (a_2) on drug penetration. (a) Results in tissue domain for $P' = 0.1$ cm/h and (b) the concentrations at point $x' = 0.195$ for different permeability values (μ_I = 5 cP and μ_E = 1 cP). 66

4.15 Effects of cell width (a_1) on penetration. (a) Results in tissue domain for $P' = 0.1$ cm/h. (b) The concentrations at point $x' = 0.195$. 66

4.16 Effects of cell geometry on penetration. (a) Results in tissue domain for $P' = 0.1$ cm/h. (b) The concentrations against a_2 at point $x' = 0.195$. 67

5.1 Tissue image [28]. 72

5.2 Schematic of problem. 73

5.3 Schematic for the implementation of novel reconstruction operators. 75

5.4 A comparison between the (a) analytical and (b) numerical (FVHMM-p(II)) solutions on the finite volume mesh of size 20×20 at $t = 1$. 78

5.5 Grid independency results for the FVHMM-p(II) on macro-spatial grid (a) 13×13, (b) 25×25, and (c) 50×50. (d) Concentrations along the lines $y' = 0.5$ and $y' = 0.97$ from each of the contour. 79

5.6 Comparison of the FVHMM-p(II) results with the experimental values of Huang et al. [23]. 80

5.7 Contour plots for concentration distribution on application of convection boundary condition on upper and lower boundaries, (a) FVHMM-p(II) along with Eq. (5.4), (b) FVHMM-p(II) along with Eq. (5.3), and (c) MATLAB solution. . . . 81

5.8 Results for drug transport in tissue using (a) FVHMM-p(I) and (b) FVHMM-p(II) for $\phi = \frac{\pi}{4}$. 81

5.9 Prediction of concentration distribution and penetration using the FVHMM-p and FVHMM-p(II) for (a) the elliptical cell whose axes lie along with the coordinate directions ($\phi = 0$) and (b) the elliptical cell is rotated by an angle $\phi = \frac{\pi}{4}$ anticlockwise. 83

5.10 (a)–(e) Results for drug concentration distribution and penetration for various ϕ ($\kappa' = 0.01$). (f) Schematic of the cell height. 84

5.11 Drug concentrations along the lines (a) $y' = 0.05$, (b) $y' = 0.49$, (c) $y' = 0.95$, and (d) on the selected probes. 85

5.12 Concentration distribution along the cross-section $x' = 0.21$. (a) $0 \leq \phi \leq \frac{\pi}{4}$ and (b) $\frac{\pi}{4} \leq \phi \leq \frac{\pi}{2}$. 86

5.13 Drug concentration distribution and penetration with $\kappa' = 0.1$ cm/h for various values of ϕ. 87

5.14 Drug concentrations along the cross-section $x' = 0.21$ for (a) $0 \leq \phi \leq \frac{\pi}{4}$ and (b) $\frac{\pi}{4} \leq \phi \leq \frac{\pi}{2}$. (c) Drug concentrations against ϕ on the probes. 88

5.15 Drug concentrations for two different elliptical cells on probes (a) P_1, (b) P_2, and (c) P_3. 89

5.16 Drug concentrations for two different permeability values on probes (a) P_1, (b) P_2, and (c) P_3. 90

5.17 Normalized effect of the input parameters on the model output. Results with 'dashed lines' are shown for the 10% reduction in the input parameter value while 'solid lines' are for the 10% increase. These results are along the line $y' = 0.49$. 92

6.1 Schematic diagram of the tissue domain and the specified boundary conditions. 98

6.2 Stencil for the SUPERBEE upwind scheme. 99

6.3 Contour plots of (a) analytical and (b) numerical results on 20×20 finite volume mesh at time $t = 1$. 101

6.4 Validation with the experimental results of Huang et al. [23]. 101

6.5 Effects of drug particle size on its penetration and distribution for (a) $u_0' = 0.036$ cm/h and (b) $u_0' = 0$ cm/h. (c) Penetration depths of drugs observed in (a) and (b). 104

6.6 Effects of cell size on dug penetration ($u_0' = 0.036$ cm/h, $V_{max}' = 0$ M/h) for (a) $r = 1$ nm, (b) $r = 10$ nm, and (c) $r = 100$ nm. (d) Penetration depths of drugs observed in (a), (b), and (c). 105

6.7 Effects of cell height on drug penetration ($a_1 = 2.1 \times 10^{-4}$ cm, $u_0' = 0.036$ cm/h and $V_{max}' = 0$ M/h) for (a) $r = 1$ nm, (b) $r = 10$ nm, and (c) $r = 100$ nm. (d) Penetration depths of drugs observed in (a), (b), and (c). 106

6.8 Effects of cell width on drug penetration ($a_2 = 2.1 \times 10^{-4}$ cm, $u_0' = 0.036$ cm/h, and $V_{max}' = 0$ M/h) for (a) $r = 1$ nm, (b) $r = 10$ nm, and (c) $r = 100$ nm. (d) Penetration depths of drugs observed in (a), (b), and (c). 107

6.9 (a) Effects of cell membrane permeability on drug penetration ($u_0' = 0.036$ cm/h, $V_{max}' = 0$ M/h). Dashed lines '- -' show the results for $P' = 10$ cm/h while solid lines '–' display the results for $P' = 0.1$ cm/h. (b) Penetration depth for each permeability values. 108

6.10 Results of metabolism on penetration and distribution of drug (a) with no fluid flow ($u_0' = 0$) for 1 and 10 nm drug particles and (b) with fluid flow ($u_0' = 0.036$) cm/h for 1 nm particles ($V_{max}' = 1.8 \times 10^{-2}$ M/h, $K_m' = 10^{-5}$ M). . . . 109

6.11 Sensitivity of the input parameters on the model response with no advection term. The 'solid lines' display the results for 10% increase in the nominal values while the 'dashed lines' show the results for 10% reduction. 110

6.12 Sensitivity of the input parameters on the model response measured as the NSC values. (a) Results are depicted for the full proposed model and (b) results for the model with no drug metabolism term. The inset in (a) shows the zoomed-version of the results in rectangular box. The 'solid lines' display the results for the 10% increase in the nominal values while the 'dashed lines' show the results for 10% reduction. 110

7.1 Logarithmic plot of the values of the dimensionless numbers. 118

7.2 Validation of the present model results with (a) the experimental results of DOX [44] and (b) the experimental results of PTX [5]. 119

7.3 Importance of dimensionless parameter KT. 120

7.4 Penetration of chemotherapeutic drugs on various fluid velocity. (a) $u_0' = 0$ cm/h, (b) $u_0' = 0.01$ cm/h, (c) $u_0' = 0.036$ cm/h, and (d) $u_0' = 0.06$ cm/h. (e) Penetration depths. 121

7.5 Comparison of penetration of chemotherapeutics with and without elimination. Solid lines '–' show the results with elimination while dashed lines '- -' without elimination. 122

7.6 Penetration depths of drugs with and without advection. Solid lines '–' show the results with elimination while dashed lines '- -' without elimination. 123

7.7 Effects of cell geometry on drug penetration ($u_0' = 0$ cm/h). 125

7.8 Effects of cell height on drug penetration ($u_0' = 0$ cm/h, $a_1 = 2.1 \times 10^{-4}$ cm). . 126

7.9 Effects of cell width on drug penetration ($u_0' = 0$ cm/h, $a_2 = 2.1 \times 10^{-4}$ cm). . 128

7.10 Effects of cell size on drug penetration ($u_0' = 0.06$ cm/h). 129

7.11 Effects of cell geometry on drug penetration ($u_0' = 0.06$ cm/h). 130

LIST OF TABLES

2.1 Error analysis for the IIM ($\delta x = \delta t = 1/2^s$). 33

2.2 Maximum error estimates for the FV-HMM (Problem 3). 34

4.1 Maximum error estimates and the orders of convergence for the PIM. 58

4.2 Maximum error estimates on macro-spatial grid refinement for the FVHMM-p. 59

5.1 Maximum error estimates ($||E_h||_\infty$) for the FVHMM-p with the type I and type II reconstruction operators and for the FV-HMM. 78

6.1 Maximum error estimates for the macro-spatial grid refinement. 100

6.2 Values of the physical parameters. 102

7.1 Values of the parameters for chemotherapeutic drugs. 117

7.2 Dimensionless numbers. 118

NOMENCLATURE

Superscripts

$\cdot'$	Dimensional quantity
$\tilde{\cdot}$	Characteristic variable

Notations

Ω	Macroscale domain
$\partial\Omega$	Macroscale domain boundary
ω	Microscale domain
$\partial\omega$	Microscale domain boundary
ω_I, ω_E	Microscopic intra- and extra-cellular spaces, respectively
τ	Stipulated time frame
∇	Gradient operator
λ	Edge length of the microscale domain
Γ	Cell membrane (interface)
μ	Fluid viscosity
μ_I, μ_E	Intra- and extra-cellular fluid viscosities, respectively
$\delta x, \delta y$	Microscopic spatial-step sizes in x- and y-directions, respectively
δt	Microscopic time-step size
ε_{tol}	Tolerance parameter
ε	Cell membrane width
ϕ	Orientation angle of the cell
Δt	Macroscopic time-step size
a_1, a_2	Horizontal and vertical axes lengths of the ellipse, respectively

c	Microscopic concentration of the drug
c_I, c_E	Microscopic concentrations of the drug in intra- and extra-cellular spaces, respectively
C	Macroscopic concentration of the drug
C_0	Initial macroscopic concentration of the drug
C_∞	Concentration in the exterior to the tissue domain
$\mathbf{D}$	Molecular diffusion tensor (at micro level)
D	Molecular diffusion scalar (at micro level)
D_I, D_E	Molecular diffusion coefficients in intra- and extra-cellular spaces, respectively
D_m	Transmembrane molecular diffusion
D_{eff}	Effective molecular diffusion at macroscale
e_f, w_f, n_f, s_f	East, west, north, and south faces of the control volume, respectively
$\mathbf{F}$	Macro flux vector (F_x, F_y)
F_x, F_y	Components of the macro flux ($\mathbf{F}$) in x- and y-directions, respectively
h	Macroscopic spatial-step size
$\mathbf{I}$	Identity matrix
i, j	Indices of the microscopic Cartesian spatial grid in x- and y-directions, respectively
J	Index set
K	Partition coefficient
$\mathbf{K}$	Permeability tensor of tissue
k_D	Darcy's coefficient
k, l	Indices of macroscopic spatial grid in x- and y-directions, respectively
k_B	Boltzmann's constant
κ	Mass transfer coefficient
L	Length scale
M_x, M_y	Number of microscopic grid points in the x- and y-directions, respectively
N	Macroscopic grid points in the both x- and y-directions
$\mathbf{n}$	Outward unit normal vector to the cell membrane
$\mathbf{n_t}$	Outward unit normal vector to the tissue domain
P	Cell membrane permeability
r	Radius of the solute/drug particle
t	Time
T	Temperature
u, v	x- and y-components of the velocity vector ($\mathbf{v}$), respectively
$\mathbf{v}$	Velocity vector (u, v)

x	Spatial position vector (x, y)
x, y	Spatial coordinate variables

Units

μs	Microsecond
ms	millisecond
s	second
fs	femtosecond
h	hour
nm	Nanometre
cm	centimetre
M	Molar
cP	Centipoise

Abbreviations

1D	One-dimensional
2D	Two-dimensional
ABM	Agent-based modelling
ADI	Alternating direction implicit method
BCNU	Carmustine
BiCGSTAB	Biconjugate gradient stabilized method
BiCGSTAB(II)	Biconjugate gradient stabilized method II
CG	Coarse-grained
CIS	Cisplatin
CPI	Coarse projective integration
CV	Control volume
DOX	Doxorubicin
DPD	Dissipative particle dynamics
QM	Quantum mechanics
DNA	Deoxyribonucleic acid
EFM	Equation-free method
FDHMM	Finite difference heterogeneous multiscale method
FU	Fluorouracil
FV-HMM	Finite volume heterogeneous multiscale method

FVHMM-p	Finite volume heterogeneous multiscale method for permeable membrane
GTS	Gap-tooth scheme
HMM	Heterogeneous multiscale method
IBM	Immersed boundary method
IIM	Immersed interface method
Ka	Karlovitz number
MD	Molecular dynamics
MTX	Methotrexate
NHM	Numerical homogenization method
NSC	Normalized sensitivity coefficient
PD	Patch dynamics
Pe	Peclet Number
PIM	Permeable interface method
PTX	Paclitaxel
QC	Quasi-continuum
SSOR	Symmetric successive over-relaxation
Th	Thiele modulus
TIP	Tumour interstitial fluid pressure

CONTENTS

Abstract **ix**

List of Figures **xvii**

List of Tables **xix**

Nomenclature **xxv**

1 Introduction **1**

1.1 Overview: drug delivery 1

1.1.1 Multiscale nature of biological tissue 3

1.2 Mathematical modelling 4

1.2.1 Continuum models 5

1.2.2 Microscale models 6

1.3 Multiscale modelling 7

1.3.1 Equation-free multiscale method 9

1.3.2 Heterogeneous multiscale method 10

1.3.3 Homogenization techniques 11

1.4 A suitable multiscale approach for drug delivery 11

1.5 Thesis objectives 12

1.6 Organization of the thesis 12

2 Finite volume heterogeneous multiscale method **15**

2.1 Model formulation 15

2.2 Finite volume heterogeneous multiscale method 17
2.2.1 Choice of macro solver 17
2.2.2 Set-up of microscale model 18
2.2.3 Simulation of microscale model 22
2.2.4 Estimation of macro flux 22
2.2.5 Evaluation of boundary flux 24
2.2.6 Evolution of macroscopic equations 24
2.2.7 Summary of the FV-HMM algorithm 24
2.3 Immersed interface method 25
2.3.1 Model formulation 25
2.3.2 Numerical method 27
2.4 Numerical validation 30
2.4.1 IIM 30
2.4.2 FV-HMM 32
2.5 Conclusions 34

3 Effects of particle size and partition coefficient 35
3.1 Model problem 36
3.2 Results and discussion 38
3.2.1 Validation with the experimental results 38
3.2.2 Effects of partition coefficient and drug particle size 38
3.2.3 Effects of cell geometry 42
3.2.4 Effects of fluid viscosity 43
3.3 Conclusions 46

4 Effects of cell permeability on drug delivery 47
4.1 Model formulation 48
4.1.1 Microscale model 48
4.1.2 Simulation of microscale model 50
4.2 Permeable interface method 51
4.2.1 Model formulation 51
4.2.2 Numerical method 51
4.3 Numerical experiments 54

4.3.1 PIM . . . 54
4.4 Results in drug delivery . . . 58
4.4.1 Convergence and validation . . . 59
4.4.2 Effects of cell membrane permeability . . . 61
4.4.3 Effects of drug particle size . . . 64
4.4.4 Effects of cell geometry . . . 64
4.5 Conclusions . . . 68

5 Effects of cell orientation on drug delivery 71
5.1 Model formulation . . . 72
5.1.1 Reconstruction operator . . . 73
5.1.2 Estimation of macro flux . . . 77
5.2 Results and discussion . . . 77
5.2.1 Numerical convergence and comparison with the FV-HMM . . . 77
5.2.2 Grid independency . . . 78
5.2.3 Validation with the experimental results . . . 80
5.2.4 Convection boundary condition . . . 80
5.2.5 Type-I versus type-II operators . . . 82
5.2.6 Old versus new reconstruction operators . . . 82
5.2.7 Effects of cell orientation . . . 83
5.2.8 Effects of cell dimensions and cell permeability . . . 89
5.3 Sensitivity analysis . . . 91
5.4 Conclusions . . . 92

6 Effects of fluid flow and drug metabolism 95
6.1 Model formulation . . . 96
6.2 Solution procedure . . . 98
6.3 Numerical convergence and validation . . . 99
6.3.1 Convergence of the method . . . 99
6.3.2 Validation with the experimental results . . . 100
6.4 Effects of fluid flow and drug metabolism . . . 102
6.4.1 Effects of drug particle size . . . 102
6.4.2 Effects of cell geometry . . . 103

6.4.3 Effects of permeability . . . 106
6.4.4 Effects of drug metabolism . . . 107
6.5 Sensitivity analysis . . . 108
6.5.1 Sensitivity of the parameters without advection . . . 109
6.5.2 Sensitivity of the parameters with advection . . . 109
6.6 Conclusions . . . 111

7 Penetration and distribution of chemotherapeutics 115
7.1 Model formulation . . . 116
7.2 Results and discussion . . . 116
7.2.1 Validation . . . 118
7.2.2 Importance of KT number . . . 119
7.2.3 Effects of fluid flow . . . 120
7.2.4 Effects of drug elimination rate . . . 123
7.2.5 Effects of cell geometry . . . 124
7.3 Conclusions . . . 128

8 Conclusions and future scope 133
8.1 Conclusions . . . 133
8.2 Future scope . . . 135

Bibliography 144

Publications xxviii

CHAPTER 1

INTRODUCTION

1.1 Overview: drug delivery

In the human body, *disease, defined as the abnormal condition of the organism excluding external injury*, is either prevented or cured with the help of therapeutic agents. *A therapeutic agent or a drug is a chemical compound that leads to some specific physiological changes in the organism upon its administration.* A drug is delivered to the infected cells or tissues to obtain the best possible efficacy with minimum adverse effects to the healthy cells. The delivery faces several biophysical barriers such as mucus barrier, blood circulation barrier, and the cell membrane barrier, to name a few [50]. The situation is more complicated in the case of tumour tissues, where vasculatures become leaky and tortuous, as compared to that of the healthy tissues. Elevated tumour interstitial fluid pressure (TIP) has been identified as one of the culprits that impedes effective cancer treatment. This elevation of TIP can be attributed to several pathophysiological factors include abnormalities in tumour vasculatures, lack of proper lymphatic vessels, and rapid proliferation of tumour cells within a confined space [21]. Unlike normal tissues, cells in tumour proliferate faster than the formation of vasculatures, resulting in chaotic supply of blood and other important constituents.

Several routes, such as oral, parenteral, topical, and enteral, have been identified for drug administration. The choice of a route depends on the exposure to the diseased site to get the best possible treatment efficacy. Thereby drug delivery has become a central theme in pharmaceutical sciences. As the nanotechnology has been growing, nanoparticles are being made to achieve the targeted drug delivery by overcoming the biophysical barriers that hinder

the delivery to the lesion site. Pharmacokinetics can be regulated properly by altering drug's chemical structure or changing its formulation. Traditionally, formulations are developed to solubilize medications or increase their bioavailability. *Bioavailability of a drug refers to the fraction of a dose that enters the systemic circulation.* Nanoparticle formulations are utilized to alter the drug absorption, distribution, metabolism, excretion, and toxicity (ADME-Tox). *The term absorption means the drug movement in bloodstream after administration. Metabolism is a process of reactions of a drug with the enzymes while the elimination is the removal of a drug from the body. Toxicity is defined as the measure of adverse effects of a drug to the healthy cells.*

Despite the success in nanomedicine, therapeutic effects of a drug are not clearly understood in chronicle diseases, such as cancer, which has been affecting human lives severely. According to the data shown in Fig. 1.1, cancer is the second most leading cause of death in the United States [3]. One of the main reasons is found to be the lack of specific delivery of anticancer drugs to the tumour site.

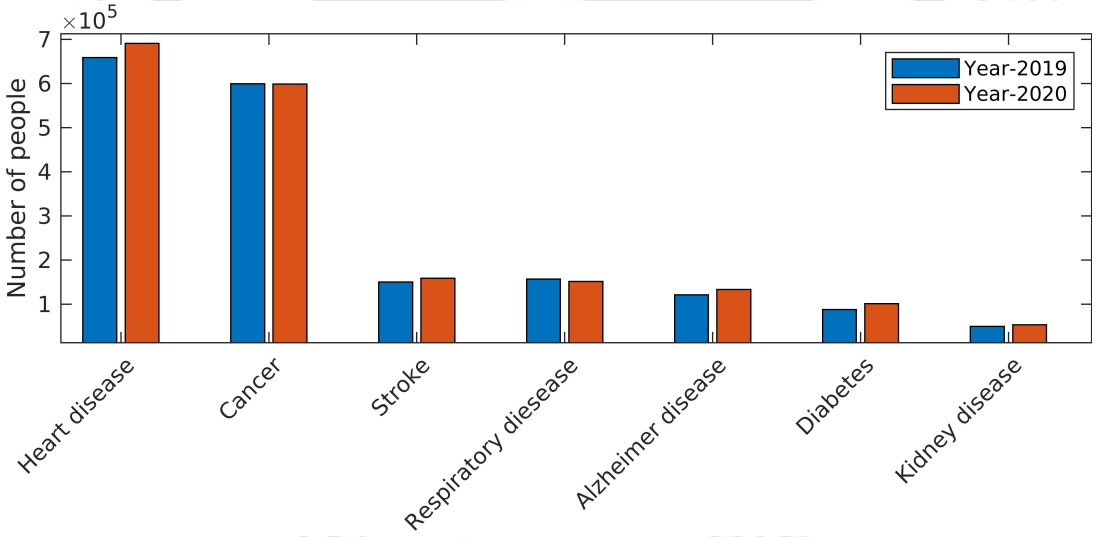

Figure 1.1: Leading causes of death in the United States [3].

The efficacy of a drug is often related to its concentration at the site of action. As a result, the correlations between drug concentrations and their pharmacological responses determine the patient health condition [47]. A drug is delivered through tumour's tortuous and leaky vasculatures, extravasate into the interstitial space, and penetrates multiple layers of cells to reach the cancer cells in a cytotoxic concentration. Thus, it is worthwhile to monitor drug distribution into the tissue with a goal of determining penetration into the lesion site. Therefore, drug penetration and distribution have become pivotal concept of pharmacokinetics and form

a base for pharmacodynamic or therapeutic effects at a later stage after the delivery of drug. *Pharmacokinetics is the study of what the biological system does to a drug (e.g., absorption, metabolism, and elimination) while pharmacodynamics is the study of what a drug does to the biological systems (e.g., therapeutic effects of a drug).*

The cytotoxic concentration involves an important factor, drug *penetration depth, which is defined as the depth from a capillary at which the minimum concentration (required for a treatment) is achieved*. Thus, the investigation of drug penetration depth in solid tumours is important for chemotherapy. The present thesis specifically focuses to explore the penetration depth of a drug and the biophysics behind the resulting penetration.

Over the years, various methods, such as *in vivo*, *in vitro*, and *in silico*, have been developed to examine drug delivery. *In vitro studies are performed on cells in confined test tubes within laboratories; whereas, in vivo studies are performed inside the living organisms itself.* For ethical reasons, studies are frequently conducted in *in vitro* first. *In vitro* investigations allow a material to be investigated without exposing humans or animals to their potential adverse effects or toxicity. Experimental techniques, that include *in vitro* and *in vivo*, are the preferred ones used to determine the penetration and distribution efficacy of a drug in tissues.

In general, the first-stage drug safety and efficacy are determined through the animal populations, and it may display variations from one animal to the other [36]. Also, in addition to the animal tissues, drug testing is performed in human tissues. However, the effects of several factors such as age, gender, diet, environment, and disease could potentially alter the experimental findings significantly [25, 35]. Though experiments are the fundamental methods to determine the potent drugs but are extremely expensive, as several experiments are needed to understand the outcome behaviour. The quantitative understanding of drug delivery can not be obtained readily from experimental studies. Also, it is difficult to understand how the biophysical and biochemical barriers do affect the drug delivery. Thus, experimental models are not appropriate, as the primary tool, for the study of penetration and distribution efficacy of a drug in biological tissues.

1.1.1 Multiscale nature of biological tissue

The biological tissues are heterogeneously complex owing to the involvement of disparate temporal and spatial scales [12, 55]. The homeostasis state of the biological systems is closely coupled with the biophysical and biochemical processes occurring at these scales. Spatial scale,

in the living organism, varies from characteristic length of an atom to that of an organism, and biochemical interactions occurring at atomic and molecular levels happen in time-scale ranging from μs to ms.

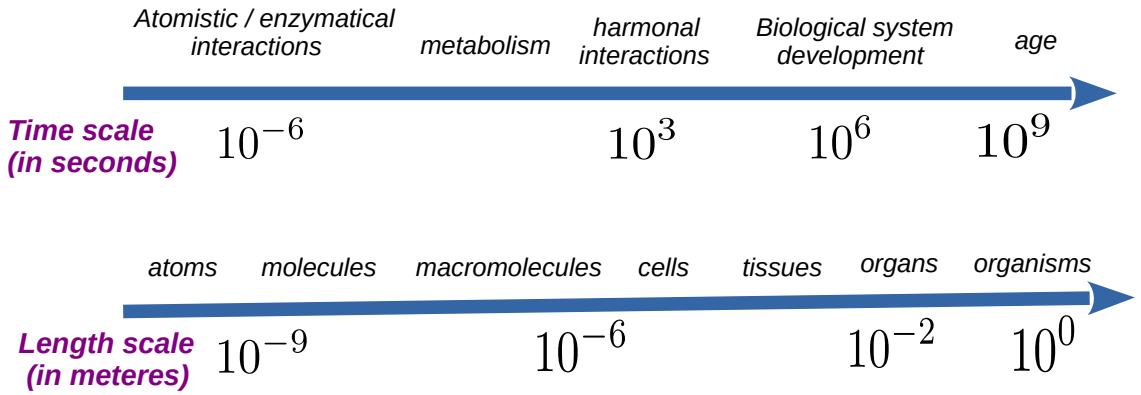

Figure 1.2: Multiscale nature of an organism [55].

In the reference [55], the authors have distinguished the characteristic length and temporal scales (depicted in the Fig. 1.2) as follows:

- At the tissue scale, characteristic length and time scales are selected in centimetres and tens of second, respectively, so that the heterogeneity can be recognized.
- The characteristic length and time scales of the processes at the extracellular space are measured in millimetres and seconds, respectively.
- The characteristic length and time scales at the cellular level can be considered in micrometres and milliseconds, respectively.
- At the subcellular level, characteristic length and temporal scales are chosen at hundreds of nanometres and microseconds, respectively.

1.2 Mathematical modelling

Owing to the massive computational tools made available in recent times, mathematical models become instrumental in describing several situations, which are usually very expensive and take ample time for the actual experiments. Mathematical models, which complement experimental studies, have become popular and convenient alternatives. These allow to predict and describe

the understanding of biological processes in a quantitative way to work out the efficiency of a treatment as well as the efficacy of a drug with wide range of parameters.

Now-a-days, mathematical models are widely used to study drug delivery [29, 40, 69]. Models, in general, can be categorized as: microscale models, continuum models (at tissue scale), and the multiscale models. The choice among the models depends on the desired information and the scale of interest.

1.2.1 Continuum models

The model at the tissue scale that average out the effects of all the heterogeneities, such as cells, micro-blood vessels, and extracellular space, can be classified as continuum model. Researchers have developed continuum models in one or other way [29, 54, 62, 64]. The governing mass-balance equation that models drug transport at the continuum (tissue) level is used as,

$$\frac{\partial C(t,x,y)}{\partial t} = \nabla \cdot (D\nabla C) - \nabla \cdot (C\mathbf{v}(t,x,y)) - \alpha C - \beta C + \gamma. \tag{1.1}$$

The left-hand-side represents the local temporal change in drug concentration, C. On the right-hand-side, the first-term accounts for the molecular diffusion of the drug with diffusivity D, the second-term accounts for the advection with the Darcy's velocity $\mathbf{v}(t,x,y)$ obtained from Eq. (1.2), third-term takes care of decay or deactivation of the drug with decaying rate α, the next one incorporates the cellular uptake with rate β, and the last-term for the rate of supply.

In most of the literature, tissue domain is treated as a porous medium, and the biological fluid is considered as the Newtonian one. By neglecting momentum exchange between the fluid phase and solid one (cellular phase), the Darcy's law used to model fluid flow is defined as [27, 70],

$$\mathbf{v} = -\frac{\mathbf{K}}{\mu}\nabla P, \tag{1.2}$$

where $\mathbf{v}$, the fluid velocity, is known as the Darcy's velocity, μ denotes the dynamic viscosity, $\mathbf{K}$ is a tensor that accounts for the permeability of the porous medium, and P denotes the fluid pressure. The term $\frac{\mathbf{K}}{\mu}$ is known as the Darcy's coefficient, denoted by k_D.

The Darcy's law originally established for laminar flow in saturated granular media under steady-state flow regimes, and the fluid was considered to be homogeneous, isothermal, and incompressible [65]. However, owing to the averaging character, the Darcy's law is used for many situations other than the basic assumptions. Nevertheless, for complex heterogeneous porous

media particularly in large domains, determining the Darcy's coefficient remains a challenge due to the significant efforts required in generating internal microstructures.

Continuum models are very efficient for drug delivery applications on scales larger than the cellular scale. However, molecular details can not be traced with this approach as the parameters are usually taken to be constant and simplified constitutive relations are used. The coefficients are estimated from the observations, but they are model specific. Also, the estimation of these coefficients to capture the heterogeneity with full-resolution in large domains is not feasible with the present technology.

1.2.2 Microscale models

The models used to study information at the scales smaller than the tissue scale can be categorized as the microscale models. The models include, but not limited to, molecular dynamics (MD), dissipative particle dynamics (DPD), ab-initio quantum mechanics (QM), and coarse-grained (CG) molecular simulations [26, 71]. Typically, the time-scale for microscale models ranges from femtoseconds (fs) to milliseconds (ms) while length scale from Angstroms to millimetres.

The QM approaches resolve the atomic and subatomic levels, which hardly matter for drug delivery investigations at the tissue scale. In the MD, trajectories of individual particles are traced out, and the time and length scales are limited to tens to hundreds of nanoseconds and tens of nanometres, respectively. However, the important biological processes occur above these length scales (above than that of the membrane width) could not be resolved with this technique. The coarse-grained simulations are suitable for modelling interactions among biomolecules, nanoparticles, cell membranes, and extracellular matrix, and reduce the computational cost significantly by lowering degrees of freedom associated with the force fields. The scale can be enhanced to 10^1 fs with CG as compared to that of the 10^0 fs associated with MD calculations. DPD method is another choice, which is similar to CG molecular dynamics, and resolves the mesoscale.

Note that the microscale models offer the possibility of rigorous studies at the cellular scale and at tumour micro-environment levels. These models have been replacing the real experiments with great accuracy on advancing the technology. However, these models are computationally expensive and take enormous time, and thus, are not viable for tissue scale studies.

1.3 Multiscale modelling

Majority of the literature are focused to single-scale modelling, which resolves the processes of that underlying scale only. In some cases, a coarse-scale model (such as the Navier-Stokes equations and a reaction-diffusion system) can accurately capture the physics of the problem by using general principles of conservation (e.g., mass, momentum, and energy) closed through phenomenological constitutive equations. However, in systems, such as non-Newtonian fluid flow, porous media transport, and neural systems, formulation of explicit closure relations may be impossible or unfeasible without simplifying assumptions. This motivation led to the goal of developing a model that can resolve microscopic information to the tissue scale for biological applications. Furthermore, the thesis aims to develop a model that is accurate as close to the microscale models and efficient as much as the continuum models.

Multiscale modelling simulates the behaviour of complex systems by coupling several spatial and temporal scales. Many multiscale approaches have been developed in different fields of research during last three decades to fulfil the above demand [1, 10, 12, 30, 31, 33, 61]. The strategies can be classified as either continuous or discrete based on the procedure used to integrate the various scales. Historically, continuous techniques have been used to determine the exact behaviour of macroscopic systems, such as fluids and solids, subject to physical principles. The continuum techniques often express the link between system attributes as continuous mathematical equations, which are solved numerically under a variety of scenarios. Most of the time, these equations are mean-field approximations that combine the results of lower-level interactions into a higher-level equation. Unlike the continuum technique, discrete approach models a complex system by explicitly expressing the discrete units and their interactions at the lower level, rather than attempting to summarize low level attributes in a continuous function. The discrete strategy is suitable for complex systems, such as social, financial, economic, and biological systems, which are made up of diverse units such as persons or cells whose behaviours are difficult to link to macro-level results. Agent-based modelling (ABM) is one such kind of approaches. Both methodologies, continuous or discrete, have advantages and disadvantages, and which one to be used is determined by the biological concern being addressed. The present thesis focuses on drug delivery, which has been explored using the continuum mass-balance model over the years; so, the continuous approach is a suitable candidate.

The modelling of heterogeneous complex tissues should consider the different relevant scales (those discussed in Section 1.1.1) to have a realistic and proper idea of the behaviour of

biological systems [12, 55]. It requires appropriate multiscale algorithms to get the behaviour at macro level [12]. Some attempts have been made to model the mass transport processes in the biological tissues incorporating multiscale features [4, 24, 53]. In literature, the models have considered the cells as solid spheres even though the interior of cells can play a significant role in the transport of drug into the interstitial space. Ambrosi et al. [4] developed a bottom-up multiscale approach starting from the micro scale and upscaling to the macro scale was done through a one-way coupling. The model was used to determine the absorption rate of nanoparticles by upscaling unit cell drug uptake efficacy to the macroscopic model. Kojic et al. [30] developed a multiscale molecular dynamic finite element method based on a procedure known as the numerical homogenization method (NHM). This model is a bottom-up approach that upscales the microscopic effects to the macroscale through the effective parameters. They used the NHM to study mass transport into the biological tissues [31].

In most of the available multiscale models, the effective coefficients are calculated from a single-cell model (termed as Happel's sphere) and are used directly at the tissue scale model [4, 53]. Also, the models are problem specific. The literature still lacks robust models that have incorporated complex biological processes and tissue heterogeneity to provide insights of microscopic events to the tissue scale [55, 71]. The upscaling techniques that can be used to exchange the information back and forth among the models at different scales need to be understood in terms of biological applications.

To model biological processes, multiscale modelling can be employed mainly in two ways: 'top-down' and 'bottom-up'. In a top-down strategy, modelling starts at the macro level, and the data required for macro model are obtained from the micro scale. In the latter strategy, mathematical modelling starts from the micro model, and the macroscopic behaviour is obtained by some appropriate averaging of the micro model outcomes. Another growing approach is the 'middle out' strategy, which begins with an intermediate scale (typically the biological cell) and gradually stretched to cover both smaller and larger spatial scales.

The well-known multiscale techniques include the quasi-continuum (QC) method, equation-free method (EFM), heterogeneous multiscale methods (HMM), and the asymptotic homogenization approach. The QC approach is restricted to the scales smaller than the cellular scale owing to the atomistic simulations. It can be used to simulate the biological processes of the mentioned scale, if required. The EFM, HMM, and homogenization are the potential approaches for drug delivery.

1.3.1 Equation-free multiscale method

EFM is a multiscale framework that allows macroscopic descriptions that emerge from microscopic descriptions [17]. If the macroscopic evolution equations are not readily available, the EFM technique can be used. In the EFM, the macroscopic modelling activities, which generate data over long time scales and large spatial scales, are carried out by making properly initialized calls to the micro simulator for only short time and in small spatial domains. This method combines the following approaches: coarse time stepper, coarse projective integration (CPI), gap-tooth scheme, and patch dynamics.

For illustration, consider $\mathcal{V}$ and $\mathcal{U}$ are the microscopic/detailed and macroscopic fields, respectively. The procedure coarse time stepper consists of lifting, microscale simulation, and restriction. Lifting is used to construct the microscopic field from the given macroscopic one as,

$$\mathcal{V} = \mathcal{C}\mathcal{U}, \tag{1.3}$$

where $\mathcal{C}$ is a lifting operator.

Once the microscale field is constructed, the microscale simulation is carried out to relax the system to the equilibrium state, and the results are used to obtain the macroscopic field using the restriction as,

$$\mathcal{U} = \mathcal{R}\mathcal{V}, \tag{1.4}$$

where $\mathcal{R}$ is a restriction operator. Then, CPI advances the obtained macroscopic field to the larger macro-time step.

The gap-tooth scheme (GTS) exploits scale separation. In this scheme, the microscopic simulations are performed in small boxes that are large enough to capture the heterogeneity; however, smaller than the macroscopic spatial grid size. The patch dynamics (PD) approach combines the CPI and GTS techniques to perform numerical simulations of an unavailable macroscopic equation on macroscopic time and length scales. PD computes microscale dynamics on small patches, which are then used to predict the macroscale behaviour. The calculated microscale solution is extended into the buffer region around each patch to define the patch boundary condition. A patch is a small domain (a “box” or “tooth”), which is created for a short period of time.

1.3.2 Heterogeneous multiscale method (HMM)

The HMM, a top-down approach, provides a general framework to construct multiscale algorithms [61]. The general philosophy of the HMM is to solve macroscale model by extracting the missing data from microscale model. The algorithm starts at the macro scale and uses microscale models as the supplement for the missing data. The basic algorithm of heterogeneous multiscale methodology can be outlined as follows:

1. A macroscale model is formulated at the macro level based on the physics of the problem under consideration. The constructed macroscale model may be incomplete in some sense (e.g., constitutive relations may be missing) and requires additional data for its completion. The additional data may be termed as missing information.

2. An appropriate solver is chosen to solve the macroscale model.

3. The missing information is determined in the following two steps:

   (a) A microscale model constrained by macroscopic state variables is constructed.

   (b) The microscale model simulation results are used for the evaluation of missing information.

The general framework of the HMM can be described symbolically as follows. Consider the relation for macroscale model is given as,

$$\mathcal{F}(\mathcal{U}, \mathcal{D}) = 0, \tag{1.5}$$

where $\mathcal{U}$ is the macroscopic state variable, and $\mathcal{D}$ denotes the unknown data to be determined for completing the macroscale model. In order to solve macro model, one requires the missing information $\mathcal{D}$, which is extracted using the microscale model that can be written as,

$$f(\mathcal{V}, d) = 0, \quad d = d(\mathcal{U}), \tag{1.6}$$

where $\mathcal{V}$ is the microscopic state variable, and d is the data needed to set-up the microscale model. The term $d(\mathcal{U})$ denotes that the microscale model is constrained by the macroscopic state variable $\mathcal{U}$; in other words, it ensures consistency between the models.

The HMM framework has been used in many applications and found to produce accurate results [1, 2, 10, 61]. The HMM algorithm was employed to develop finite difference heterogeneous multiscale method (FDHMM) to solve parabolic differential equations which involve

multiscale diffusion coefficient [1]. Later, it was used by Chen and Ren [10] to solve the Richards' equation and also to study the transient unsaturated water flow in random porous structures.

Although, the HMM is widely used, but it has some inherent implementation difficulties. The HMM is solely based on the presumed macroscale model. So, in case, the macroscale model is constructed incorrectly, the resulted procedure can produce inaccurate results. The HMM requires a complete set of macro-state variables as its initial state. At every macroscopic iteration, it needs back and forth conversion between macro and micro states of the system.

1.3.3 Homogenization techniques

Homogenization techniques are also used to model fluid flow and drug transport in biological tissues [8, 11, 40, 52]. It helps to develop a computationally tractable macroscale model, which encompasses the microscale features. The macroscale model is composed of the effective coefficients that are derived from the microscale cell problem resolving the smaller scale processes. Homogenization techniques rely on local microscopic periodic structures, which are resolved using the cell problem to derive the macroscopic effective parameters. Scale separation, in the length scales between the macro and micro levels, is required for asymptotic expansion in the homogenization procedure.

1.4 A suitable multiscale approach for drug delivery

A good multiscale method relies purely on the micro scale and does not require a priori assumptions about the macroscale model's structure. Clearly, a possible strategy ought to be a bottom-up one. On the other hand, the top-down strategy is compromised of idealism and practicality. Researchers often suggest the top-down approaches for biological applications [12, 71]. The HMM is one of the top-down strategies, which offers a middle ground between idealism and actuality. It is, in some ways, the simplest approach to convert the sequential multiscale strategy to a concurrent one. In this thesis, the HMM framework is adopted to deal with the proposed problems.

1.5 Thesis objectives

This thesis aims to study tissue penetration and distribution efficacy of drug nanoparticles. The transport determinant biological processes such as diffusion, advection, and drug elimination are considered. As biological tissues consist of large number of cells and the extracellular space (the space outside the cells), it is difficult to extract tissue's structural information and apply a mathematical model to study drug delivery. So, mathematical modelling is proposed in the HMM framework to include the cellular heterogeneity of the tissue. The objectives of this work are listed as follows.

- A finite volume heterogeneous multiscale method (FV-HMM) is propounded to model drug transport by considering cell scale heterogeneity in the biological tissue.
- Firstly, the diffusion process along with the partition coefficient across the cell membrane are considered in the model to analyse the effects of particle size on tissue penetration and distribution efficacy of a drug.
- The FV-HMM is extended to incorporate the passive diffusion across the cell membrane (FVHMM-p). The selective permeability of the membrane is treated in the microscale model through the permeable interface condition that incorporates the solute diffusivity, membrane thickness, and the partition coefficient.
- The effects of cell orientation on tissue penetration and distribution of a drug are investigated. Furthermore, the local sensitivity analysis is performed to determine the most sensitive input parameter to the model output.
- Further, the FVHMM-p is comprehended with the advection and drug metabolism terms to analyse the effects of these processes on drug delivery.
- As the subsequent objective, the modified FVHMM-p is employed to study penetration and distribution efficacy of chemotherapeutic agents, such as fluorouracil, carmustine, cisplatin, methotrexate, doxorubicin, and paclitaxel.

1.6 Organization of the thesis

The thesis is organized as follows.

- In **Chapter 2**, the FV-HMM is propounded for the application of drug delivery. A model is developed to deal with the transport in microscale model composed of a biological cell. Numerical experiments are performed with the model problems to test the robustness of the proposed method.

- In **Chapter 3**, the FV-HMM is employed to study drug delivery, where the effects of particle size and partition coefficient on the penetration and distribution efficacy of drug delivery nanoparticles are studied.

- The FV-HMM is extended in **Chapter 4** to the FVHMM-p to incorporate the passive diffusion of a drug across the cell membrane. The permeable interface method has been proposed to deal with the mass transfer across the permeable membranes. Numerical experiments are conducted to understand the effects of particle size, cell membrane permeability, and other parameters in the model on drug penetration and distribution efficacy of drug particles in biological tissues.

- The fluid flow and drug metabolism are also incorporated in the FVHMM-p, and it is discussed in the **Chapter 5**. The effects of stated phenomena are analysed on the drug penetration efficacy of drug particles of different sizes.

- The multiscale method propounded in Chapter 5 is used to study the penetration of chemotherapeutic drugs in **Chapter 6**.

- Finally, the thesis is concluded in **Chapter 7** with a brief discussion on further developments in the model to deal with more complex problems in the future.

भारतीय प्रौद्योगिकी संस्थान गुवाहाटी
Indian Institute of Technology Guwahati

CHAPTER 2

FINITE VOLUME HETEROGENEOUS MULTISCALE METHOD

In this chapter, a novel finite volume heterogeneous multiscale method (FV-HMM) is propounded based on the HMM framework to study mass transport in biological tissues. There are two models at different scales that govern the mass transport. One is the macroscale model that governs the mass balance at the tissue scale. The second one is a microscale model that determines the mass transport at the cellular scale comprising extracellular matrix and cellular properties. In the microscale model, diffusion is the mode of drug transport in intra- and extra-cellular spaces, and the partition coefficient is also included across the cell membrane. In order to accurately incorporate the cell membrane, an immersed interface method (IIM) based on the alternating direction implicit (ADI) scheme is proposed. In the FV-HMM, an upscaling technique is defined to upscale the microscopic effects to the macroscale model. Numerical convergence and robustness of the FV-HMM and IIM are studied with model problems.

2.1 Model formulation

In order to model mass transport in tissues, a two-dimensional tissue domain, as shown in Fig. 2.1, is considered. The tissue domain is assumed to be a porous medium consisting of dispersed cells with extracellular matrix [24]. In a simplified form, the zoomed-version of tissue at a point **P** is shown in Fig. 2.1. The intra- and extra-cellular spaces are assumed to be filled with homogeneous and isotropic fluids. The cells are considered to be permeable and of

elliptical shape.

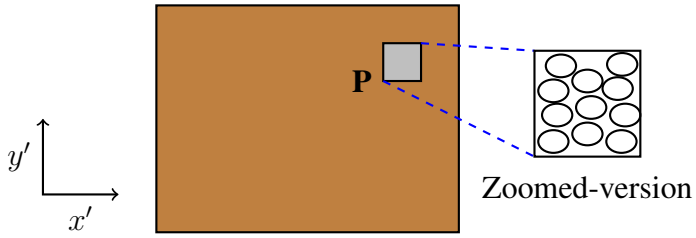

Figure 2.1: Schematic of a tissue domain and a simplified zoomed-version at a point **P** consists of dispersed cells.

For elevated tumor interstitial fluid pressure and in the absence of fluid flow, diffusion becomes the dominating mode of mass transport in biological tissues. In the present work, diffusion phenomenon and the partition coefficient of drug are considered. Let Ω' denotes the tissue domain, and its boundary is denoted by $\partial\Omega'$. The mass-balance relation used at macro scale (macroscale model) is given as,

$$\frac{\partial C'(t', \mathbf{x}')}{\partial t'} = \nabla' \cdot \mathbf{F}' \quad \text{in} \quad (0, \tau'] \times \Omega', \tag{2.1}$$

with initial condition

$$C'(0, \mathbf{x}') = C'_0(\mathbf{x}') \quad \text{in} \quad \Omega', \tag{2.2}$$

and some prescribed boundary condition on $\partial\Omega'$. In above equations, $C'(t', \mathbf{x}')$ denotes the drug concentration at time t' at a position $\mathbf{x}' = (x', y') \in \Omega'(\subset \mathbb{R}^2)$, where Ω' is a bounded domain. $\nabla' = (\frac{\partial}{\partial x'}, \frac{\partial}{\partial y'})$ denotes the gradient operator. Here, $\mathbf{F}' = (F'_{x'}, F'_{y'})$ is an unknown flux vector and it may be termed as macro flux. In continuum modelling, a fundamental constitutive relation known as the Fick's law is used for $\mathbf{F}'$; but here, $\mathbf{F}'$ is a more general unknown flux vector rather than the Fickian one. $\mathbf{F}'$ is determined by solving microscale model, which accounts for diffusion and partition coefficient of the drug. Note that the macroscale model is not complete as $\mathbf{F}'$ is unknown.

Dimensionless macroscale model

Let $\tilde{C}$ (maximum of the initial concentration) be the typical concentration scale in the tissue domain. Let $\tilde{L}$ (the length of the tissue domain along x'-direction) and $\tilde{D}$ (microscopic molecular diffusivity in extracellular space) are the typical length and diffusivity scales, respectively.

Then the typical time scale is obtained as, $\tilde{t} = \tilde{L}^2/\tilde{D}$. Thus, the dimensionless parameters can be written as,

$$t = \frac{t'}{\tilde{t}},\ x = \frac{x'}{\tilde{L}},\ y = \frac{y'}{\tilde{L}},\ C = \frac{C'}{\tilde{C}},\ \text{and}\ \mathbf{F} = \frac{\mathbf{F}'}{\tilde{C}\tilde{L}/\tilde{t}},$$

which lead to the dimensionless governing mass-balance equation as,

$$\frac{\partial C(t,\mathbf{x})}{\partial t} = \nabla \cdot \mathbf{F} \quad \text{in} \quad (0,\tau] \times \Omega, \tag{2.3}$$

with initial condition

$$C(0,\mathbf{x}) = C_0(\mathbf{x}) \quad \text{in} \quad \Omega. \tag{2.4}$$

Thus, $\mathbf{F} = (F_x, F_y)$ is an unknown dimensionless flux vector.

In order to find concentration distribution in Ω, knowledge of $\mathbf{F}$ is required in advance. In the next section, the FV-HMM method is developed to solve the macroscale model.

2.2 Finite volume heterogeneous multiscale method (FV-HMM)

The macroscale model (Eqs. (2.3)-(2.4)) is solved in the HMM framework that enables to incorporate the microscopic heterogeneity. In this section, a full-description of the methodology is presented.

2.2.1 Choice of macro solver

The macroscale model (Eq. (2.3)) governs the mass conservation law; so, the finite volume method is chosen for the discretization as it automatically conserves the flux in the entire computational domain [42]. For simplicity, let Ω be a square domain. The domain is discretized in $N \times N$ non-overlapping control volumes with uniform step size $h\ (= \frac{1}{N})$ in x- and y-directions and each control volume (CV) is denoted by (k,l), $k,l = 1,2,\ldots,N$. Let e_f, w_f, n_f, and s_f denote the east, west, north, and south faces of the CV, respectively. Also, assume that the state variable C is placed at the centre of the CV (k,l), denoted by $C_{k,l}$. Integrating Eq. (2.3) on the CV leads to

$$\begin{aligned}\int_{CV} \frac{\partial C(t,\mathbf{x})}{\partial t} dxdy &= \int_{e_f} F_x dy + \int_{n_f} F_y dx - \int_{w_f} F_x dy - \int_{s_f} F_y dx \\ &= F_{e_f} + F_{n_f} - F_{w_f} - F_{s_f},\end{aligned} \tag{2.5}$$

where F_{e_f}, F_{n_f}, F_{w_f}, and F_{s_f} are the approximate fluxes on e_f, n_f, w_f, and s_f faces, respectively, obtained by prevailing the flux of face centre to the face.

Now, the left-hand-side of Eq. (2.5) can be approximated as,

$$\int_{\text{CV}} \frac{\partial C(t,\mathbf{x})}{\partial t} dxdy \approx \frac{\partial}{\partial t}(C_{k,l}(t))h^2. \tag{2.6}$$

In words, the approximation is obtained by replacing $C(t,\mathbf{x})$ by $C_{k,l}(t)$, the average value in the CV (k,l), and it is taken to be at the centre of the CV.

By using (2.6) in Eq. (2.5) and then integrating in time from t_n to t_{n+1}, where $t_n = n\Delta t$ for Δt to be a time step and n a non-negative integer, a further simplified equation can be obtained as,

$$\frac{C_{k,l}(t_{n+1}) - C_{k,l}(t_n)}{\Delta t} \approx \frac{1}{h^2}\left[F_{e_f} + F_{n_f} - F_{w_f} - F_{s_f}\right]|_{t_n}, \tag{2.7}$$

where $|_{t_n}$ denotes the value at time t_n. Thus, the macroscopic set of difference equations (for $C_{k,l}^{n+1}$) can be written as,

$$C_{k,l}^{n+1} \approx C_{k,l}^{n} + \frac{\Delta t}{h^2}\left[F_{e_f}^{n} + F_{n_f}^{n} - F_{w_f}^{n} - F_{s_f}^{n}\right], \tag{2.8}$$

where $C_{k,l}^{n}$ is the concentration in the CV (k,l) for $k,l = 1,2,\ldots,N$, and superscript n denotes the value at time t_n.

To advance the macroscopic set of Eqs. (2.8) from time t_n to t_{n+1}, unknown fluxes F_p^n for $p = e_f, n_f, w_f, s_f$ need to be determined. To fulfil this requirement, a microscale model is constructed at each face of the CV in the next.

2.2.2 Set-up of microscale model

A schematic representation of the microscale domain centred at each face is shown in Fig. 2.2(a) (assume that the control volume face does not lie on the macroscale domain boundary; otherwise, the case is discussed in Section 2.2.5). The microscale domain should be sufficiently large to account the heterogeneity. In general, the size of a microscale domain is chosen to be larger than the periodicity of macroscale domain or the correlation length [68]. In this thesis, the microscale domain is chosen to be a square containing an elliptical cell (schematic diagram is shown in Fig. 2.2(b)).

Consider a microscale domain of side (λ) that contains a cell placed at the centre of it. Let ω denotes the typical microscale domain, and intra- and extra-cellular spaces are identified by ω_I

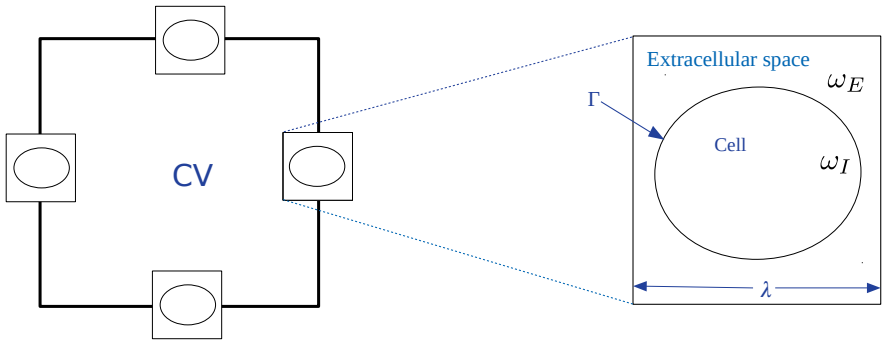

Figure 2.2: Schematic of (a) a control volume (CV) with microscale domain each of on its face centre and (b) a typical microscale domain.

and ω_E, respectively. The governing (dimensionless) mass-balance equation for the microscale model is considered as,

$$\frac{\partial c(t,\mathbf{x})}{\partial t} = \nabla \cdot (\mathbf{D}\nabla c) \quad \text{in} \quad \omega, \tag{2.9}$$

where $\mathbf{D}$ is diffusion tensor, and c is microscopic state variable (microscopic concentration). The diffusion tensor can be written as $\mathbf{D} = D\mathbf{I}$, where $\mathbf{I}$ is the identity matrix, and D is a scalar. The diffusion coefficient D is denoted by D_E and D_I in extra- and intra-cellular spaces, respectively. The presented methodology can also be applied to more general $\mathbf{D}$. Note that $D_E = D'_E/\tilde{D}$ and $D_I = D'_I/\tilde{D}$, where D'_E and D'_I are the dimensional variants of D_E and D_I, respectively. As $\tilde{D}$ is taken to be the extracellular diffusivity, $D_E = 1$. Due to the different structural complexity of cells and extracellular space, D_I and D_E can be significantly different; thus, D may be discontinuous across the cell membrane.

The dimensional form of the above equation can be obtained using the scales defined earlier for the macroscale model. The microscale model (Eq. (2.9)) is valid in intra- and extra-cellular spaces (Fig. 2.2(b)). Partition coefficient is incorporated across the cell membrane.

Partition coefficient

The partition coefficient (K) is defined, for unionized solute, at the interface of two immiscible solvents. As the cell membrane is made up of lipid-bilayer and hydrophobic in nature, the partition coefficient can be defined as,

$$K = \frac{c_I}{c_E}, \tag{2.10}$$

where c_I and c_E are the concentrations of a solute in intra- and extra-cellular spaces, respectively, in equilibrium [34].

Interface conditions

Partition coefficient is incorporated through the interface condition at the cell membrane (Γ, Fig. 2.2(b)). So, the interface conditions (with no source/sink) are considered as,

$$c_I = K c_E \quad \text{at} \quad \Gamma, \tag{2.11}$$

$$\left[D \frac{\partial c}{\partial \mathbf{n}} \right]_\Gamma = 0, \tag{2.12}$$

where $\mathbf{n}$ is an outward unit normal vector to the interface Γ, and c_I and c_E are the concentrations in intra- and extra-cellular spaces, respectively. Eq. (2.12) provides a jump in normal flux across Γ and is defined in (2.29).

Next, the initial and boundary conditions for the microscale model are evaluated using the macroscopic state variable (C).

Reconstruction for initial and boundary values (reconstruction operator)

To formulate the multiscale model in HMM framework, microscale models should be constrained with the macroscopic state variables. As the concentration gradient is the driving force for the concentration distribution, it is necessary to constrain the microscale model with the macroscopic concentration gradient. Also, partition plays a role in the concentration distribution across the cell membrane. In order to solve microscale model, these constraints should be used as a reconstruction operator, i.e., to construct appropriate initial and (artificial) boundary conditions. The initial and boundary values for micro state variables are reconstructed by interpolating macroscopic concentrations, which are obtained from the previous step or initial values. The reconstruction using linear interpolation of macroscale values can not be used directly as in literature [1, 61]. The reconstruction should be consistent with the condition in Eq. (2.11).

First, assume that the control volume's face does not lie on the macroscale domain boundary ($\partial\Omega$) so that the microscale model can be constructed at the face as shown in Fig. 2.2(a). For control volume (k, l), whose coordinate is (x_k, y_l), let the microscale domains situated at east, west, north, and south faces are denoted by ω^{e_f}, ω^{w_f}, ω^{n_f}, and ω^{s_f}, respectively, as shown in Fig. 2.2(a). The positions of the microscale domains ω^{e_f} and ω^{n_f} in Ω are determined as

follows. An illustration is also depicted in Fig. 2.3 for ω^{e_f}. Let $\epsilon^- = \dfrac{h-\lambda}{2}$ and $\epsilon^+ = \dfrac{h+\lambda}{2}$, then

$$\omega^{e_f} = \left[x_k + \epsilon^-, x_k + \epsilon^+\right] \times \left[y_l - \lambda/2, y_l + \lambda/2\right],$$
$$\omega^{n_f} = \left[x_k - \lambda/2, x_k + \lambda/2\right] \times \left[y_l + \epsilon^-, y_l + \epsilon^+\right].$$

The microscale domain ω is discretized by $M \times M$ Cartesian mesh with step sizes δx and δy in x- and y-directions, respectively, with $\delta x = \delta y$ $(= \frac{1}{M-1})$, and the grid points are denoted by (i, j), $i, j = 1, 2, \ldots, M$.

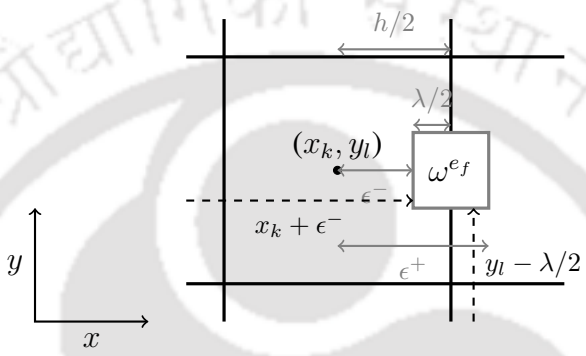

Figure 2.3: An illustration to determine the position of a microscale computational domain (ω^{e_f}) in Ω.

Let $c^n_{i,j}$ be the numerical microscopic concentration at grid point (i, j) in ω, at time t_n. The schematic for the reconstruction is shown in Fig. 2.4. Reconstruction for ω^{e_f} is defined as,

$$c^n_{i,j} = \begin{cases} C^n_{k,l} + \xi_i \frac{C^n_{k+1,l} - C^n_{k,l}}{h}, & \text{for } j = 1, 2, \ldots, M, \text{ and } (i,j) \text{ falls in } \omega_E, \\ K\left[C^n_{k,l} + \xi_i \frac{C^n_{k+1,l} - C^n_{k,l}}{h}\right], & \text{for } j = 1, 2, \ldots, M, \text{ and } (i,j) \text{ falls in } \omega_I, \end{cases} \tag{2.13}$$

and $\xi_i = \epsilon^- + (i-1)\delta x$ for $i = 1, 2, \ldots, M$. The reconstruction for ω^{n_f} is defined as,

$$c^n_{i,j} = \begin{cases} C^n_{k,l} + \eta_j \frac{C^n_{k,l+1} - C^n_{k,l}}{h}, & \text{for } i = 1, 2, \ldots, M, \text{ and } (i,j) \text{ falls in } \omega_E, \\ K\left[C^n_{k,l} + \eta_j \frac{C^n_{k,l+1} - C^n_{k,l}}{h}\right], & \text{for } i = 1, 2, \ldots, M, \text{ and } (i,j) \text{ falls in } \omega_I, \end{cases} \tag{2.14}$$

and $\eta_j = \epsilon^- + (j-1)\delta y$ for $j = 1, 2, \ldots, M$. The reconstructions for ω^{w_f} and ω^{s_f} are similar to that for ω^{e_f} and ω^{n_f}, respectively.

In case the CV is adjacent to the boundary, at least one of its face lies on $\partial\Omega$. Then, the microscale domain on that face can not taken as depicted in Fig. 2.2(a). So, the discussion for the microscale model on this type of face is deferred to the Section 2.2.5.

Dirichlet's boundary condition, obtained from reconstruction, is used in the simulation of microscale model.

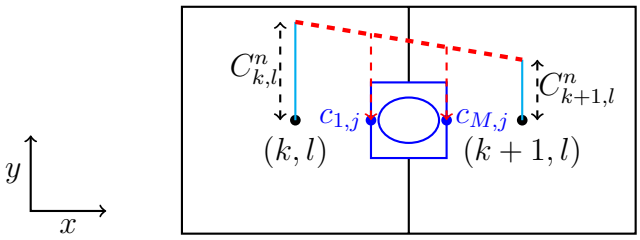

Figure 2.4: A procedure to obtain the boundary condition for the microscale model constructed at the east face of the CV (k,l).

2.2.3 Simulation of microscale model

Microscale model is evolved for time τ_{mic} (where $\tau_{mic} < \Delta t$) with time step δt, to achieve quasi-equilibrium state. This microscale evolution does not contribute to the macroscopic time step advancement. The microscale models are simulated using the method developed in Section 2.3.

The microscale model simulations are carried out to achieve the quasi-equilibrium state in macro flux. So, a tolerance value ε_{tol} is also set to stop the micro time evolution in the FV-HMM algorithm, i.e., to achieve quasi-equilibrium state

$$\frac{|F^{n,m+1} - F^{n,m}|}{|F^{n,m+1}|} < \varepsilon_{\text{tol}}, \tag{2.15}$$

where $F^{n,m}$ denotes the macro flux calculated (discussed in Section 2.2.4) after m steps microscale model evolution in time and n denotes the macroscopic time t_n. Eq. (2.15) is used only if $F^{n,m+1} \neq 0$; otherwise, the macro flux (F) is taken to be zero. $\varepsilon_{\text{tol}} = 0.1$ is chosen for this study. Next, the estimation of macro flux from microscale simulation results is discussed.

2.2.4 Estimation of macro flux (estimation operator)

The macro flux is calculated from the microscale model simulation results by averaging the microscale flux [1]. The macro flux in the x-direction is evaluated as,

$$F_x = \frac{1}{\lambda^2} \int_{\omega} D \frac{\partial c}{\partial x} dx dy. \tag{2.16}$$

Note that c is obtained from the microscale model simulation results. To estimate the above integral, a forward differencing is used for $\frac{\partial c}{\partial x}$. For description, a stencil in the x-direction is depicted in Fig. 2.5, where the index j (y-direction) is omitted for the sake of brevity. As the microscale model contains an interface, the stencil involves interface is shown for explanation.

The intersecting point of grid line with the interface is denoted by $i+\theta$ and termed as interfacial grid point. The concentration c could be discontinuous across the interface, so a different treatment is needed in the approximation of integral at the grid point, say i, as shown in Fig. 2.5. At the interfacial point, c is defined in limiting sense: $c^-_{i+\theta}$ and $c^+_{i+\theta}$, the left and right limiting concentrations, respectively. The formulae to calculate the limiting concentrations at the interfacial point are given in Section 2.3.2 (Eqs. (2.38) and (2.39)). The integrand of Eq. (2.16), at such a grid point i, is approximated as,

$$\left(D\frac{\partial c}{\partial x}\right)_i = D_{i+\theta/2}\frac{c^-_{i+\theta}-c_i}{x_{i+\theta}-x_i}, \tag{2.17}$$

$$\left(D\frac{\partial c}{\partial x}\right)_{i+\theta} = D_{i+(1+\theta)/2}\frac{c_{i+1}-c^+_{i+\theta}}{x_{i+1}-x_{i+\theta}}, \tag{2.18}$$

where $x_{i+\theta} = x_i + \theta\delta x$ for $0 < \theta < 1$. $D_{i+\theta/2}$ denotes the value at point $i+\theta/2$ which is a midpoint of i and $i+\theta$. The index $i+(1+\theta)/2$ denotes the value at the midpoint of $i+\theta$ and $i+1$. The value of diffusivity at the midpoint is used directly as it is known to us.

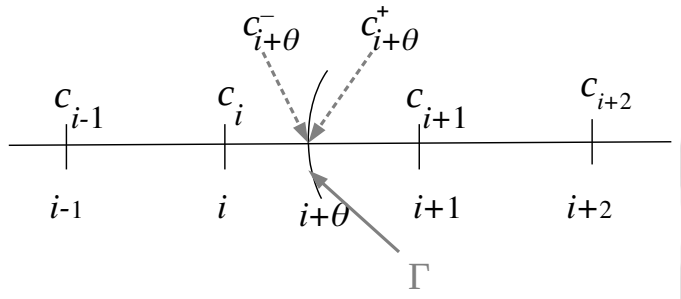

Figure 2.5: Schematic representation of interfacial point $(i+\theta, j)$, for fix j.

Let J denotes the set of all grid points that are located just left to the interfacial point, then

$$\int_\omega D\frac{\partial c}{\partial x}dxdy = \sum_{\substack{1\le i,j\le M-1,\\ (i,j)\notin J}} D_{i+1/2,j}\left(c_{i+1,j}-c_{i,j}\right)\delta y + \sum_{\substack{1\le i,j\le M-1,\\ (i,j)\in J}} \left(D_{i+\theta/2,j}\left(c^-_{i+\theta,j}-c_{i,j}\right) + D_{i+(1+\theta)/2,j}\left(c_{i+1,j}-c^+_{i+\theta,j}\right)\right)\delta y, \tag{2.19}$$

where index $i+1/2$ denotes the value at the midpoint of i and $i+1$.

Similarly, the macro flux in the y-direction is evaluated. For this, let J denote the set of all grid points that located below to the interface, then y-directional flux is calculated as,

$$F_y = \frac{1}{\lambda^2}\int_\omega D\frac{\partial c}{\partial y}dxdy, \tag{2.20}$$

where the integral is determined using the relation

$$\int_{\omega} D\frac{\partial c}{\partial y}dxdy = \sum_{\substack{1\le i,j\le M-1,\\ (i,j)\notin J}} D_{i,j+1/2}\left(c_{i,j+1}-c_{i,j}\right)\delta x + \sum_{\substack{1\le i,j\le M-1,\\ (i,j)\in J}} \left(D_{i,j+\theta/2}\left(c^{-}_{i,j+\theta}-c_{i,j}\right)+D_{i,j+(1+\theta)/2}\left(c_{i,j+1}-c^{+}_{i,j+\theta}\right)\right)\delta x. \quad (2.21)$$

2.2.5 Evaluation of boundary flux

In order to find concentration in the CV adjacent to the macroscale boundary, the flux at the boundary needs to be determined. Though the boundary condition (Neumann or Dirichlet) is prescribed, the effective diffusion coefficient is not known at the macro scale, the macro boundary flux can not be approximated using classical interpolation techniques. Microscale models are constructed at the boundary faces of the CV; the schematic for microscale domains is shown in Fig. 2.6(a) on a 3×3 finite volume mesh. The first thing is the reconstruction of initial and boundary conditions for microscale models. Let us discuss the case as shown in Fig. 2.6(b); others can be treated similarly. As there is no control volume on the right of this CV, one can not directly employ Eq. (2.13). In this case, we introduce a point on the boundary where the concentration is given to be C_b as pointed in Fig. 2.6(b), and then the reconstruction is used as ($k = N$),

$$c^n_{i,j} = \begin{cases} C^n_{N,l} + \xi_i \frac{C_b - C^n_{N,l}}{h/2}, & \text{for } j = 1,2,\ldots,M, \text{ and } (i,j) \text{ falls in } \omega_E, \\ K\left[C^n_{N,l} + \xi_i \frac{C_b - C^n_{N,l}}{h/2}\right], & \text{for } j = 1,2,\ldots,M, \text{ and } (i,j) \text{ falls in } \omega_I, \end{cases} \quad (2.22)$$

and $\xi_i = (h/2 - \lambda) + (i-1)\delta x$ for $i = 1,2,\ldots,M$.

The macro flux is estimated as discussed in Section 2.2.4.

2.2.6 Evolution of macroscopic equations

Once the macro flux is known at each face of each CV, the macroscopic set of governing equations (2.8) are solved to obtain concentration at time t_{n+1}. As the system of equations (2.8) is explicit, so small temporal step is required for stability.

2.2.7 Summary of the FV-HMM algorithm

In summary, the macroscale model is discretized using the finite volume method (Eqs. (2.8)), and the macro fluxes are estimated from the microscale information. In macroscale model, the

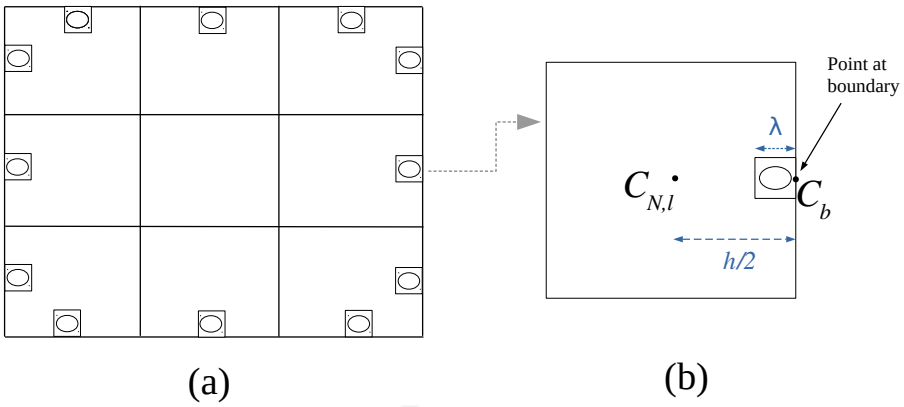

Figure 2.6: (a) Construction of microscale domains at the boundary faces of respective control volumes, and (b) an illustration of the reconstruction for the boundary microscale model.

concentration distribution is known at the initial time, $t = 0$. The algorithm to advance the macroscopic equations (2.8) from time t_n to t_{n+1} by using FV-HMM is displayed in Fig. 2.7 in the form of a flow chart.

2.3 Immersed interface method (IIM)

In this section, an alternating direction implicit (ADI) scheme based immersed interface method is developed for a fixed interface. The scheme is developed for the two-dimensional unsteady reaction-diffusion problem, which is a more general problem compared to the one defined in Section 2.2.2.

2.3.1 Model formulation

The physical domain, as shown in Fig. 2.8, is denoted by ω with boundary $\partial\omega$. An interface Γ, that divides ω into ω_E and ω_I, is considered to be immersed into the domain. The interface is given by

$$\Gamma : \frac{(x-x_0)^2}{{a_1}^2} + \frac{(y-y_0)^2}{{a_2}^2} = 1, \tag{2.23}$$

where (x_0, y_0) is the centre of the ellipse, and a_1 and a_2 are constants such that $2a_1$ is the horizontal axis length and $2a_2$ is the vertical axis length of the ellipse.

The following two-dimensional parabolic interface problem is considered with fixed Γ:

$$\frac{\partial c(t,x,y)}{\partial t} = \nabla \cdot (a(x,y)\nabla c) + f(t,x,y), \quad (t,x,y) \in (0, \tau_{mic}] \times \omega, \tag{2.24}$$

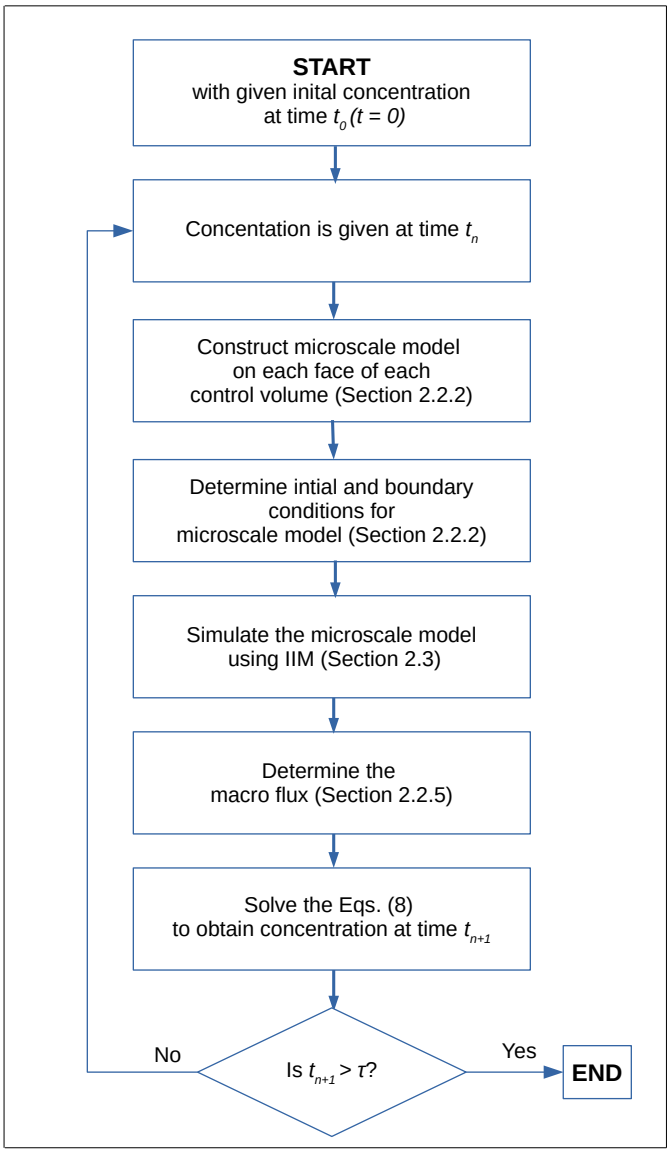

Figure 2.7: A pictorial summary of the FV-HMM algorithm.

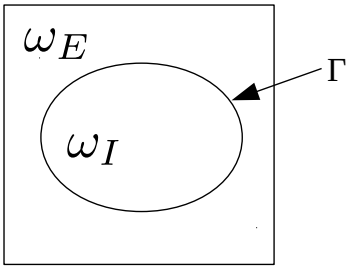

Figure 2.8: A two-dimensional physical domain with an immersed interface Γ that divides domain (ω) into two parts: ω_E and ω_I.

with initial and boundary conditions

$$c(0, x, y) = c_0(x, y), \quad (x, y) \in \omega, \tag{2.25}$$

$$c(t, x, y) = c_b, \quad (x, y) \in \partial\omega, \tag{2.26}$$

where $f(t,x,y)$ and $a(x,y)$ are piecewise continuous real-valued functions but may have finite jump discontinuity across the interface Γ. τ_{mic} is the stipulated time frame for the model. The interface conditions are given by

$$c^-(t,x,y) = Kc^+(t,x,y), \quad (x,y) \in \Gamma, \tag{2.27}$$

$$\left[a\frac{\partial c}{\partial \mathbf{n}}\right]_\Gamma = 0, \tag{2.28}$$

where K is a constant. Eq. (2.28) provides jump condition in normal flux at the interface Γ, and this condition is defined as,

$$\left[a\frac{\partial c}{\partial \mathbf{n}}\right]_\Gamma = a^+\frac{\partial c^+}{\partial \mathbf{n}} - a^-\frac{\partial c^-}{\partial \mathbf{n}}, \tag{2.29}$$

where $'+'$ and $'-'$ signs are denoting the limiting values from ω_E and ω_I, respectively, at the interface.

2.3.2 Numerical method

For simplicity, consider ω to be a unit square domain, and it is discretized by Cartesian mesh with uniform step size δx $(= \frac{1}{M-1})$ in x- and y-directions. The coordinates (x_i, y_j) for the Cartesian grid points (i,j) are given by

$$x_i = (i-1)\delta x,\ y_j = (j-1)\delta x \quad \text{for } i,j = 1,2,\ldots,M. \tag{2.30}$$

The Cartesian grid points are classified as regular and irregular (depicted in Fig. 2.9). A grid point is said to be irregular if the standard finite difference approximation involves the stencil from both sides of the interface. Irregular grid points are further classed into x-irregular and y-irregular. A Cartesian grid point, which involves points from both sides of the interface in the finite difference stencil that resulted from the approximation of derivatives along x-direction, is said to be x-irregular. A Cartesian grid point, which involves points from both sides of the interface in the finite difference stencil that resulted from the approximation of derivatives along y-direction, is said to be y-irregular. A grid point can be both x-irregular and y-irregular simultaneously, and a grid point is said to be regular if it is not irregular.

ADI scheme [58] used at the regular grid points is given as,

$$\frac{c_{i,j}^{m+1/2} - c_{i,j}^m}{\delta t/2} = \left(\delta_x\left(a\delta_x c\right)\right)_{i,j}^{m+1/2} + \left(\delta_y\left(a\delta_y c\right)\right)_{i,j}^m + f_{i,j}^{m+1/2}, \tag{2.31}$$

$$\frac{c_{i,j}^{m+1} - c_{i,j}^{m+1/2}}{\delta t/2} = \left(\delta_x\left(a\delta_x c\right)\right)_{i,j}^{m+1/2} + \left(\delta_y\left(a\delta_y c\right)\right)_{i,j}^{m+1} + f_{i,j}^{m+1/2}, \tag{2.32}$$

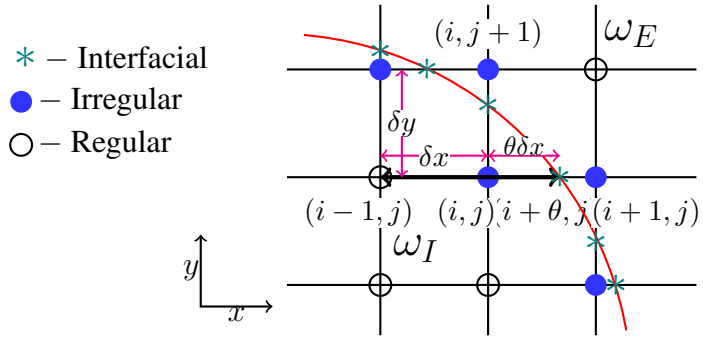

Figure 2.9: An illustration of the regular, irregular, and interfacial grid points.

where

$$(\delta_x\,(a\delta_x c))^m_{i,j} = \left\{ \frac{a_{i+1/2,j}c^m_{i+1,j} - (a_{i+1/2,j} + a_{i-1/2,j})c^m_{i,j} + a_{i-1/2,j}c^m_{i-1,j}}{(\delta x)^2} \right\}$$

and

$$(\delta_y\,(a\delta_y c))^m_{i,j} = \left\{ \frac{a_{i,j+1/2}c^m_{i,j+1} - (a_{i,j+1/2} + a_{i,j-1/2})c^m_{i,j} + a_{i,j-1/2}c^m_{i,j-1}}{(\delta x)^2} \right\}.$$

Here, δt is the time step. δ_x is a central-difference operator in x-direction, which is defined as,

$$\delta_x(g_i) = \frac{g_{i+1/2} - g_{i-1/2}}{\delta x}$$

for some function g. Similarly, δ_y is defined in the y-direction. $c^m_{i,j}$ denotes the concentration at grid point (i, j) on time $t_m (= m\delta t)$. $c^{m+1/2}_{i,j}$ is the concentration at time $t_{m+1/2} = (m + 1/2)\delta t$. The index $(i + 1/2)$ denotes the value at midpoint of i and $(i + 1)$ grid points. Accordingly, the indices $i - 1/2$, $j - 1/2$, and $j + 1/2$ are also defined.

As the coefficient (a) can be discontinuous across the interface, the ADI scheme can not be used directly for irregular grid points. For the treatment of irregular grid points, the interfacial points are introduced at the interface, which are defined as the intersecting points at the interface with the Cartesian grid lines (Fig. 2.9).

A zero level set function used to identify the interface is given as,

$$\Phi(x, y) = \frac{(x - x_0)^2}{a_1^2} + \frac{(y - y_0)^2}{a_2^2} - 1, \quad (x, y) \in \omega. \tag{2.33}$$

Thus, $\Phi > 0$ in ω_E, $\Phi < 0$ in ω_I, and $\Phi = 0$ corresponds to Γ.

Here, we will discuss the modified formula for x-irregular grid point and similarly can be derived for y-irregular grid point. In order to define the modified formula, the idea is adopted from the article [38]. As the discussion is for x-direction, the indices m and j are dropped for

the sake of brevity. The modified difference operator for the x-irregular grid point is defined as,

$$(\delta_x (a\delta_x c))_i = \left\{ a_{i+\theta/2} \frac{c^-_{i+\theta} - c_i}{x_{i+\theta} - x_i} - a_{i-1/2} \frac{c_i - c_{i-1}}{x_i - x_{i-1}} \right\} \Bigg/ \left(\frac{x_{i+\theta} - x_{i-1}}{2} \right), \tag{2.34}$$

where $x_{i+\theta} = x_i + \theta\delta x$ for some $0 < \theta < 1$, and $c^-_{i+\theta}$ is the left limiting concentration at the interfacial grid point $i + \theta$.

If the Cartesian grid point falls in between two interfacial grid points, as the case shown in Fig. 2.10, the modified difference operator is used as,

$$(\delta_x (a\delta_x c))_i = \left\{ a_{i+\theta_1/2} \frac{c^-_{i+\theta_1} - c_i}{x_{i+\theta_1} - x_i} - a_{i-\theta_2/2} \frac{c_i - c^+_{i-\theta_2}}{x_i - x_{i-\theta_2}} \right\} \Bigg/ \left(\frac{x_{i+\theta_1} - x_{i-\theta_2}}{2} \right), \tag{2.35}$$

where $x_{i+\theta_1} = x_i + \theta_1\delta x$ and $x_{i-\theta_2} = x_i - \theta_2\delta x$ for some $0 < \theta_1, \theta_2 < 1$.

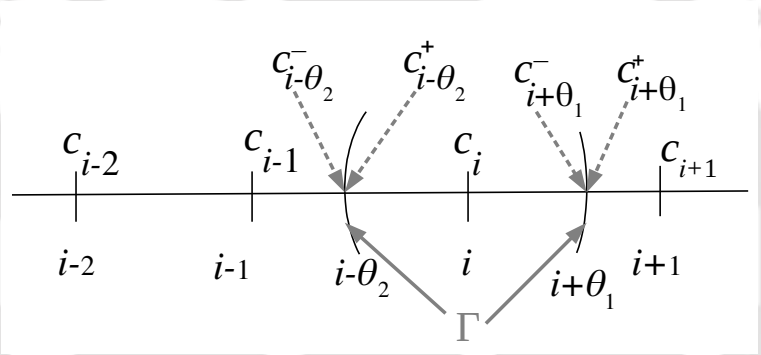

Figure 2.10: Schematic of Cartesian grid point i which falls in between two interfacial points $i + \theta_1$ and $i - \theta_2$, for fixed j and m.

Eqs. (2.34) and (2.35) require left and right interfacial limiting values of the variable at the interfacial grid point. The interfacial unknowns are determined using Lagrange's interpolating polynomials [38]. In this work, linear interpolation is used to find the interfacial values. For description, consider the case as shown in Fig. 2.5. In this case, $c^-_{i+\theta}$ and $c^+_{i+\theta}$ need to be determined. The interpolating polynomial using the values c_i and $c^-_{i+\theta}$ can be written as,

$$L^-(x) = \frac{x - x_{i+\theta}}{x_i - x_{i+\theta}} c_i + \frac{x - x_i}{x_{i+\theta} - x_i} c^-_{i+\theta}. \tag{2.36}$$

Note that, to determine interpolating polynomial using $c^-_{i+\theta}$ at point $i + \theta$ only left side grid points should be used namely $c^-_{i+\theta}$, c_i, c_{i-1}, and so on. Similarly, other side interpolating polynomial using the points c_{i+1} and $c^+_{i+\theta}$ can be written as

$$L^+(x) = \frac{x - x_{i+\theta}}{x_{i+1} - x_{i+\theta}} c_{i+1} + \frac{x - x_{i+1}}{x_{i+\theta} - x_{i+1}} c^+_{i+\theta}. \tag{2.37}$$

Now using Eqs. (2.27), (2.28), (2.36), and (2.37), and assuming that the grid point (shown in Fig. 2.5) lies in ω_E,

$$c^-_{i+\theta} = \frac{-a^+_{i+\theta}c_{i+1}(x_i - x_{i+\theta}) + a^-_{i+\theta}c_i(x_{i+1} - x_{i+\theta})}{Ka^+_{i+\theta}(x_{i+\theta} - x_i) - a^-_{i+\theta}(x_{i+\theta} - x_{i+1})}, \tag{2.38}$$

and

$$c^+_{i+\theta} = Kc^-_{i+\theta}, \tag{2.39}$$

where $'+'$ and $'-'$ in the superscript denote the limiting values from the right and left, respectively, at the interfacial point. If the Cartesian grid point falls at the interface, the grid point is treated as an interfacial point, the value of the unknown can be calculated using the arithmetic mean of interfacial limiting values [38]. A similar procedure is used to derive the above expressions for other x-irregular grid points and also for y-irregular grid points.

Here, we have used linear interpolating polynomials, as the microscale model in the FV-HMM algorithm requires simulation to achieve a quasi-equilibrium state. For this purpose, a few temporal iterations in the microscale model are sufficient. The presented methodology can also be used with higher order interpolating polynomials that can increase the order of accuracy of the method, for details see Ref. [38].

2.4 Numerical validation

Let $\mathcal{C}_{i,j}$ be the numerical approximation to $\hat{\mathcal{C}}(x_i, y_j)$ which is exact solution, at Cartesian grid point (i, j). The maximum error is defined as,

$$||E_{h'}||_\infty = \max_{1\le i,j\le n_b} \left|\mathcal{C}_{i,j} - \hat{\mathcal{C}}(x_i, y_j)\right|, \tag{2.40}$$

where n_b denotes the mesh size and the corresponding spatial step size is denoted by h'.

2.4.1 IIM

Numerical experiments are presented to examine the accuracy and convergence of IIM. A problem with discontinuous coefficient is discussed, and another problem with discontinuous coefficient and for $K \neq 1$ is solved.

The order of convergence is computed as follows:

$$\text{Order} = \frac{\log(||E_{\delta x_1}||_\infty / ||E_{\delta x_2}||_\infty)}{\log(\delta x_1/\delta x_2)}, \tag{2.41}$$

where δx_1 and δx_2 are two different spatial step sizes.

Problem 1. Consider Eqs. (2.24)–(2.28) on solution domain $\omega = [0,1] \times [0,1]$ and time interval $[0,1]$ with $a = 1$ and 2 in ω_E and ω_I (Fig. 2.8), respectively, and $K = 1$ is considered. The interface Γ is defined by $(x-0.5)^2 + (y-0.5)^2 = R^2$ with $R = 0.31$. Let $Z^2 = (x-0.5)^2 + (y-0.5)^2$. The source term is defined as,

$$f(t,x,y) = \begin{cases} \exp(-t)(f_1(x,y)((R^2 - Z^2)(-1+2\pi^2)+4) + 4\pi f_2(x,y)), & (x,y) \in \omega_E, \\ 0.5\exp(-t)(f_1(x,y)((R^2 - Z^2)(-1+4\pi^2)+8) + 8\pi f_2(x,y)), & (x,y) \in \omega_I, \end{cases} \tag{2.42}$$

where $f_1(x,y) = \sin(\pi x)\sin(\pi y)$ and $f_2(x,y) = (y-0.5)\sin(\pi x)\cos(\pi y) + (x-0.5)\sin(\pi y)\cos(\pi x)$. The initial and boundary conditions are specified as,

$$c(0,x,y) = \begin{cases} (R^2 - Z^2)\sin(\pi x)\sin(\pi y), & (x,y) \in \omega_E, \\ 0.5(R^2 - Z^2)\sin(\pi x)\sin(\pi y), & (x,y) \in \omega_I, \end{cases} \tag{2.43}$$

and

$$c(t,x,y) = 0, \quad (x,y) \in \partial\omega. \tag{2.44}$$

Then, the exact solution can be obtained as,

$$c(t,x,y) = \begin{cases} \exp(-t)(R^2 - Z^2)\sin(\pi x)\sin(\pi y), & (x,y) \in \omega_E, \\ 0.5\exp(-t)(R^2 - Z^2)\sin(\pi x)\sin(\pi y), & (x,y) \in \omega_I. \end{cases} \tag{2.45}$$

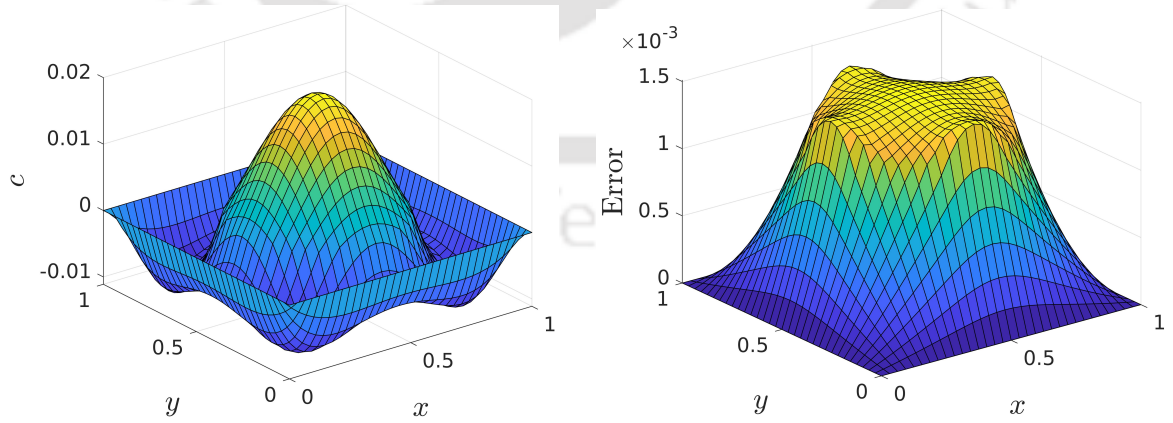

Figure 2.11: Surface plots of (a) numerical solution and (b) the error for Problem 1 at time $t = 1$.

In the Problem 1, the coefficient (a) is discontinuous, but both the solution and normal flux are continuous across the interface. This problem aims to test the method for discontinuous

coefficient. Table 2.1 shows maximum errors associated with different mesh sizes and the orders of convergence. The error decreases on mesh refinement. Fig. 2.11 displays the surface plots of numerical solution and error for $\delta t = \delta x = 1/2^5$ at $t = 1$.

Problem 2. Consider Eqs. (2.24)-(2.28) on solution domain $\omega = [0,1]\times[0,1]$ and time interval $[0,1]$ with $a = 1$ and 10 in ω_E and ω_I (Fig. 2.8), respectively, and $K = 0.1$ is considered. The interface Γ is defined by $(x-0.5)^2 + (y-0.5)^2 = 0.31^2$. The source term is defined by

$$f(t,x,y) = \begin{cases} \exp(-t)(-1+2\pi^2)\sin(\pi x)\sin(\pi y), & (x,y) \in \omega_E, \\ K\exp(-t)(-1+20\pi^2)\sin(\pi x)\sin(\pi y), & (x,y) \in \omega_I. \end{cases} \tag{2.46}$$

The initial and boundary conditions are specified as,

$$c(0,x,y) = \begin{cases} \sin(\pi x)\sin(\pi y), & (x,y) \in \omega_E, \\ K\sin(\pi x)\sin(\pi y), & (x,y) \in \omega_I. \end{cases} \tag{2.47}$$

and

$$c(t,x,y) = 0, \quad (x,y) \in \partial\omega. \tag{2.48}$$

Then, the exact solution is obtained as,

$$c(t,x,y) = \begin{cases} \exp(-t)\sin(\pi x)\sin(\pi y), & (x,y) \in \omega_1, \\ K\exp(-t)\sin(\pi x)\sin(\pi y), & (x,y) \in \omega_2. \end{cases} \tag{2.49}$$

In Problem 2, coefficient a is discontinuous across the interface but the jump in normal flux is zero, and the solution satisfies condition (2.27). The numerical errors and orders of convergence are shown in Table 2.1. The error reduces with mesh refinement. Fig. 2.12 displays the surface plots of numerical solution and error for $\delta t = \delta x = 1/2^5$ at $t = 1$.

2.4.2 FV-HMM

The following problem is presented for the validation of overall FV-HMM algorithm.

Problem 3. Consider the macroscale model (Eqs. (2.3) and (2.4)) on solution domain $\Omega = [0,1]\times[0,1]$ with the associated microscale model (Eq. (2.9)) having $D_E = D_I = 1$ and $K = 1$.

The initial condition for the macroscale model is specified as,

$$C(0,x,y) = \sin(\pi x)\sin(\pi y), \quad (x,y) \in \Omega, \tag{2.50}$$

Table 2.1: Error analysis for the IIM ($\delta x = \delta t = 1/2^s$).

s	Problem 1		Problem 2	
	$\|\|E_{\delta x}\|\|_\infty$	Order	$\|\|E_{\delta x}\|\|_\infty$	Order
3	8.502×10^{-3}	–	4.011×10^{-2}	–
4	3.728×10^{-3}	1.189	2.099×10^{-2}	0.933
5	1.509×10^{-3}	1.304	8.344×10^{-3}	1.331
6	6.862×10^{-4}	1.137	3.862×10^{-3}	1.111

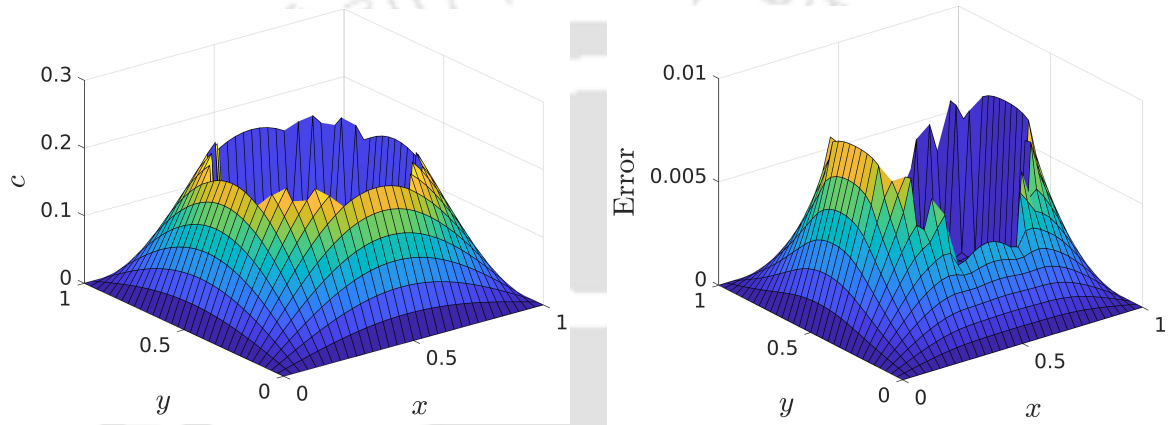

Figure 2.12: Surface plots of (a) numerical solution and (b) the error for Problem 2 at time $t = 1$.

and the boundary condition as,

$$C(t, x, y) = 0, \quad (x, y) \in \partial\Omega. \tag{2.51}$$

Then, the exact solution can be obtained as,

$$C(t, x, y) = \exp(-2\pi^2 t)\sin(\pi x)\sin(\pi y), \quad (x, y) \in \Omega. \tag{2.52}$$

Problem 3 is chosen to test the convergence of the FV-HMM on mesh refinement. λ is chosen to be 1.0×10^{-3}, and a circle placed at the centre of ω is taken of radius 4.1×10^{-4}. ω is discretized with 30×30 mesh, and the macroscale model is simulated for $t = 1$ with microscopic temporal step $\delta t = 1 \times 10^{-5}$. Results on macroscopic spatial grid refinement are shown in Table 2.2, where Δt is taken to be 1.0×10^{-4}. The coarse mesh refinement decreases the maximum error. The surface plots of exact and numerical solutions (on 20×20 macro grid) are displayed in Fig. 2.13.

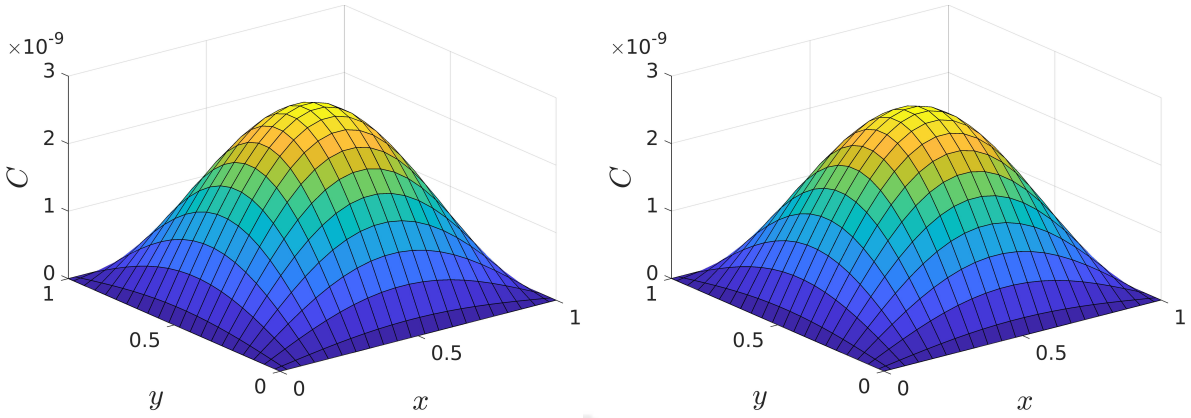

(a) (b)

Figure 2.13: Surface plots of (a) exact and (b) the FV-HMM solutions at time $t = 1$.

Table 2.2: Maximum error estimates for the FV-HMM (Problem 3).

Mesh size (macro spatial grid)	$\|\|E_h\|\|_\infty$
10×10	3.993×10^{-10}
20×20	5.666×10^{-11}
30×30	3.831×10^{-12}

2.5 Conclusions

Single scale continuum models are not sufficiently accurate for biological systems as they involve multiple scales. This motivated to look for a suitable mathematical model in the HMM framework. In this chapter, a novel finite volume heterogeneous multiscale method (FV-HMM) is propounded in the HMM framework. In the model, diffusion and partition phenomena are included as the main transport processes. The algorithm includes two models at different scales; macroscale model at tissue scale and microscale model at the cellular scale. The model includes cell heterogeneity to the tissue scale using macro-micro coupling. An immersed interface method (IIM) based on the ADI scheme is proposed to solve microscale models. Model problems are solved to test the convergence of the IIM and the overall algorithm, the FV-HMM. The IIM is found to be first-order accurate asymptotically.

CHAPTER 3

EFFECTS OF PARTICLE SIZE AND PARTITION COEFFICIENT ON DRUG DELIVERY

In the advancement of nanotechnology, it is now possible to formulate nanoparticle-based drug carriers such as lipid vesicles, gold nanoparticles, carbon-based nanoparticles, and DNA. These nano-constructs are being made for drug delivery into specific tissues or cells by overcoming the biological barriers. The design of these nanoparticles includes the following key parameters: surface, stiffness, shape, and size. *In vivo* and *in vitro* experiments have revealed that the particle size plays an important role in drug delivery [66, 56, 24, 20]. Wong et al. [66] performed in vitro experiments in collagen gel with 10 and 100 nanometer (nm) particles to investigate their penetration. Diffusion phenomenon was considered to be the main mode of transport. Tang et al. [56] performed *in vivo* experiments with 50 and 200 nm particles. Also, a spatio-temporal multiscale model was developed by Islam et al. [24] that accounts for diffusion and advection along with particle capturing efficacy. They used Brownian dynamics to track the individual particle movement in the domain consisting of spherical cells treated each one as a solid body. The effects of size of nanoparticle on tissue penetration and distribution efficacy were reported in the above mentioned articles [66, 56, 24]. The smaller size particles were found to penetrate in the deep as compared to the larger ones. Further developments in the modelling are required for a better insight at the tissue scale. The biological tissues are heterogeneously complex as the biophysical and biochemical processes occur at disparate temporal and spatial scales [12, 55].

The effects of microscopic structural and biophysical and biochemical processes on the

penetration efficacy of drug particles have not yet studied at the tissue scale (model). The cell membrane is made up of lipid bilayer whose middle part is hydrophobic to the water phase, hence, inhibits the movement of water-soluble molecules across the membrane. It leads to the partition phenomenon, which is incorporated in the mathematical model as a parameter known as partition coefficient. The partition coefficient determines how a solute distributes in two immiscible solvents [34]. It plays a significant role in the movement of biomolecules, nutrients, and other constituents across the cell membrane. Though, the influence of partition coefficient on drug penetration efficacy is not well understood. Also, as the cell geometry determines the tissue's microscopic structure and varies across the different tissues, it is vital to understand its impact on drug penetration. As already discussed, particle size is an important parameter that affects drug penetration, but the effects at tissue scale by combining tissues' complexity are not yet understood.

In this chapter, the FV-HMM is employed to study tissue penetration and distribution efficacy of drug delivery nanoparticles. Several numerical experiments are performed to understand the effects of different parameters such as biological fluid viscosity, nanoparticle size, partition coefficient, and the shape of cell on penetration efficacy of drug nanoparticles at the tissue scale.

3.1 Model problem

It is considered that the drug is made of nanometer size particles. So, the 'drug particles' and 'drug nanoparticles' both retain the same meaning and are used interchangeably in this thesis. The drug particles are considered to be spherical. So, the diffusion coefficients for the intra- and extra-cellular spaces are calculated using the Einstein-Stokes equation as follows,

$$D' = \frac{k_B T}{6\pi\mu r}, \tag{3.1}$$

where k_B denotes the Boltzmann's constant, T (310 Kelvin) is temperature, r the radius of nanoparticle, and μ denotes the viscosity of biological fluid. The viscosity parameter μ is denoted by μ_I and μ_E for the intra- and extra-cellular spaces, respectively.

For the study of drug penetration, the geometrical setup for tissue domain is shown in Fig. 3.1. The initial and boundary conditions are also displayed in Fig. 3.1. Continuous infusion of concentration is assumed at the left boundary of Ω', i.e., a reservoir is assumed to be fixed therein, which maintains concentration $C' = 1$ M (M – Molar). The upper and lower

boundaries are assumed to be impermeable $\left(\frac{\partial C'}{\partial y'} = 0 \text{ M cm}^{-1}\right)$; hence, the normal flux is set to be zero there, in tissue domain (macroscale model). The horizontal length of the domain is taken to be large enough so that the drug does not reach the right boundary in the stipulated time; thus, the right boundary can be set at zero concentration. The domain is assumed to be at zero concentration initially.

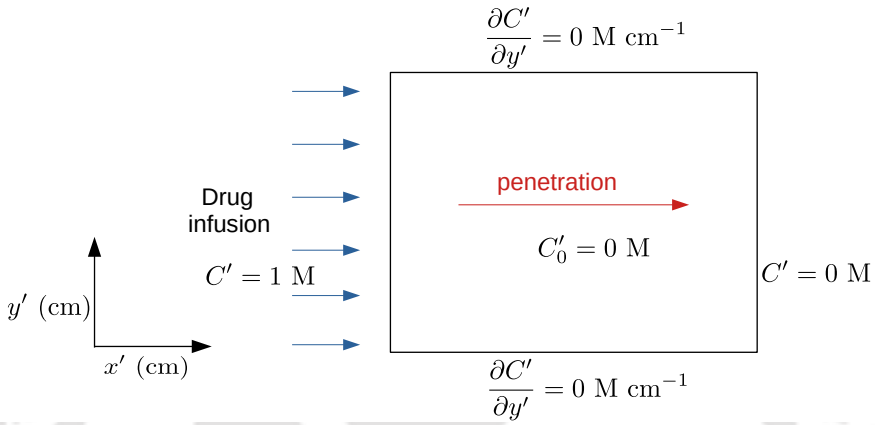

Figure 3.1: The geometrical setup for the problem. The arrow inside the tissue domain shows the direction of interest for drug penetration.

Other than the drug particle size, fluid viscosity is an important parameter for the calculation of diffusion coefficient (Eq. (3.1)). To enforce a realistic physiological situation in the model, literature is consulted for realistic values of the viscosity parameters. It is found that the cytosolic fluid (the fluid excluding macromolecules in the cell) is 1.2–1.4 times viscous than the water, where $\mu \approx 1$ cP (cP – centipoise) for water [15]. However, the intracellular fluid viscosity is greatly affected by the presence of macromolecules inside it. The present work has used the intracellular viscosity (μ_I) ranging in 1–10 cP; whereas, the extracellular fluid viscosity (μ_E) is taken to be 1 cP as the default value [63].

The size of Ω' (macroscale domain) is chosen to be 1×1 cm^2 by ensuring that the drug does not reach the right boundary in the stipulated time ($t' = 5$ h). The chosen parameters values and the initial and boundary conditions lead to zero flux along y'-direction, i.e., $F'_{y'} = 0$ M cm h^{-1} (h – hour) on north and south faces of each control volume. This conclusion is made by simulating the macroscale model. Thus, the concentration gradient will be occurred along x'-direction only in the macroscale model. Hence, it is enough to discretize the macroscale domain along x'-direction. On performing grid independency, it is found that the mesh size 70×1, i.e., 70 control volumes in x'-direction and 1 control volume in y'-direction, is sufficient

to discretize the macroscale domain. In each simulation, if not stated explicitly, the macroscale model is simulated for $t' = 5$ h with the macroscale time step $\Delta t = 1.0 \times 10^{-4}$ h. The size of cell is of order 10^{-4} cm and varies across the tissues [55]. In the present study, a circular cell (default shape) of diameter 8.2×10^{-4} cm is chosen to be placed at the centre of microscale domain (ω). ω is chosen to be a square of edge length 10^{-3} cm, and it is discretized by 100×100 spatial grid. The microscale time step is chosen to be $\delta t = 1.0 \times 10^{-5}$ h.

3.2 Results and discussion

3.2.1 Validation with the experimental results

The FV-HMM simulation results are used to capture the experimental work of Wong et al. [66]. In their work, nanoparticle penetration was studied in collagen gel. A direct quantitative comparison between the model and experimental data is not feasible due to the missing information on fluid properties (collagen gel viscosity). Here, an attempt is made for qualitative comparison of nanoparticle penetration. Simulation is carried out on 0.1×0.1 cm^2 macroscale domain as the experimental data is available in the range $\approx$ 0–0.08 cm (x'-axis distance that can be seen in Fig. 3.2). The FV-HMM is simulated for $t' = 12$ h with $D' = 6 \times 10^{-6}$ cm^2 h^{-1} to match with the experimental data. The results are displayed in Fig. 3.2. As the FV-HMM problem is effectively one-dimensional, the results are also compared with the following analytical solution [66],

$$C'(x', t') = \frac{2}{\sqrt{\pi}} \int_{x'/(2\sqrt{D't'})}^{\infty} \exp(s^2) ds. \tag{3.2}$$

It can be seen that the FV-HMM results agree well with the experimental data and analytical solution (see Fig. 3.2). The open-source application WebPlotDigitizer [45] is used to extract the Wong's experimental data, and the integral in (3.2) is evaluated using the function 'erfc' available in the MATLAB [37].

3.2.2 Effects of partition coefficient and drug particle size

The partition coefficient is used in pharmaceutical industries for drug formulations. Its impact on tissue penetration and distribution efficacy of drug nanoparticles is not well-understood. The FV-HMM is employed to analyze the partitioning effects on nanoparticle transport. In the

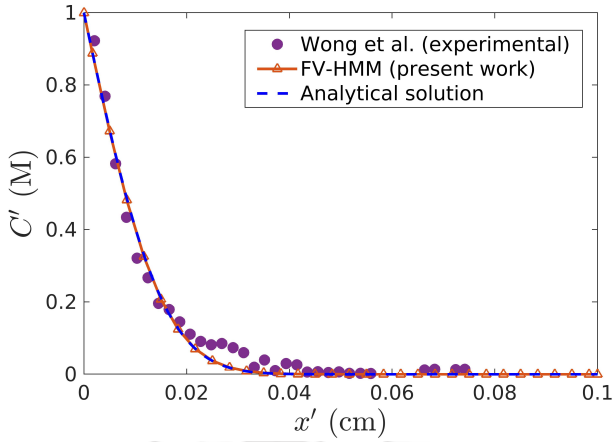

Figure 3.2: Comparison of the FV-HMM results with the experimental results and one-dimensional analytical solution. Solid line with marker represents the FV-HMM simulation result, whereas the filled circles and the dashed line represent experimental data from Wong et al. [66], and analytical solution, respectively.

following, the model discretization and the parameters are chosen to be the same as mentioned in Section 3.1. The macroscale domain is taken to be 1×1 cm^2. In this study, the range of K is considered to be $0 \leq K \leq 1$. Numerical experiments are performed with seven different values of K for 1 and 10 nm particles. Experiments are performed with constant diffusion coefficient in tissue and also for different diffusion (constant) values in intra- and extra-cellular spaces. Latter is more realistic as the diffusivity in intra- and extracellular spaces is significantly different in a real scenario.

Fig. 3.3(a) displays the results for constant viscosity $\mu = 2.5$ cP. Partitioning effects on penetration are significant in this case as the penetration depths are significantly different for $K = 0.1$ and $K = 1$. Fig. 3.3(b) displays the concentrations for 1 and 10 nm particles with different viscosity parameter values in intra- and extra-cellular spaces as, $\mu_I = 5$ cP and $\mu_E = 1$ cP. For 10 nm particles, partitioning effect on penetration is less significant than that of Fig. 3.3(a). Thus, the results on penetration with constant viscosity can be different from reality. However, the effects of partitioning are significant for 1 nm size particles even with different viscosities in intra- and extra-cellular spaces (Fig. 3.3(b)). Thus, it may be concluded that the tissue penetration efficacy of drug nanoparticles can be affected by the partition coefficient significantly.

From Fig. 3.3, one can also notice that the penetration depth is sensitive to K in the range $0.1 < K < 1$; however, insensitive when $K < 0.1$ for small as well as for large size nanopar-

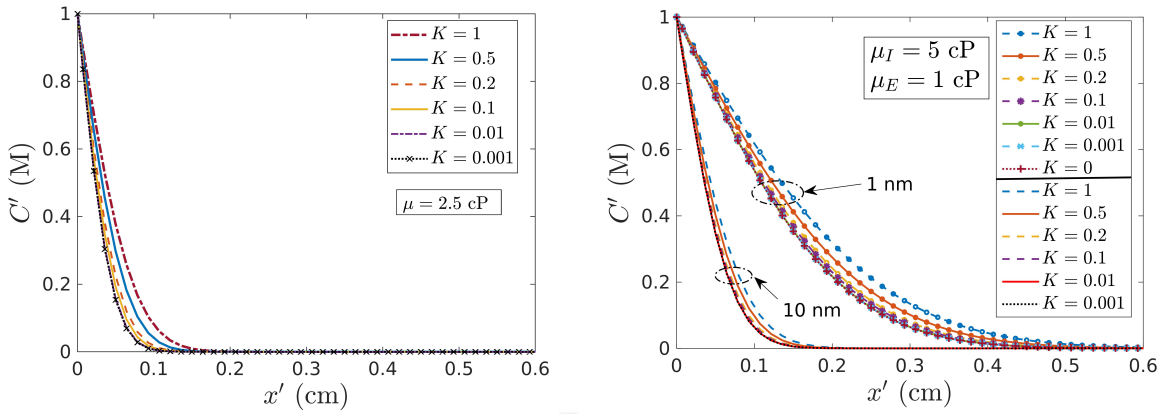

(a) (b)

Figure 3.3: Effects of partition coefficient on drug penetration. (a) For fixed constant diffusion in tissue for 10 nm particles and (b) for different diffusion coefficients in intra- and extracellular spaces for 1 and 10 nm particles.

ticles. Thus, in the following, $K = 0.1$ is chosen as a default value for the partitioning and $K = 1$ for no partition.

In Fig. 3.3(b), the effects of particle size on drug penetration can also be investigated. It can be seen that the smaller size particles (1 nm) penetrate in the deep as compared to the larger ones (10 nm). Moreover, the nanoparticles penetration for three different size particles (1, 10, and 100 nm) are displayed in Fig. 3.4. In Fig. 3.4(a), results are shown for $K = 0.1$, and in Fig. 3.4(b), results are displayed for $K = 1$. It can be seen that the smaller size particles penetrate in the deep as compared to the larger ones for each choice of K. The observation can be explained by Eq. (3.1), where diffusion (D') is inversely proportional to the particle size (r). So, for small size particles, there is large diffusivity, and consequently particles penetrate with more ease.

Next, numerical experiments are conducted for the microscale model to get insights of drug distribution at the cell scale. The schematic diagram with boundary conditions for the microscale model is displayed in Fig. 3.5. The results are displayed in Figs. 3.6(a) and (b) with two different values of K ($= 0.1, 1$). For $K = 0.1$, the cell membrane allows ten times lower concentration into the intracellular space from extracellular one (Fig. 3.6(a)). Fig. 3.6(c) displays the concentration distribution along the arrows shown in Figs. 3.6(a) and (b). The results show the heterogeneity in the concentration distribution at the cellular level. The rectangles R_1 and R_2 (in Fig. 3.6) display the solute accumulation on the cell membrane. This accumula-

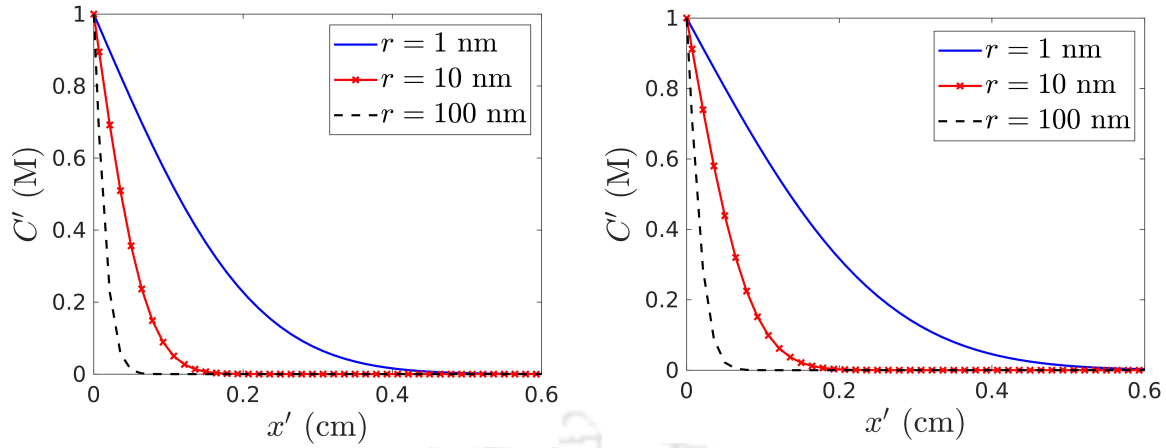

Figure 3.4: Effects of particle size on drug penetration (a) with partitioning $(K = 0.1)$ and (b) without partitioning $(K = 1)$.

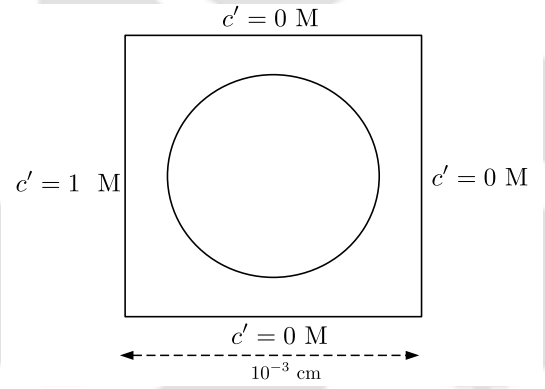

Figure 3.5: Schematic for the microscale problem to study concentration distribution at cell scale. The cell is chosen with the parameters $a_1 = a_2 = 3.1 \times 10^{-4}$ cm.

tion contributes to the reduction in penetration at the tissue scale. The accumulation of solute particles near the cell membrane surface is large in the case of partitioning $(K = 0.1)$. Thus, these simulation results explain that the reduction in tissue penetration efficacy of nanoparticles with partitioning is due to the solute accumulation near the cell membrane surface and limited availability of the main medium of transport, namely extracellular space. Fig. 3.6(d) displays the ratio of the concentrations at two consecutive grid points: one is in intracellular space and the other one is in the extracellular space. It can be seen that the quasi-equilibrium state is achieved at $\approx 10^{-6}$ h.

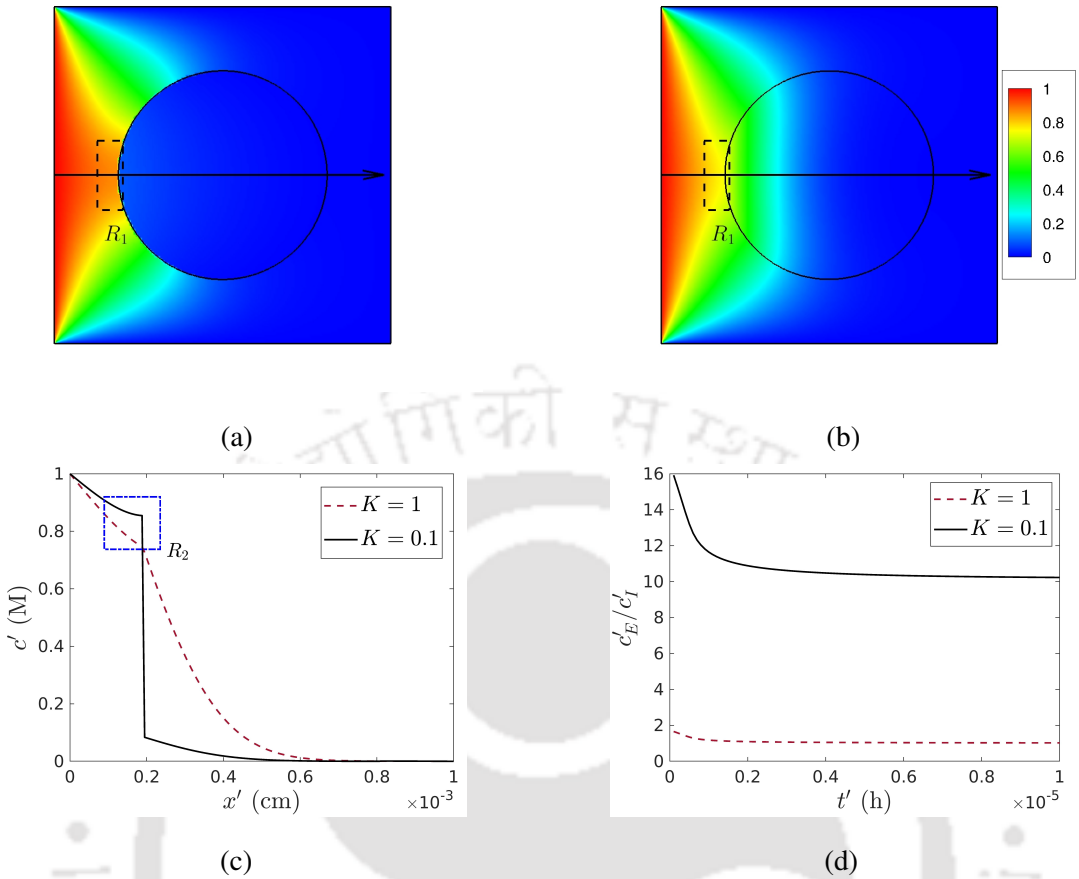

Figure 3.6: Simulation results for a typical microscale model. Results (a) with partitioning $(K = 0.1)$ and (b) without partitioning $(K = 1)$. (c) The concentration distribution along the arrows drawn in (a) and (b). (d) The ratio of concentration at first two consecutive x'-irregular Cartesian grid points (on arrow) vs. time (c'_E: concentration at extracellular grid point $(0.000503, 0.000805)$ and c'_I: concentration at intracellular grid point $(0.000503, 0.000812)$). The parameters are chosen as: $r = 1$ nm, $\mu_I = 5$ cP, $\mu_E = 1$ cP, and $t' = 10^{-5}$ h.

3.2.3 Effects of cell geometry

In literature, continuum models have been used at tissue scale in drug delivery problems. The models resolve the tissue scale and involve some parameters whose values are used to be constant (are known as one scale models). Some parameters are used to quantify tissue heterogeneity, such as extracellular volume. However, different cell geometry can lead to the same extracellular volume in the tissue domain, making one scale modelling inefficient. In this section, the FV-HMM is used to analyze the effects of cell geometry on penetration. Numerical experiments are performed with three different elliptical cells: the first one is having semi-

major axis along the x'-axis, the second one is having semi-major axis along y'-axis, and the last one is having both axes equal, i.e., forming a circular cell. All the experiments are conducted with two different values of K $(= 0.1, 1)$. The viscosity parameters are chosen as $\mu_I = 5$ cP and $\mu_E = 1$ cP, and the experiments are conducted for the penetration of 1 nm particles.

Figs. 3.7(a) and (b) display the results for different elliptical cells having the same area. Nanoparticles penetration for elliptical cells with semi-major axis along y'-direction is less than that for semi-major axis along x'-direction. Also, the penetration depths are significantly different with partitioning ($K = 0.1$). The findings can be explained as follows. Elliptical cells having a semi-major axis along y'-direction create a more cell membrane obstruction (Fig. 3.7(d)) in the direction of concentration gradient. Hence, there is a large accumulation of solute particles near the cell membrane and results in the reduction of penetration. In order to quantify the effects of cell geometry further, the results at point $x' = 0.1214$ for concentration versus cell width (a_1) are plotted in Fig. 3.7(c). It can be seen that as a_1 increases (results into a_2 to decrease) the concentration also increases. This is because, the cell is flatten out with the increase in a_1 and it leads to the large passage area, which subsequently allows more solute diffusion in deeper into the tissue. In these simulations, as the area occupied by the cell (in microscale domain) is kept fixed, the extracellular volume does not change; though the results on drug penetration are significantly affected by the change in cell shape. Thus, the cell geometry has a significant impact on tissue penetration efficacy of drug delivery nanoparticles.

Next, the numerical experiments are performed by changing the cell height and keeping cell width fixed, and vice versa. The results are displayed in Fig. 3.8. Fig. 3.8(a) displays the results for varying a_2 (cell height) while keeping a_1 (cell width) unchanged. It can be seen that the cell height affects drug penetration significantly, and the reduction in height results in more drug penetration. In Fig. 3.8(b), results are displayed for varying cell width (a_1) while keeping a_2 fixed. It can be seen that the cell width variation does not affect the penetration significantly. Thus, it can be concluded that the cell height has a significant impact on drug penetration rather than its width.

3.2.4 Effects of fluid viscosity

Biological fluid viscosity is a key parameter for the diffusivity of various constituents in tissues. Fluid viscosity varies across healthy to abnormal tissues [51, 19]. Here, the FV-HMM is employed to analyse the effects of viscosity variation on tissue penetration efficacy of nanopar-

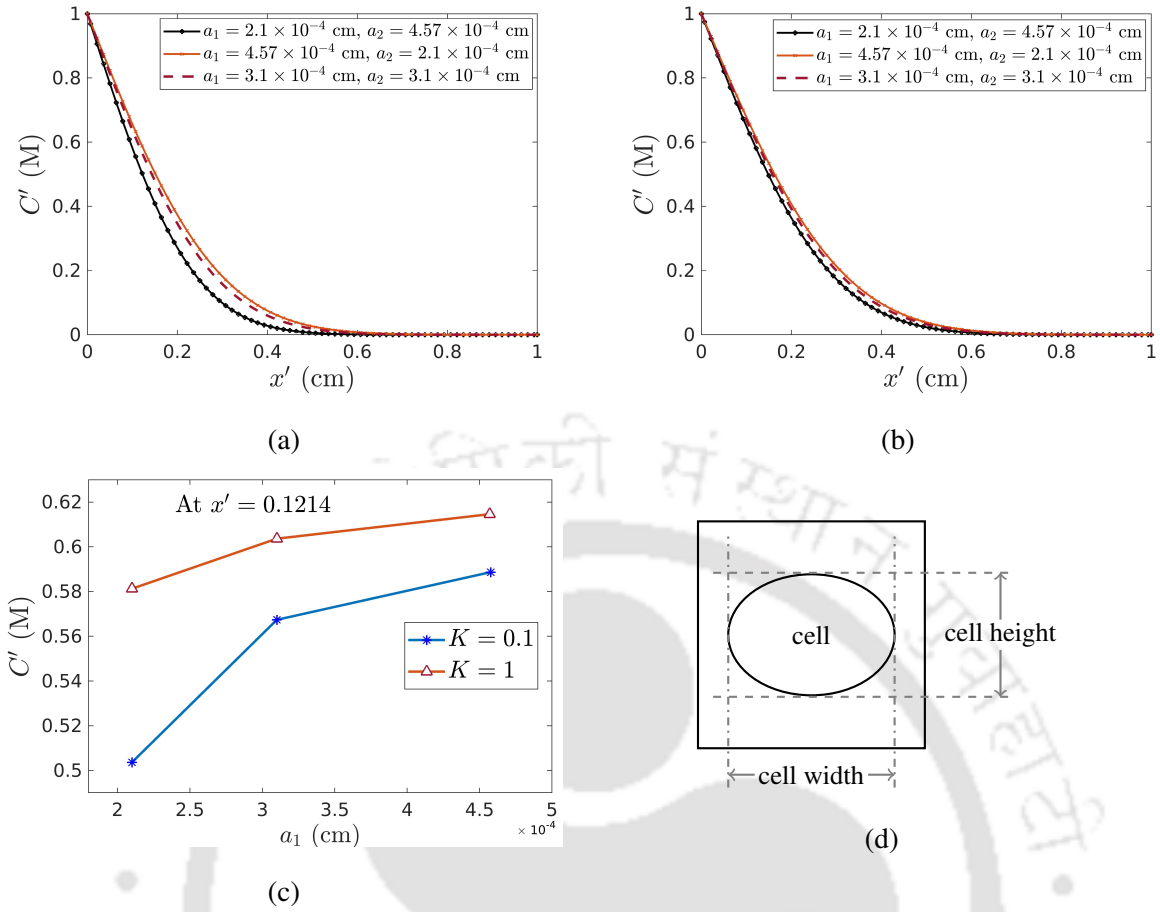

Figure 3.7: Effects of cell geometry on drug penetration (a) with partitioning $(K = 0.1)$ and (b) without partitioning $(K = 1)$. (c) The concentration at point $x' = 0.1214$. (d) Schematic for the cell height and cell width.

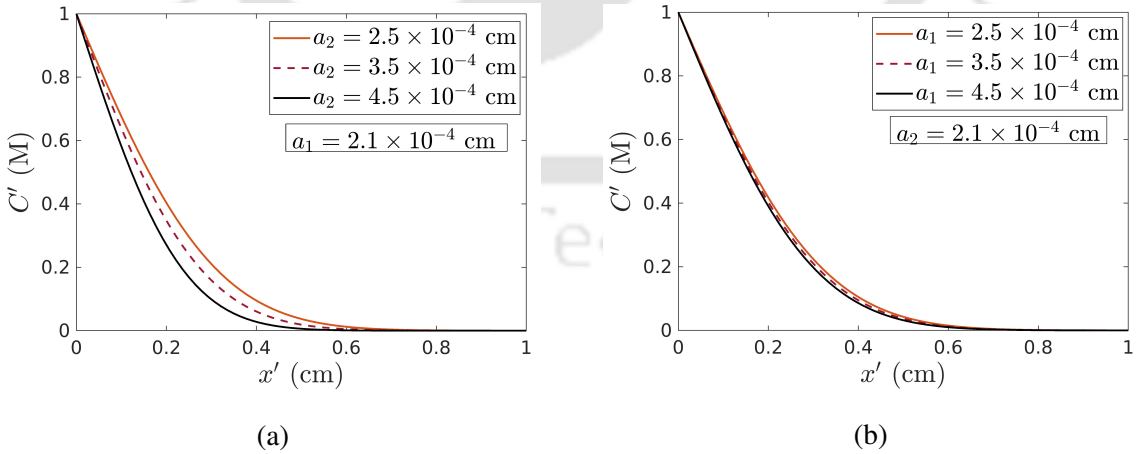

Figure 3.8: Effects of (a) cell height and (b) cell width with partition coefficient $K = 0.1$.

ticles. Two types of experiments are performed; one with varying intracellular viscosity and the other one with varying extracellular viscosity. The experiments are performed with $(K = 0.1)$

and without partitioning ($K = 1$) for 10 nm size particles. Figs. 3.9(a) and (b) display the effects of intracellular viscosity variation. On increasing intracellular viscosity, penetration depths are reduced significantly without partitioning ($K = 1$). However, partitioning shows no significant difference in penetration. It is because, with partitioning ($K = 0.1$), transport mainly happens in the extracellular space. Figs. 3.9(c) and (d) display the effects of extracellular viscosity variation. The change in extracellular viscosity affects the penetration with and without partitioning. Thus, it is observed that with partitioning, tissue penetration efficacy of nanoparticles is not affected due to the change in intracellular viscosity; however, extracellular viscosity may affect.

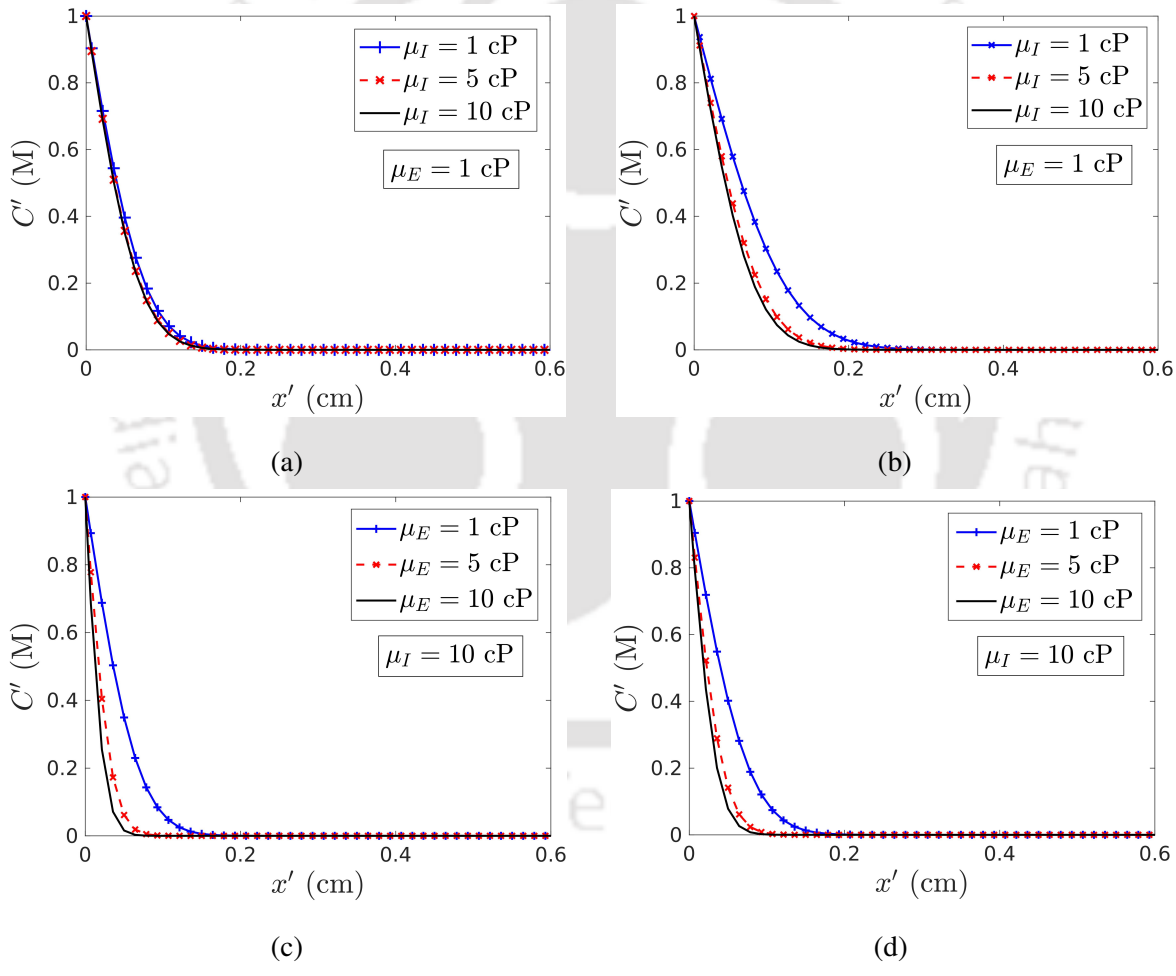

Figure 3.9: Effects of fluid viscosities on drug penetration. Intracellular fluid viscosity variation (a) with ($K = 0.1$) and (b) without partitioning ($K = 1$). Extracellular fluid viscosity variation (c) with ($K = 0.1$) and (d) without partitioning ($K = 1$).

3.3 Conclusions

In this chapter, the FV-HMM is simulated to analyse the effects of several factors such as partition coefficient, drug particle size, tissue micro-environment, and the cell geometry effects on the penetration and distribution efficacy of drug particles in the tissues. The investigations have revealed that the particle size and partition coefficient can play a significant role in the penetration of drug nanoparticles. The focus of this work is on 1–100 nm size particles. It is observed that the smaller size particles penetrate deeper compared to the larger ones. The partition coefficient can reduce the drug penetration significantly. The effects of cell geometry on drug penetration are also analyzed. It is observed that the different shapes of cell may lead to significantly different penetration distances despite the cell volume being kept fixed. The cell height is found to be a significant obstacle in the path of drug diffusion.

CHAPTER 4

EFFECTS OF CELL PERMEABILITY ON DRUG DELIVERY

The cell membrane poses a crucial barrier in permeation of drug particles in tissues [67]. The overall delivery of targeted nanoparticles across the cell membrane can be categorized in two ways: passive and active targeting [67]. The molecules that are small and moderately polar can diffuse across the cell membrane passively. However, largely polar and charged molecules do not permeate passively [67]. Researchers have suggested several numerical techniques to deal with selectively permeable membrane [18, 22, 39, 60]. In 2009, Huang et al. [22] proposed a permeable interface method based on the immersed boundary method (IBM) handling the interface with a smooth delta function. IBM was found to produce less accurate results as the permeability decreases gradually [49] and unable to handle non-permeable membranes [39]. Miyauchi et al. [39] presented a method using the finite element technique, and it was used for permeable and non-permeable membranes. In a recent article, Leedale et al. [33] studied the passive as well as the active mass transport across the membrane at the cell-scale. They used spherical coordinate system with radial symmetry in their model and analysed a single-cell model.

In this chapter, the passive diffusion of a drug across the cell membrane is included into the mass transport model (developed in Chapter 2). Accordingly, the FV-HMM is extended to the FVHMM-p. The resulted model comprises water-phase into intra- and extra-cellular spaces and selective permeability of a drug through the cell membrane due to the lipophilic profile. Across the cell membrane, as the diffusion coefficient may be discontinuous and solute transport takes place with restrictive permeability, the microscale model could be treated as an interface problem. This chapter also discusses a novel central-type finite difference based numerical scheme,

called as permeable interface method (PIM), to deal with the interface conditions. PIM can be used for permeable as well as non-permeable membrane and also for the irregular interface presents in the domain. It is found that the PIM produces better results in comparison with the ones available in literature.

Moreover, the FVHMM-p is employed to determine the penetration and distribution of drug particles in tissue. Numerical experiments are conducted to study the effects of cell membrane permeability, drug particle size, and intra- or extra-cellular volume on tissue penetration efficacy of drug particles. Investigations reveal that the cell membrane permeability may affect drug penetration significantly. The cell is considered to be elliptical, and the simulations with different configurations lead to pronounced effects on penetration of a drug at tissue scale irrespective of the cell membrane permeability.

4.1 Model formulation

The non-dimensional macroscale model is given by Eqs. (2.3)–(2.4), and its discrete version by (2.8). The macro flux needs to be estimated on each face of the CV (Fig. 4.1).

4.1.1 Microscale model

The microscale domain ω is a square domain and contains an elliptical cell placed at the centre of it (see Fig. 4.1(b)). The steady-state diffusion equation considered at the micro level is given as,

$$\nabla \cdot (D \nabla c(x, y)) = 0 \quad \text{in} \quad \omega, \tag{4.1}$$

where c denotes the microscopic concentration.

Cell membrane permeability

In order to study drug distribution in the tissue domain, it is necessary to understand how a drug gets distributed in the presence of biological cells. Subsequently, how does it penetrate across the cell membrane? The presence of phospholipids in the cell membrane show the hydrophobic characteristics to the water-soluble molecules and hence provides a barrier. Several factors affect the drug transport across the membrane, including passive diffusivity, protein binding, but the hydrophobicity that leads to the partition phenomenon is the key factor.

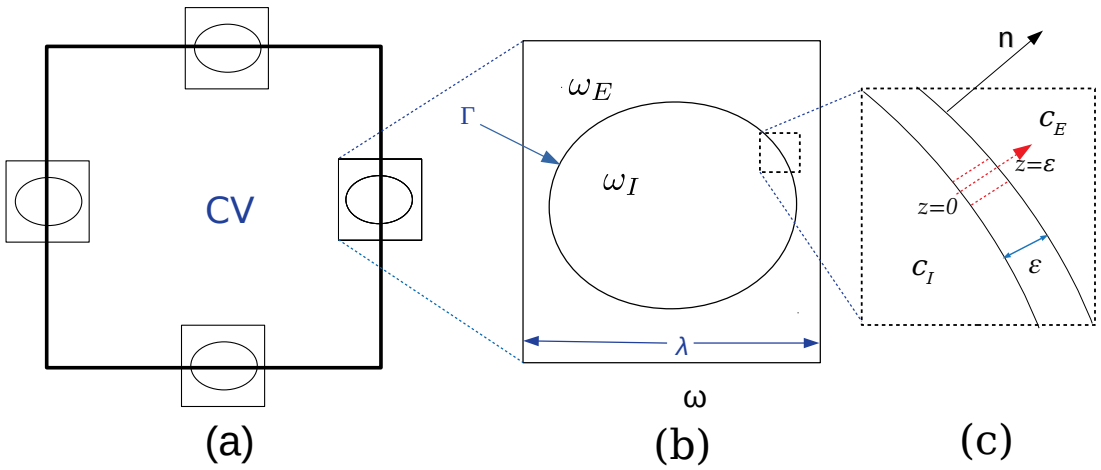

Figure 4.1: The hierarchy of the computational domain to couple the microscale model to the macroscale one. (a) A typical control volume, (b) a typical microscale domain, and (c) the zoomed-version of cell membrane of width ε.

The cell membrane width that varies between 5–10 nm, is negligible compared to the cell scale. Also, the passive diffusion across the cell membrane happens through the channels. So, the diffusion of solute particles of relatively smaller size ($\approx$ 1 nm) can be modelled as one-dimensional (in the normal direction) [60], as depicted in Fig. 4.1(c). Thus, the steady-state one-dimensional diffusion equation along the normal direction (**n**) is given as,

$$\frac{d}{dz}\left(D_m \frac{dc_m}{dz}\right) = 0, \tag{4.2}$$

where D_m is the solute transmembrane diffusion coefficient. As the intra- and extra-cellular fluids are very different in their properties, like protein contents, the partition coefficient may be different: one, where solute enters from extracellular space to lipid membrane or vice versa, and second, when solute moves from lipid membrane to the intracellular fluid or vice versa. Thus, the partitioning conditions at $z = 0$ and $z = \varepsilon$ (depicted in Fig. 4.1(c)) can be written as,

$$c_m(0) = K_1 c_I \quad \text{and} \quad c_m(\varepsilon) = K_2 c_E, \tag{4.3}$$

respectively. Now, the equation (4.2) says that

$$D_m \frac{dc_m}{dz} = \text{constant} = j, \tag{4.4}$$

which is a transmembrane flux (j). Note that j is a scalar as it is one-dimensional quantity. For this work, it is assumed that the transmembrane diffusion coefficient is constant. The solution

of the above differential equation can be written as,

$$c_m = \frac{j}{D_m} z + A, \tag{4.5}$$

for some constant A. Now, the use of (4.3) leads to

$$j = \frac{D_m}{\varepsilon} \left(K_2 c_E - K_1 c_I \right). \tag{4.6}$$

This is a general expression for flux across the cell membrane whose two sides are occupied with different fluids. In the following, we choose $K_1 = K_2 = K$, then

$$j = \frac{D_m K}{\varepsilon} \left(c_E - c_I \right). \tag{4.7}$$

Note that, as $\varepsilon << \lambda$, $\varepsilon \to 0$ compared to the cell scale; the normal flux vector $(\mathbf{J})$ can be taken as $\mathbf{J} = j\mathbf{n}$. Thus, the permeability (P) of the cell membrane is related to the partition coefficient (K) as,

$$P = \frac{D_m K}{\varepsilon}. \tag{4.8}$$

The cell membrane is taken to be a sharp interface in the computational domain. With this assumption, diffusion of large size particles can also be studied. However, in practice, there is negligible passive diffusion of large particles due to the availability of small pores only in the membrane.

Interface conditions

The metabolism or deactivation of drug across the cell membrane is not considered here, so the interface conditions are used as [22, 33]:

$$D_E \nabla c_E = D_I \nabla c_I = P(c_E - c_I)\mathbf{n}. \tag{4.9}$$

Here, P is related to the dimensional permeability (P') as, $P = P'\tilde{L}/\tilde{D}$.

4.1.2 Simulation of microscale model

The boundary values for the micro state variable (c) are obtained using the linear interpolation of macroscopic concentrations, as discussed in Chapter 2 (Section 2.2). The microscale models are solved using the permeable interface method (PIM) presented for permeable membranes in Section 4.2. The outcomes of the microscale models are used to estimate the macro flux as discussed in Chapter 2 (Section 2.2.4).

4.2 Permeable interface method (PIM)

In this section, an interface method is discussed, which is presented in the context of microscale model in FVHMM-p.

4.2.1 Model formulation

Consider the physical domain ω as shown in Fig. 4.2 and its boundary is denoted by $\partial\omega$. The interface Γ is given by Eq. (2.23).

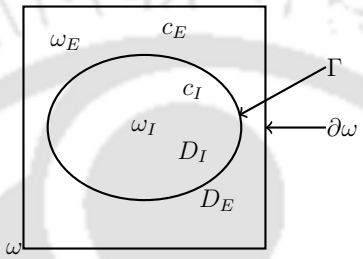

Figure 4.2: Schematic diagram of ω and the elliptical interface Γ. Here, I is used to showing the intracellular quantity and E for the extracellular one.

For application in the FVHMM-p (microscale model), the two-dimensional elliptic-type interface problem is considered as:

$$\nabla \cdot (D(x,y)\nabla c) = 0, \quad (x,y) \in \omega, \tag{4.10}$$

for prescribed boundary condition

$$c(x,y) = c_b, \quad (x,y) \in \partial\omega, \tag{4.11}$$

and the interface condition

$$D_E \nabla c_E = D_I \nabla c_I = P(c_E - c_I)\mathbf{n}. \tag{4.12}$$

4.2.2 Numerical method

Without loss of generality, ω is considered a unit square domain. It is discretized as discussed in Section 2.3. The classification for the grid points predominantly needed for the discretization of model near the interface are used as discussed in Chapter 2 (Section 2.3, depicted in Fig. 2.9).

The model (Eq. 4.10) is discretized using the central-difference at regular grid points as,

$$\left(\delta_x \left(D\delta_x c\right)\right)_{i,j} + \left(\delta_y \left(D\delta_y c\right)\right)_{i,j} = 0, \tag{4.13}$$

where

$$\left(\delta_x \left(D\delta_x c\right)\right)_{i,j} = \left\{ \frac{D_{i+1/2,j}c_{i+1,j} - (D_{i+1/2,j} + D_{i-1/2,j})c_{i,j} + D_{i-1/2,j}c_{i-1,j}}{(\delta x)^2} \right\}$$

and

$$\left(\delta_y \left(D\delta_y c\right)\right)_{i,j} = \left\{ \frac{D_{i,j+1/2}c_{i,j+1} - (D_{i,j+1/2} + D_{i,j-1/2})c_{i,j} + D_{i,j-1/2}c_{i,j-1}}{(\delta y)^2} \right\}.$$

In the following, difference operators for x-directional derivative are discussed, and the index j is omitted for the sake of brevity. At the x-irregular grid point i (shown in Figs. 2.9 and 4.3a), the central-type difference operator is used as,

$$\left(\delta_x \left(D\delta_x c\right)\right)_i = \left\{ D_{i+\theta/2} \frac{c^-_{i+\theta} - c_i}{x_{i+\theta} - x_i} - D_{i-1/2} \frac{c_i - c_{i-1}}{x_i - x_{i-1}} \right\} \Bigg/ \left(\frac{x_{i+\theta} - x_{i-1}}{2} \right), \tag{4.14}$$

where $x_{i+\theta} = x_i + \theta\delta x$ for some $0 < \theta < 1$. For the case where a Cartesian grid point is surrounded by two interfacial points (as in Fig. 4.3(b)), the central-type difference operator is used as,

$$\left(\delta_x \left(D\delta_x c\right)\right)_i = \left\{ D_{i+\theta_1/2} \frac{c^-_{i+\theta_1} - c_i}{x_{i+\theta_1} - x_i} - D_{i-\theta_2/2} \frac{c_i - c^+_{i-\theta_2}}{x_i - x_{i-\theta_2}} \right\} \Bigg/ \left(\frac{x_{i+\theta_1} - x_{i-\theta_2}}{2} \right), \tag{4.15}$$

where $x_{i+\theta_1} = x_i + \theta_1\delta x$ and $x_{i-\theta_2} = x_i - \theta_2\delta x$ for some $0 < \theta_1, \theta_2 < 1$.

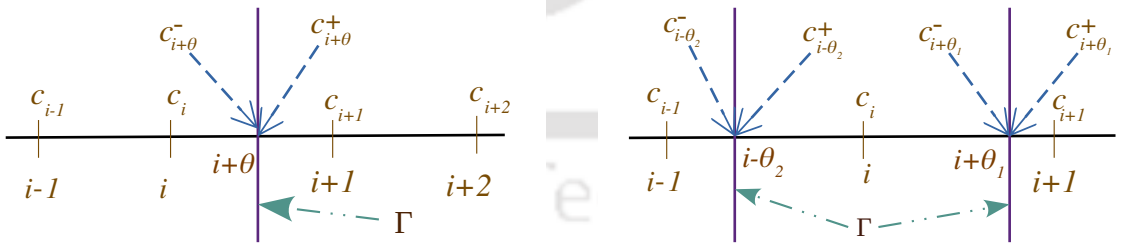

(a) (b)

Figure 4.3: Treatment of drug concentration at the interfacial point. (a) Single interfacial point $i + \theta$ around i and (b) two interfacial points $i + \theta_1$ and $i - \theta_2$ surrounds Cartesian grid point i.

In order to make the relation (4.14) well-defined, $c^-_{i+\theta}$ needs to be evaluated. Limiting concentrations are obtained using the linear interpolation and the interface conditions. The interpolating polynomials $L^-(x)$ and $L^+(x)$ are given by Eqs (2.36) and (2.37), respectively.

In order to determine $c^+_{i+\theta}$ and $c^-_{i+\theta}$ uniquely, there is a need of two equations. The interface condition (4.12) is imposed to get the results consistent with the permeable membrane. To rope in the discretization of derivative along x-direction, the x-component of (4.12) can be taken as,

$$D_I \frac{\partial c_I}{\partial x} = D_E \frac{\partial c_E}{\partial x} = P(c_E - c_I)\cos\phi, \tag{4.16}$$

where ϕ is the angle made by outward unit normal **n**.

So, the limiting concentrations are obtained from the equations

$$D_E \frac{\partial c_E}{\partial x} - D_I \frac{\partial c_I}{\partial x} = 0, \tag{4.17}$$

$$D_I \frac{\partial c_I}{\partial x} = P(c_E - c_I)\cos\phi. \tag{4.18}$$

Differentiating $L^-(x)$ and $L^+(x)$ with respect to x and substituting into equation (4.17) one gets,

$$\kappa^+ c^+_{i+\theta} + \kappa^- c^-_{i+\theta} = \kappa^+ c_{i+1} + \kappa^- c_i, \tag{4.19}$$

where $\kappa^+ = \frac{D^+_{i+\theta}}{x_{i+1}-x_{i+\theta}}$ and $\kappa^- = \frac{D^-_{i+\theta}}{x_{i+\theta}-x_i}$. Note that $\frac{\partial c_I}{\partial x} \approx \frac{\partial L^-(x)}{\partial x}\big|_{x=x_{i+\theta}}$ and $\frac{\partial c_E}{\partial x} \approx \frac{\partial L^+(x)}{\partial x}\big|_{x=x_{i+\theta}}$ for $i \in \omega_I$, whereas the roles of c_I and c_E are interchanged for $i \in \omega_E$. Equation (4.18) can be written as,

$$\alpha_1 c^+_{i+\theta} + \alpha_2 c^-_{i+\theta} = -\kappa^- c_i \tag{4.20}$$

for some α_1 and α_2 as discussed below. From (4.19) and (4.20) one can obtain

$$c^-_{i+\theta} = \frac{1}{X}\left[\beta_1 c_{i+1} + \beta_2 c_i\right], \tag{4.21}$$

$$c^+_{i+\theta} = \frac{1}{X}\left[\gamma_1 c_{i+1} + \gamma_2 c_i\right]. \tag{4.22}$$

The parameters $X, \beta_1, \beta_2, \gamma_1,$ and γ_2 are given as follows.
If $\eta = P\cos\phi$, then for x-irregular grid point $i \in \omega_I$,

$$\alpha_1 = \eta,\ \alpha_2 = -\eta - \kappa^-,\ \beta_1 = \kappa^+\eta,\ \beta_2 = \kappa^-\left(\kappa^+ + \eta\right),$$
$$X = -\kappa^+\alpha_2 + \kappa^-\eta,\ \gamma_1 = -\kappa^+\alpha_2,\ \gamma_2 = \kappa^-\eta,$$

and for x-irregular grid point $i \in \omega_E$,

$$\alpha_1 = -\eta,\ \alpha_2 = \eta - \kappa^-,\ \beta_1 = \kappa^+\eta,\ \beta_2 = -\kappa^-\left(\kappa^+ - \eta\right),$$
$$X = \kappa^+\alpha_2 + \kappa^-\eta,\ \gamma_1 = \kappa^+\alpha_2,\ \gamma_2 = \kappa^-\eta.$$

Similarly, to rope in y-direction discretization, the following equation is used (y-component of (4.12)),

$$D_I \frac{\partial c_I}{\partial y} = D_E \frac{\partial c_E}{\partial y} = P(c_E - c_I) \sin \phi. \tag{4.23}$$

The procedure to discretize the derivative along y-direction is similar to that for x-direction. In the case where the Cartesian grid point is same as the interfacial point, the treatment is adopted as suggested by Mittal and Ray [38].

The resulted system of equations is a sparse five-banded system, and it is solved using the BiCGSTAB algorithm without preconditioning [46]. In all the simulations in this chapter, BiCGSTAB iterations are terminated when the maximum error between the previous and updated solution falls below 10^{-15}.

4.3 Numerical experiments: validation and error analysis

The numerical multiscale method, developed in this chapter, consists of two major components. First, PIM, which is used to discretize the microscale model, and second, the overall multiscale algorithm (FVHMM-p). Thus, the validation is required for PIM and the FVHMM-p algorithm separately. In this section, the error analysis and validation are performed for the PIM, and the validation of results for the FVHMM-p is presented in the Section 4.4.1.

4.3.1 PIM

The PIM is tested on one-dimensional (1D) and two-dimensional (2D) problems. For 1D problem, an analytical solution is constructed with general parameters and for 2D one, as no analytical solution is available, results are compared with the existing numerical results [39].

1D problem

Problem 4. In the case of 1D, the interface problem given by Eqs. (4.10)–(4.12) can be stated as,

$$\frac{d}{dx}\left(D(x)\frac{dc}{dx}\right) = 0 \tag{4.24}$$

with interface conditions (at $x = x_0$),

$$D_l \frac{dc_l}{dx} = D_r \frac{dc_r}{dx} = P(c_l - c_r), \tag{4.25}$$

where the subscripts l and r denote the left and right limiting values, respectively, at the interface $x = x_0$.

For $0 < x < 1$, the analytical solution of (4.24)–(4.25) with boundary conditions $c(0) = c_0$ and $c(1) = c_1$ and the diffusion coefficient

$$D(x) = \begin{cases} D_l, & \text{for } x \le x_0, \\ D_r, & \text{for } x > x_0, \end{cases} \tag{4.26}$$

is given by

$$c(x) = \begin{cases} Ax + c_0, & \text{for } 0 \le x \le x_0, \\ F(x-1) + c_1, & \text{for } x_0 < x \le 1, \end{cases} \tag{4.27}$$

where

$$F = \frac{-PD_l}{D_l(P(x_0-1) - D_r) - PD_r x_0} \quad \text{and} \quad A = \frac{P(F(x_0-1)+1)}{D_l + Px_0}.$$

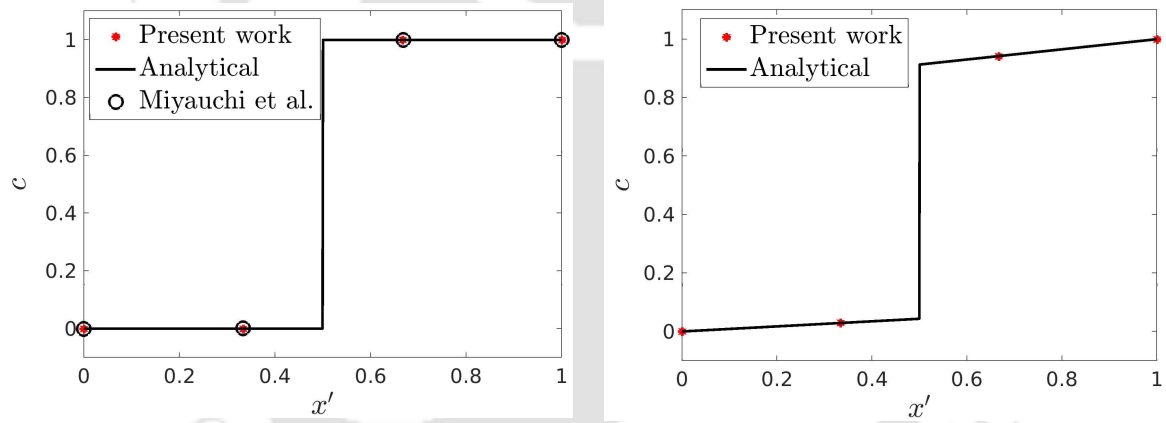

(a) (b)

Figure 4.4: Simulation results of PIM and Miyauchi et al. [39] along with the analytical solution. The parameters are (a) $D_l = D_r = 1$, $P = 0$ and (b) $D_l = 1$, $D_r = 0.5$, $P = 0.1$. The interface is located at $x_0 = 0.5$.

Fig. 4.4 compares the PIM results with the analytical solution and the numerical results of Miyauchi et al. [39]. First, the cell membrane is taken to be impermeable ($P = 0$), and the results are displayed in Fig. 4.4(a). Second, the results are displayed for $P = 0.1$ in Fig. 4.4(b). In both the cases, the interface is considered at $x = 0.5$. Four grid points are taken in the mesh and two of them are interior points. The order of maximum error is around 10^{-18}; this small error could be due to the contribution from the round off error (machine accuracy). Whereas, in the article by Miyauchi et al. [39], maximum error was noticed to be of order

10^{-16}. Despite the very crude mesh and discretization, PIM has produced very accurate results, even for smaller permeability values.

2D problem

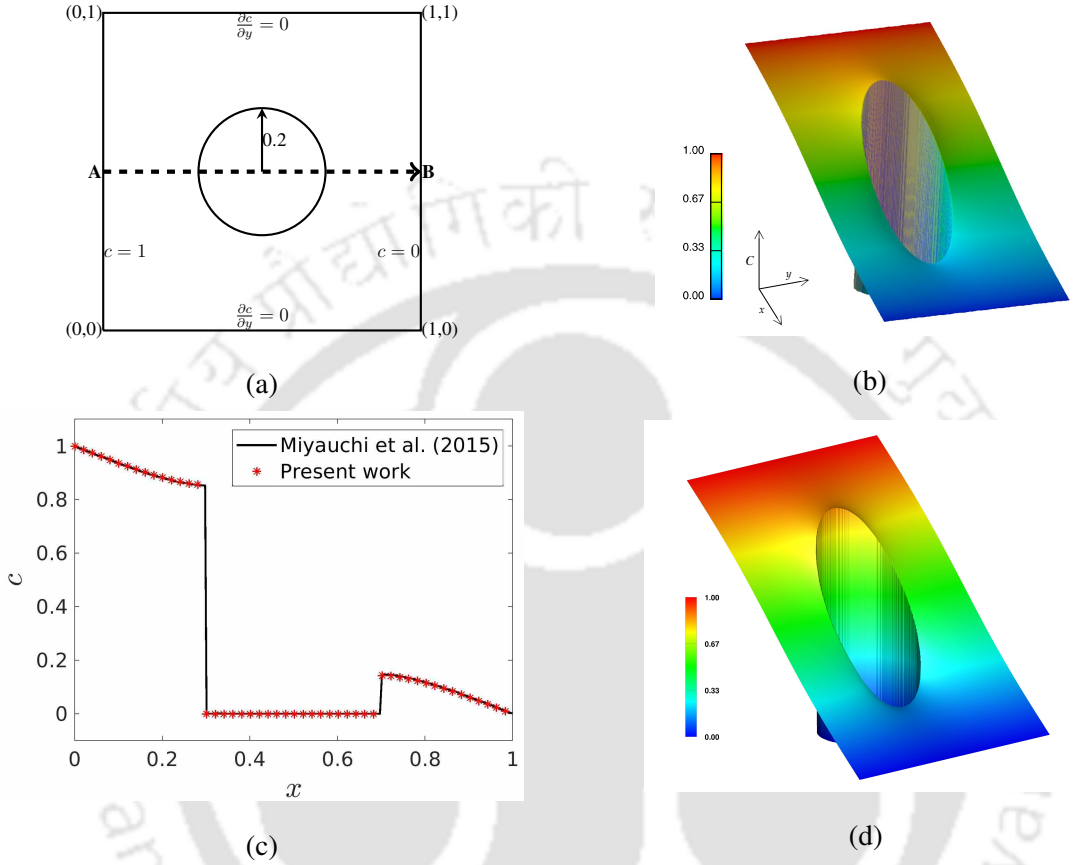

Figure 4.5: (a) Schematic of computational domain. The three-dimensional contour plots; (b) Miyauchi et al. [39], and (d) present work (PIM). (c) The concentration distribution along the line **AB**.

Problem 5. In the case of 2D, the interface problem is given by Eqs (4.10)–(4.12). For validation, a circular membrane is considered at the centre of $\omega : 0 \leq x, y \leq 1$. An illustration of the computational domain is shown in Fig. 4.5(a) and the boundary conditions are also depicted there. The cell is assumed to be impermeable $(P = 0)$ and $D = 1$ in intra- and extra-cellular spaces. The parameter values and the boundary conditions are chosen in accordance with the available work [39].

The contour plots from Miyauchi et al. [39] (at 400×400 finite element nodes) and PIM (at 400×400 mesh size) are displayed in Figs. 4.5b and 4.5d, respectively. Also, the concentration

distribution along the line **AB** corresponds $y = 0.5$ (see Fig. 4.5(a)), for both the contours, is shown in Fig. 4.5(c). By comparing, one can see that the PIM results are in good agreement with that of Miyauchi et al. [39].

Problem 6. The comparison is also made with the microscale model (IIM) used in the FV-HMM. If K is taken to be zero (Eq. (2.11)), no solute will be allowed to move across the interface separating intra- and extra-cellular spaces. The same situation will also arise in the case of zero permeability ($P = 0$) in the PIM. Note that, $P = 0$ can also be obtained by setting $K = 0$ in Eq. (4.8). Thus, PIM is comparable with the IIM. For the simulation, a circular cell is considered at the centre of domain $0 \leq x, y \leq 1$ with radius 0.31. The concentration is set to be $c = 1$ at the left boundary and zero elsewhere, and $D = 1$ is chosen in intra- and extra-cellular spaces.

Fig. 4.6 displays the results of IIM at steady-state and of the PIM (on mesh size 400×400). It shows that there is a good match in the results.

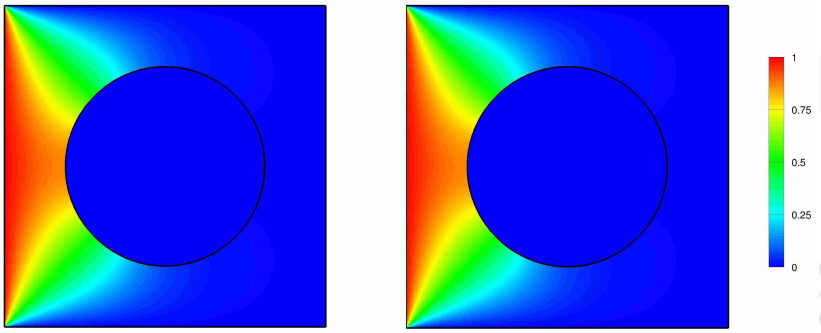

Figure 4.6: A comparison between the PIM (left) and the IIM (right) results.

Error analysis

The error analysis for the PIM is performed for problem 6 with three choices of permeability values. As the analytical solution is not known, the solution at very fine mesh (1281×1281) is used as analytical one to calculate the maximum errors. The order of convergence at the current mesh size δx is obtained as,

$$\text{Order} = \frac{\log(||E_{\delta x'}||_\infty / ||E_{\delta x}||_\infty)}{\log 2}, \tag{4.28}$$

where $\delta x' = 2\delta x$. $||E_{\delta x}||_\infty$ denotes the maximum error.

Maximum errors and the orders of accuracy are shown in table 4.1 for various grid sizes. Clearly, one can see that the solution converges on mesh refinement. The orders of convergence are similar for $P = 0.001, 0.1,$ and 1. Hence, it is evident that for 2D problem the method does not loose the convergence rate for smaller values of P. Whereas, in Sherk [49], it was noticed that the IBM method produces less accurate results for low permeable membranes. However, PIM has produced results of similar accuracy for any permeability values. Thus, PIM has additional features compared to the previous methods and hence, it could be a robust approach for permeable or impermeable interface problems. It is asymptotically first-order accurate; though, the central-difference discretization is used at the regular grid points. This is because the central-type scheme used at the irregular grid points is first-order accurate on non-uniform stencil. Also, the linear Lagrange interpolating polynomials are used to obtain the interfacial values.

Table 4.1: Maximum error estimates and the orders of convergence for the PIM.

$M_x = M_y$	$P = 0.001$		$P = 0.1$		$P = 1$	
	$\|\|E_{\delta x}\|\|_\infty$	Order	$\|\|E_{\delta x}\|\|_\infty$	Order	$\|\|E_{\delta x}\|\|_\infty$	Order
41	1.046×10^{-2}	—	1.021×10^{-2}	—	8.663×10^{-3}	—
81	4.361×10^{-3}	1.262	4.270×10^{-3}	1.257	3.718×10^{-3}	1.220
161	1.439×10^{-3}	1.598	1.405×10^{-3}	1.603	1.203×10^{-3}	1.627
321	6.814×10^{-4}	1.079	6.656×10^{-4}	1.078	5.697×10^{-4}	1.078

4.4 Results in drug delivery

In this section, the effects of cell membrane permeability, drug particle size, intra- or extra-cellular volume, and the cell geometry effects on penetration and distribution of drug particles in tissue are studied. The diffusion coefficient is evaluated from the Stokes-Einstein relation given by Eq. 3.1. The schematic diagram for the geometry of tissue domain along with initial and boundary conditions is shown in Fig. 4.7(a). The discretization and parameters are chosen according to Section 3.1.

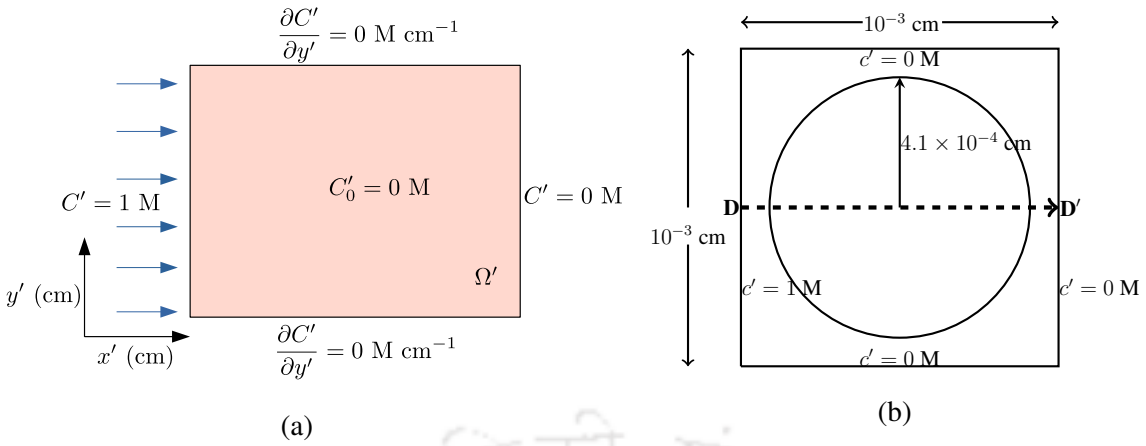

Figure 4.7: (a) An illustration of the tissue computational domain and (b) the schematic of a single-cell computational domain.

4.4.1 The convergence and validation for the FVHMM-p

In this section, convergence of the FVHMM-p for drug delivery problem is discussed, and a validation with the experimental results is also presented.

Convergence analysis

In the chosen finite volume discretization, grid points do not coincide for different macro-spatial grid sizes; so, the errors are calculated with the help of cubic spline polynomial. The functions 'spline' and 'ppval' available in the MATLAB [37] are used for the calculation of concentration at common points for different mesh sizes. The errors on grid refinement for the FVHMM-p algorithm with two permeability values $P' = 0.1$ and 0.001 cm/h are depicted in Table 4.2. It clearly shows that the maximum errors decrease with macro-spatial grid refinement; hence, the convergence is established for the FVHMM-p.

Table 4.2: Maximum error estimates on macro-spatial grid refinement for the FVHMM-p.

Grid	$P' = 0.1$	$P' = 0.001$
	$\|\|E_h\|\|_\infty$	$\|\|E_h\|\|_\infty$
(13×1) vs. (25×1)	5.400×10^{-3}	5.500×10^{-3}
(25×1) vs. (50×1)	1.819×10^{-4}	1.827×10^{-4}
(50×1) vs. (100×1)	4.572×10^{-5}	4.592×10^{-5}

Comparison with the FV-HMM and existing experimental results

Next, the FVHMM-p is validated with the experimental result of Huang et al. [23]. They studied the nanoparticles penetration and accumulation in the spheroid-on-chip system formed by fixing multicellular spheroids into a microfluidic chip, an *in vitro* setup. The comparison is made with the parameters $D'_E = 1.8 \times 10^{-7}$ cm^2/h, $D'_I = 10^{-8}$ cm^2/h, and $P' = 0.1$ cm/h. The calculation of permeability value involves the transmembrane diffusivity, partition coefficient, and the width of the cell membrane as, 10^{-9} cm^2/h, 15, and 7.5×10^{-7} cm (7.5 nm), respectively. The numerical experiments are conducted for $t' = 2$ h in the macroscale domain $[0, 0.01] \times [0, 0.01]$. Fig. 4.8 shows the numerical results of the FV-HMM and FVHMM-p along with the experimental result of Huang et al. [23]. One can observe that the FVHMM-p results are in good agreement with the experimental values; whereas, the FV-HMM overestimates the drug penetration.

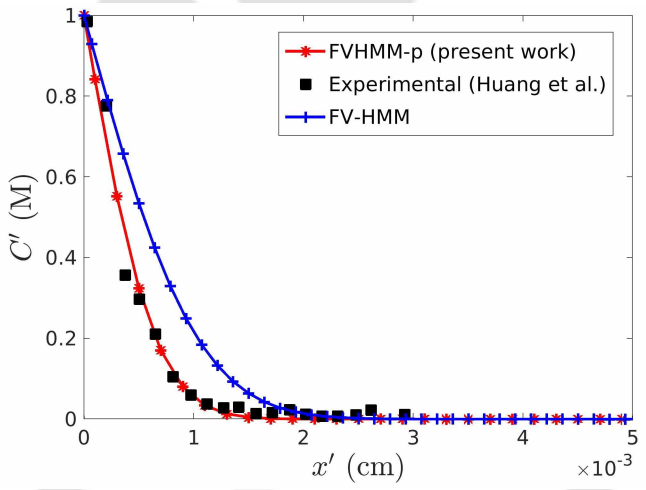

Figure 4.8: Numerical results of the FV-HMM and FVHMM-p along with the experimental results of Huang et al. [23].

The overestimation in penetration with the FV-HMM can be explained as follows. In the FV-HMM, the intracellular fluid phase is considered hydrophobic to the water-phase (extracellular fluid), and the partition coefficient is incorporated through the interface condition across the cell membrane given by Eq. (2.11). However, in physiological conditions, the cell membrane is hydrophobic to the water-phase and the intra- and extra-cellular spaces are filled with the fluid phase (water-soluble). Also, the selective permeable property of membrane modelled as the cell membrane permeability in the FVHMM-p is ignored in the FV-HMM. Hence, for larger K (typically $K > 1$), the FV-HMM overestimates the drug penetration.

However, for $K = 0$, the FVHMM-p results are comparable with the ones of the FV-HMM. The viscosity parameters are chosen as, $\mu_I = 5$ cP and $\mu_E = 1$ cP. Simulations are performed for two choices of cell: circular and elliptical, for circular, $a_1 = a_2 = 4.1 \times 10^{-4}$ cm while for elliptical, $a_1 = 4.1 \times 10^{-4}$ cm and $a_2 = 3.1 \times 10^{-4}$ cm. The results are obtained for $t' = 5$ h. Note that, the FVHMM-p and FV-HMM problems are effectively 1D with some effective diffusion coefficient D_{eff}. The effective diffusion coefficients (D_{eff}) are chosen as 2.6×10^{-3} cm^2/h and 4×10^{-3} cm^2/h for the case of circular and elliptical cells, respectively. Fig. 4.9 displays the concentration distribution in the tissue domain for the FV-HMM, FVHMM-p, and the analytical solution (Eq. 3.2). For both the types of cells, there is a very good agreement among the results.

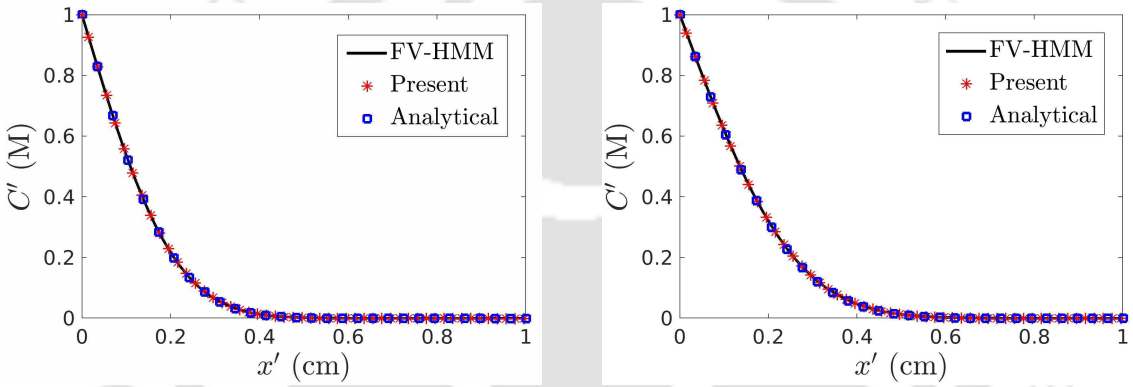

(a) (b)

Figure 4.9: Comparisons of the FV-HMM ($K = 0$) and FVHMM-p (for $P = 0$) results with the choice of (a) circular and (b) elliptical cells.

4.4.2 Effects of cell membrane permeability

In this section, the effects of cell membrane permeability on the penetration of drug particles are studied in the context of single-cell model and tissue scale model separately. The computational domain for the single-cell model is displayed in Fig. 4.7(b). This geometry is also used for microscale models in tissue scale simulations; however, the boundary conditions are evaluated in the way as discussed in Section 2.2. With different permeability parameters, numerical experiments are conducted for $r = 1$ and 10 nm (nm – nanometre, where 1 nm = 10^{-7} cm) particles. The fluid viscosity is chosen in two ways (say cases): in case-I, intra- and extra-cellular fluid viscosities are taken to be equal ($\mu_I = \mu_E = 2.5$ cP), while in case-II, $\mu_I > \mu_E$.

For case-I, the concentration distribution of 1 nm particles is displayed in Fig. 4.10. Fig. 4.10(a) displays the concentration distribution along the arrow **DD′** (see Fig. 4.7(b)) for single-cell model. It can be seen that the concentration is discontinuous and the jump is large across the cell membrane for smaller values of P' and tends towards continuity as P' approaches infinity. The drug accumulation is large in proximity of the cell membrane (see rectangle R_1 in Fig. 4.10(a)) due to the selective permeability. Fig. 4.10(b) displays the concentration distribution in the tissue domain. The drug penetrations are significantly different for different values of P' (ranging in $[0.1, 100]$). For larger values of P' ($\approx$ 100 cm/h), the solute penetration is approximately two times deeper than for smaller ones ($P' \approx 0.1$ cm/h). Thus, for this case, the cell membrane permeability has a pronounced effect on drug penetration in the tissue domain.

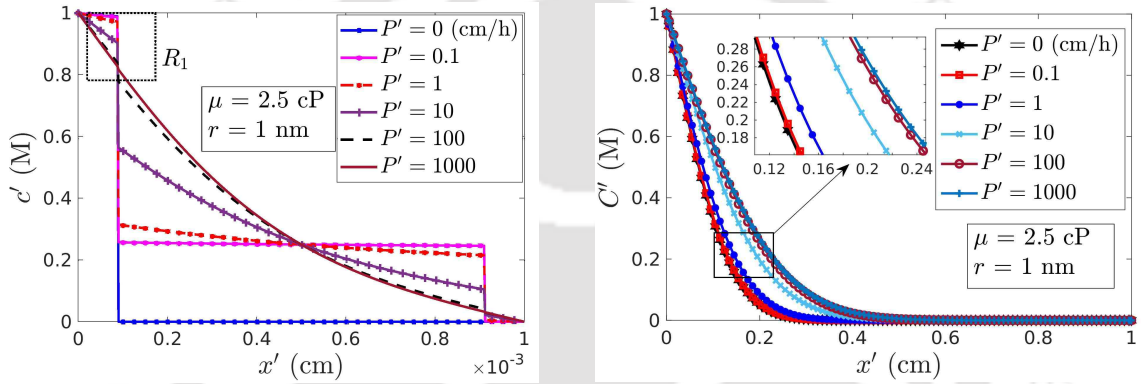

(a) (b)

Figure 4.10: Simulation results of 1 nm particles for equal fluid viscosity ($\mu_I = \mu_E = 2.5$ cP) in intra- and extra-cellular spaces. (a) Single-cell model and (b) tissue scale model.

Next, the numerical experiments are conducted for the choice of fluids viscosities according to the case-II. Two different values are chosen for μ_I as 5 and 10 cP, and $\mu_E = 1$ cP. These choices of intracellular viscosity parameter are realistic, as the intracellular environment is occupied with macromolecules that hinder the diffusion substantially. Results for the single-cell model are shown in Fig. 4.11(a). It can be noticed that the concentration is discontinuous even for the larger values of P' than the case-I (Fig. 4.10(a)). Consequently, for case-I, there are large variations in drug accumulation with permeability (rectangle R_1 in Fig. 4.10(a)) but moderate in the case-II (rectangle R_1 in Fig. 4.11(a)).

Fig. 4.11(b) displays the concentration distribution in tissue domain for $\mu_I = 5$ cP. However, in Fig. 4.11(c), the concentrations are plotted against the permeability at point $x' = 0.195$ for $\mu_I = 5$ and 10 cP. For $\mu_I = 5$ cP, there is approximately 0.1 M (10 % of 1 M, the con-

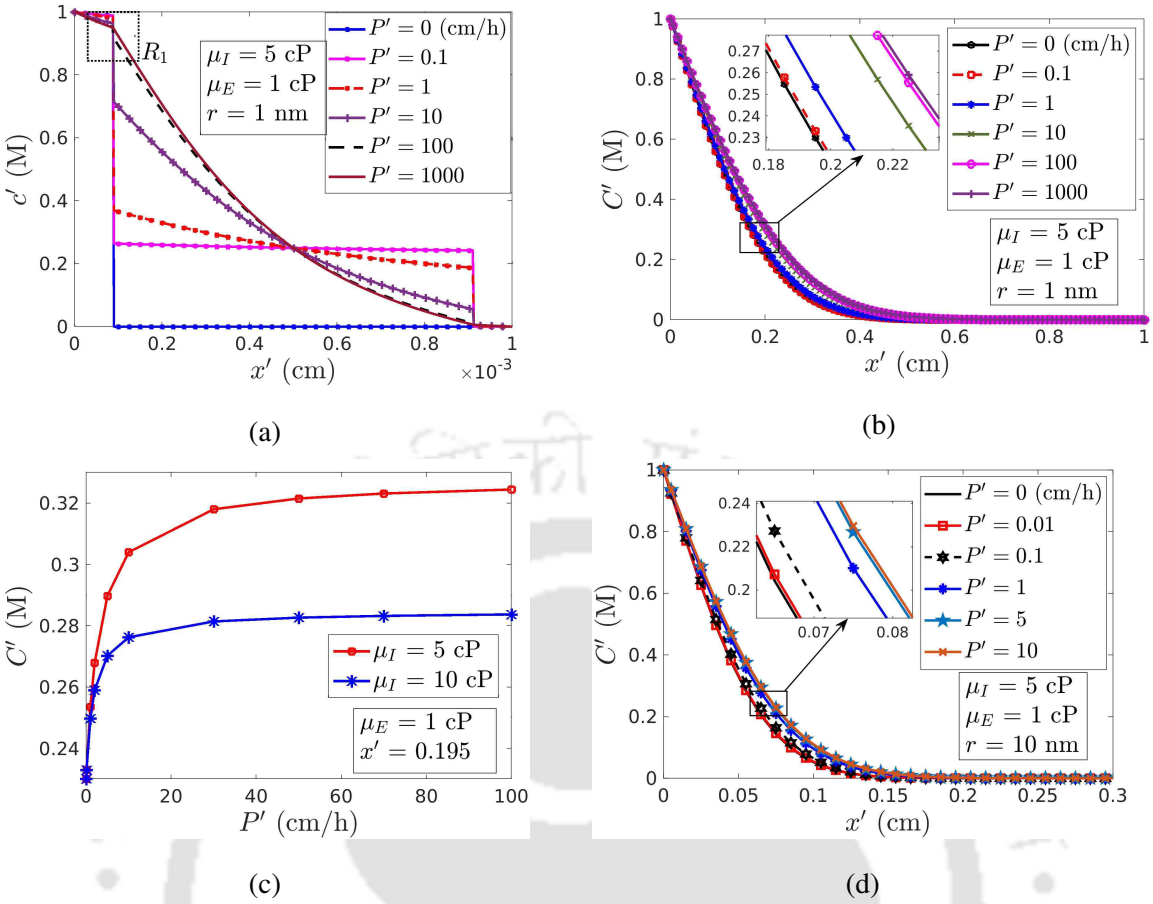

Figure 4.11: Effects of cell permeability on penetration and distribution of 1 and 10 nm drug particles (fluid viscosity as case-II). (a) A single-cell model and (b) tissue model. (c) Concentrations against the permeability at position $x' = 0.195$. (d) Concentration distribution for 10 nm size drug particles in the tissue domain.

centration input to the tissue domain) concentration difference in spanning P' from 0 to 100 cm/h, while in the case of $\mu_I = 10$ cP, it is reduced to roughly 0.05 M (5 % of 1 M), almost half. So, the concentration distribution for $\mu_I = 5$ cP is significantly different from $\mu_I = 10$ cP. It should be noted that the 5 % is also a significant amount, as in general, only small amount of drug does reach the diseased sites. Thus, in conclusion, permeability has significant effects on penetration and distribution of drug. Numerical experiments are also obtained for 10 nm particles, the results are displayed in Fig. 4.11(d).

For each particle size, a range (say $R = [P_{\text{min}}, P_{\text{max}}]$) in permeability P' can be identified, outside which there is no significant difference on drug penetration and distribution on variation of P'. The permeability value P_{max} leads to the maximum transport, and hence, it can be taken as the optimal value. From Figs. 4.10(b) and 4.11(b), it can be seen that $R = [0.1, 100]$ for 1

nm particles, but $R = [0.01, 5]$ for 10 nm particles. Clearly, the range R varies across the drug particle size since the permeability depends on the transverse membrane diffusion (Eq. (4.8)), which subsequently depends on the solute particle size.

4.4.3 Effects of drug particle size

To determine the effects of particle size on penetration of a drug, the FVHMM-p is simulated with three different size particles, $r = 1$, 10, and 100 nm. In this experiment, permeability values are selected in two ways. First, experiment is conducted by fixing $P' = 1$ cm/h for each size of particles, and the results are displayed in Fig. 4.12(a). Second, as the transverse membrane permeability is inversely proportional to the solute particle size, different permeability values are considered for different size of particles, $P' = 1$ cm/h for 1 nm, $P' = 0.1$ cm/h for 10 nm, and $P' = 0.01$ cm/h for 100 nm size particles. From the results (Fig. 4.12(b)), it can be noticed that the drug penetration is significantly large for smaller size particles. The 100 nm drug particles show very less penetration (≈ 0.05 cm) in tissue; whereas, 1 nm particles penetrate almost up to 0.4 cm.

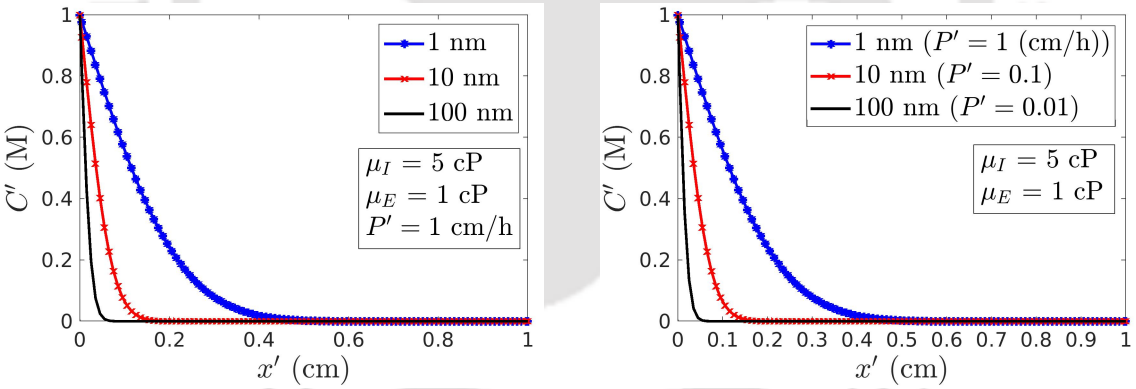

(a) (b)

Figure 4.12: Effects of particle size on penetration. (a) $P' = 1$ cm/h and (b) permeability (in cm/h) for respective particle is shown in the legend.

4.4.4 Effects of cell geometry

In this section, the effects of cell shape and its size on tissue penetration and distribution of a drug are investigated. Four different types of experiments are conducted. In the first-type, the shape of cell is chosen to be circular with varying radius. In the second-type, the experiments

are performed with elliptical shape by keeping width a_1 to be fixed (along the x'-axis) and varying the height a_2 (along the y'-axis). In the third-type, the experiments are conducted with elliptical shape by maintaining a fixed height (a_2) and varying the width (a_1). In the last one, keeping the cell area (hence, the extracellular volume) unchanged, the cell shape is chosen in three ways. Fig. 3.7(d) displays the schematic representation for the cell height and width.

In the first-type experiments, the cell is assumed to be circular. As the microscale domain size is fixed, the cell radius variation leads to the change in extracellular volume. The experiments are conducted with cell radii as, $2.1 \times 10^{-4}, 3.1 \times 10^{-4},$ and 4.1×10^{-4} cm for different permeability values. The results are displayed in Fig. 4.13. One can see that the drug penetration distances are significantly different for different choices of cell radius (Fig. 4.13(a)). Fig. 4.13(b) shows the drug concentrations at point $x' = 0.195$ against the cell radius. Drug concentration decreases with the increase in cell radius. This is because, the extracellular space, which is the main medium of drug transport into the tissue domain, decreases with the increase in cell radius, and consequently less amount of drug penetrates the tissue. From Fig. 4.13(b), one can also notice that with the increase in cell radius, the effect of permeability also increases. For $P' = 0.1$ cm/h, the concentration is reduced by ≈ 0.2 M when the cell radius increases from 2.1×10^{-4} to 4.1×10^{-4} cm, but for $P' = 10$ cm/h, the concentration difference is ≈ 0.1 M which is 10 % of 1 M. This is because an increase in cell radius increases the cell membrane surface area, and hence, the permeability becomes an important factor.

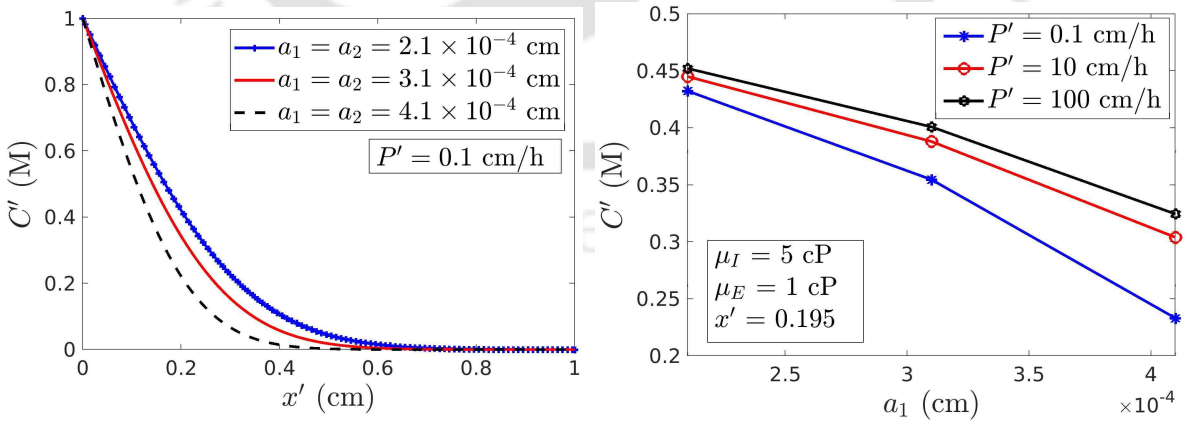

(a) (b)

Figure 4.13: Effects of cell size (or extracellular spatial volume) on drug penetration. (a) Results in tissue domain for $P' = 0.1$ cm/h and (b) the concentrations at point $x' = 0.195$ for different permeability values.

In the second-type experiments, the cell semi-minor axis length ($a_1 = 2.1 \times 10^{-4}$ cm) is kept fixed, and the experiments are conducted by changing the semi-major axis length (a_2), i.e., the height of the cell. The results are displayed in Fig. 4.14. There is a pronounced effect of cell height on penetration and distribution of drug in the tissue domain. The findings are quite similar as seen in the case of cell radius variation (Fig. 4.13).

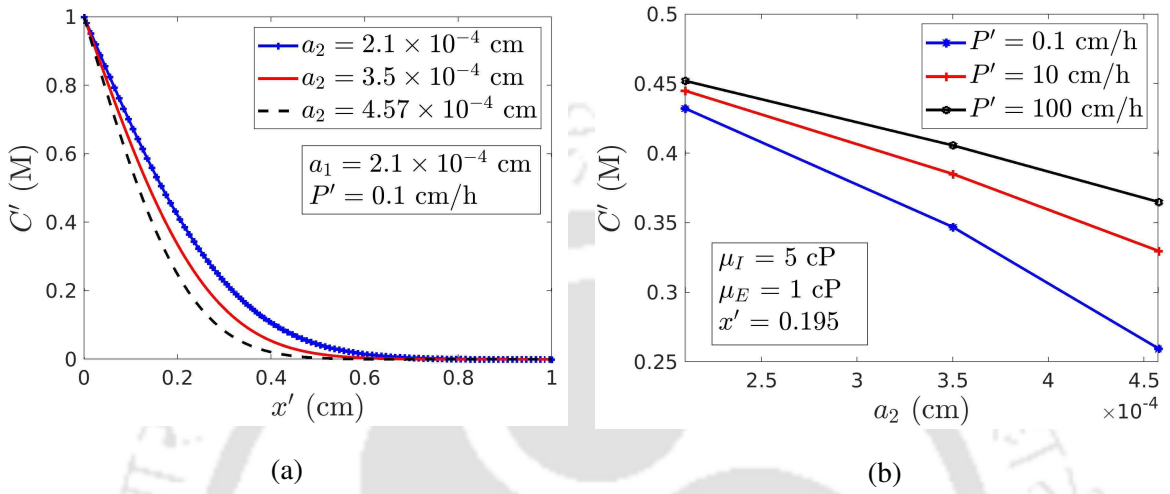

(a) (b)

Figure 4.14: Effects of cell height (a_2) on drug penetration. (a) Results in tissue domain for $P' = 0.1$ cm/h and (b) the concentrations at point $x' = 0.195$ for different permeability values (μ_I = 5 cP and μ_E = 1 cP).

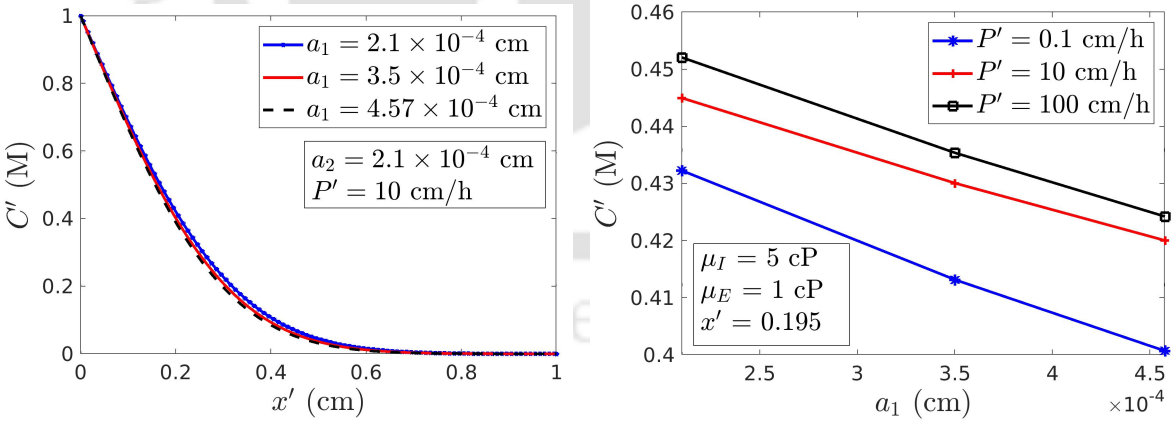

(a) (b)

Figure 4.15: Effects of cell width (a_1) on penetration. (a) Results in tissue domain for $P' = 0.1$ cm/h. (b) The concentrations at point $x' = 0.195$.

In the third-type experiments, the cell height ($a_2 = 2.1 \times 10^{-4}$ cm) is kept unchanged and varying the cell width (a_1). The results are displayed in Fig. 4.15. In Fig. 4.15(a), all

curves are almost overlapping, and hence, cell width has less effect on drug penetration. The concentrations at point $x' = 0.195$ against the cell width (a_1) (Fig. 4.15(b)) show that the curves are apart with a small concentration difference.

To determine the effects of cell shape, the extracellular as well as the intracellular volume is kept unchanged and the experiments are conducted by varying the shape of the cell. In the first two experiments, the cell is chosen to be elliptical with its different axis lengths, and circular in the last experiment. The parameters are chosen as, $a_1 = 4.57 \times 10^{-4}$ cm and $a_2 = 2.1 \times 10^{-4}$ cm in the first experiment and $a_1 = 2.1 \times 10^{-4}$ cm and $a_2 = 4.57 \times 10^{-4}$ cm in the second experiment, while in last one, $a_1 = a_2 = 3.1 \times 10^{-4}$ cm. Note that all three cells occupy the same area, and the cell shape changes with different choices of parameters. The results from numerical experiments are displayed in Fig. 4.16. Clearly, one can see that the cell shape affects drug penetration (Fig. 4.16(a)). In order to quantify the drug distribution, the concentrations at point $x' = 0.195$ are plotted in Fig. 4.16(b) for different permeability values. The concentrations are plotted against the cell height a_2. It can be seen that the drug concentration decreases with the increase in cell height, and the effects are large in the case of low permeable membranes.

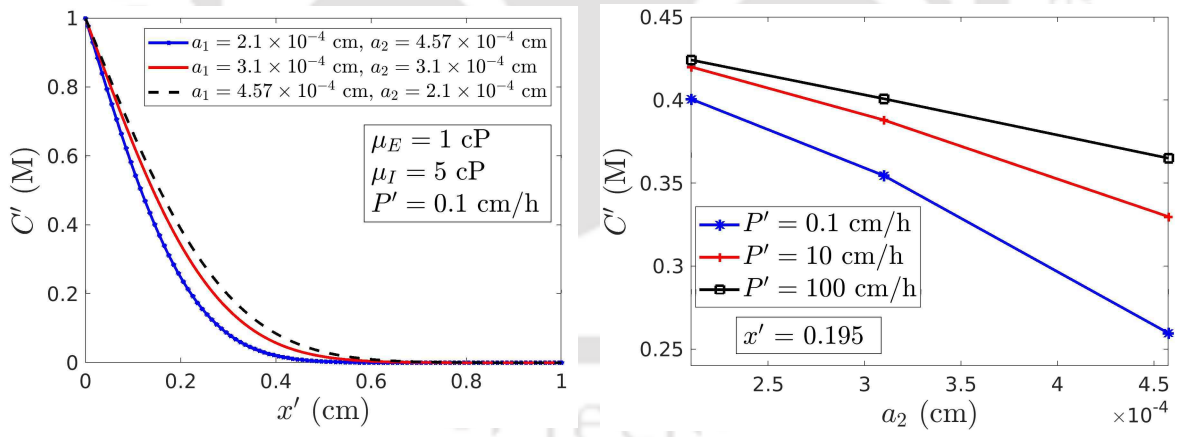

(a) (b)

Figure 4.16: Effects of cell geometry on penetration. (a) Results in tissue domain for $P' = 0.1$ cm/h. (b) The concentrations against a_2 at point $x' = 0.195$.

It can be concluded that the effect of cell width on drug penetration is less in contrast to the cell height. It is also observed that the height as well as the radius of the cell affects penetration and distribution of drug in the similar way.

4.5 Conclusions

This chapter proposes a finite volume heterogeneous multiscale method (FVHMM-p) to study drug delivery in tissues with passive diffusivity across the cell membrane. The inclusion of passive diffusivity (cell membrane permeability) in the model is the novelty of this study. The restrictive passive diffusion across the membrane, that incorporates solute transmembrane diffusivity, membrane thickness, and partition coefficient, is considered in the microscale model using permeable interface condition. For the microscale model simulation, a novel permeable interface method (PIM) based on the central-type finite difference discretization is proposed. The PIM is validated for 1D and 2D problems, and it is found to produce better results compared to the existing ones. PIM produces results of similar accuracy for different permeability values, and it is found to be of first-order accurate. It can also be used for permeable as well as for non-permeable membranes. The FVHMM-p results agree well with the experimental results while the FV-HMM is found to overestimate drug penetration. However, for $K = 0$, the FVHMM-p results are comparable with the ones of FV-HMM.

Furthermore, the effects of cell membrane permeability, drug particle size, intra- or extracellular volume, and the cell geometry on penetration and distribution of drug particles in tissues are studied. The following findings are observed from the simulated results.

1. Solute permeability of the cell membrane affects drug penetration and distribution.

2. The effects of permeability vary across the equal ($\mu_I = \mu_E$) and different fluid viscosity in the intra- and extra-cellular spaces (where $\mu_I > \mu_E$).

3. For each particle size, a range $R = [P_{\text{min}}, P_{\text{max}}]$ in permeability is identified, outside which there is no significant difference in the drug penetration and concentration distribution. Hence, P_{max} is an optimal value that leads to maximum transport. For 1 nm particles, $R = [0.1, 100]$ but for 10 nm particles, $R = [0.01, 5]$ is noticed.

4. Larger size particles penetrate in the deep at a significantly large distance compared to the smaller ones. The 100 nm drug particles show very slow and less penetration ($\approx$ 0.05 cm) in tissue; however, 1 nm particles penetrate in the deep at a significantly larger distance ($\approx$ 0.4 cm). The penetration depths are obtained by simulating FVHMM-p for 5 h.

5. The cell is considered to be elliptical, and the simulation with different configurations lead to the pronounced effects on drug penetration irrespective of the cell membrane permeability.

6. It is noticed that the cell's height and radius both affect the drug penetration; whereas, the cell width has a less effect on drug penetration.

7. It is also observed that the cell shape can affect the drug penetration and distribution irrespective of the tissue domain's porosity (extracellular spatial volume).

भारतीय प्रौद्योगिकी संस्थान गुवाहाटी
Indian Institute of Technology Guwahati

CHAPTER 5

EFFECTS OF CELL ORIENTATION ON DRUG DELIVERY

The previous choice of reconstruction operator (presented in Chapter 2) leads to the limited applicability of the FVHMM-p, which is a concern of the present chapter. In the literature, there is no study available which has shown the effects of reconstruction operator on macroscopic physics of the problem. In this chapter, two novel reconstruction operators are proposed for the application in drug delivery process.

Though some drugs get approval through the clinical trials for future use [6], but their efficacies may not be clearly understood due to the heterogeneity of tissue [55]. The cell geometry contributes to the tissue's structure. The shape of cell, which changes during growth, division and death of cell, determines the tissue morphogenesis [41]. The cell constantly controls the intracellular activities and remodels the extracellular matrix [7]. As a result, the biological cells can have different shapes, such as round, elongated, spherical, and spindle shape. The FVHMM-p considered elliptical cells with axes aligned along the coordinate directions. However, the spindle cell can have different orientations across the tissues (Fig. 5.1), which also may affect the drug delivery process. In tissue engineering, it is utmost important to control the interior structures while creating artificial tissues that closely mimic natural ones [14]. The knowledge of the effects of cell orientation on drug delivery can provide insights beforehand for experimental investigations of a drug. So, cell orientation could be a prominent factor in the drug delivery process. However, in the context of drug delivery, the authors have not come across any literature where the effects of cell orientation on drug delivery have been studied.

This chapter investigates the effects of cell orientation on drug transport in biological tissues. With the modified FVHMM-p, i.e., using new reconstruction operator, it is possible to

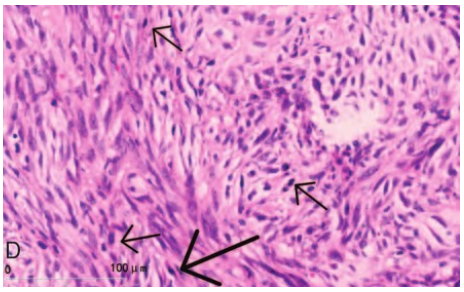

Figure 5.1: Tissue image [28].

study drug distribution in the tissue domain with the elliptical cells whose axes are no longer aligned with the coordinate axes. The simulation results reveal that the biological cell orientation is an important factor, which can affect drug penetration and distribution. Furthermore, the local sensitivity analysis is performed to determine the most sensitive parameter to the model response.

5.1 Model formulation

The model considered here is the one discussed in Chapter 4. The macroscale model is given by Eqs. (2.3)–(2.4), and its discretized version by (2.8). It is assumed that the drug is supplied through the left boundary and diffuses towards the right one. So, the boundary conditions are used as,

$$C(t, 0, y) = C_{in}, \tag{5.1}$$

$$C(t, L, y) = C_{out}, \tag{5.2}$$

respectively. Tissue domain is considered to be sufficiently large to ensure that $C_{out} = 0$ for the stipulated time. For drug delivery in tissues, physiological conditions suggest that the fluxes need to be specified at the lateral boundaries to exhibit a realistic situation of drug transport in the living organisms. The drug that moves through the lateral boundaries is modelled by the convection boundary condition, which is defined as,

$$-\mathbf{F} \cdot \mathbf{n}_t = \kappa(C - C_\infty), \tag{5.3}$$

where C_∞ denotes the drug concentration in the exterior of tissue, and it is taken to be zero in this work. κ denotes the mass transfer coefficient, and $\mathbf{n}_t$ is the normal vector to the tissue (boundary). In general, the flux $\mathbf{F}$ is defined to be proportional to the concentration gradient

(Fick's law), but here, no concrete form is assumed; instead, it is determined by using the microscopic information. Alternatively, the following relation is useful if the effective diffusivity (D_{eff}) is known at the boundary.

$$-D_{eff}\frac{\partial C}{\partial \mathbf{n}_t} = \kappa(C - C_\infty). \tag{5.4}$$

The schematic diagram of the tissue domain and boundary conditions are depicted in Fig. 5.2.

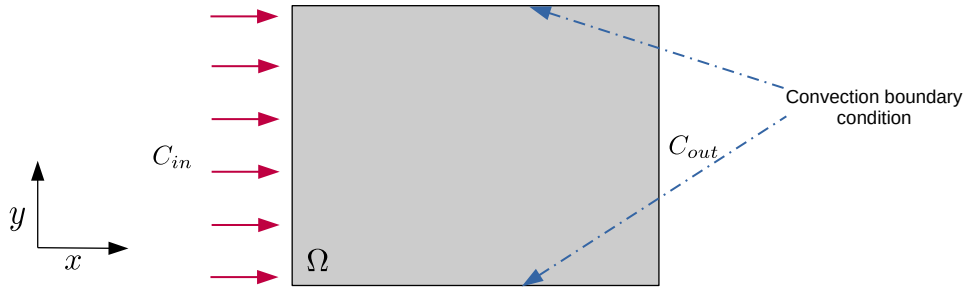

Figure 5.2: Schematic of problem.

In this chapter, mainly the effects of elliptical cell orientation on drug delivery process are discussed. The equation for the cell rotated by an angle ϕ in counter-clockwise direction can be written as,

$$\Gamma : \quad \frac{((x-x_0)\cos\phi + (y-y_0)\sin\phi)^2}{a_1^2} + \frac{((x-x_0)\sin\phi - (y-y_0)\cos\phi)^2}{a_2^2} = 1,$$

where (x_0, y_0) is the centre of the ellipse. a_1 and a_2 are chosen to be constants. $\phi = 0$ corresponds to an elliptical cell whose axes lie along the coordinate directions.

In order to estimate the macro flux $(\mathbf{F})$, the microscale models are constructed as discussed in Section 4.1.1. The reconstruction of boundary condition is discussed next.

5.1.1 Reconstruction operator

Note that, in the reconstruction operator used in Chapter 4, the x-directional macroscopic concentration gradient is imposed in the east and west microscale models to determine the x-directional fluxes, whereas y-directional macroscopic concentration gradient is used in the north and south microscale models in order to extract the y-directional fluxes.

New reconstruction operator

It is noticed that the old reconstruction operator does not impose the correct macroscopic concentration gradient on the microscale model, although it works fine for the study in previous

chapters. In the FVHMM-p, the axes of the elliptical cell placed in the microscale domain are taken to align along the coordinate directions; but if this is not the case, the old operator may not perform as expected. This is due to the fact that the microscale models placed at the north and south faces of the CV are constrained by the y-directional concentration gradient that remains zero throughout the FVHMM-p simulation (Section 4.4).

To use correct macroscopic concentration gradient at the microscopic level, two new reconstruction operators are proposed in the present study. In the following, the new operators are classified as type-I and type-II, any one of these can be used to apply the correct macroscopic concentration gradient on the microscale model. The general idea is to construct an operator in such a way that it can impose the x-directional as well as the y-directional concentration gradient simultaneously on each microscale model.

Type-I

Suppose, the CV (k, l) is interior one. For ω^{e_f} (as in Fig. 5.3), the boundary values (c) on the left $\left(\partial\omega_1^{e_f}\right)$ and right $\left(\partial\omega_2^{e_f}\right)$ boundaries are obtained by using the old reconstruction operator. At the upper $\left(\partial\omega_4^{e_f}\right)$ and lower $\left(\partial\omega_3^{e_f}\right)$ boundaries, the y-directional macroscopic concentration gradient is imposed using the macroscopic concentrations at the nodes **A** and **B** (shown in Fig. 5.3). The macroscopic concentration at node **A** $(C^n_{\mathbf{A}})$ is determined by taking the arithmetic average of concentrations of the CVs surround the node as,

$$C^n_{\mathbf{A}} = \frac{C^n_{k,l} + C^n_{k+1,l} + C^n_{k,l+1} + C^n_{k+1,l+1}}{4}.$$

Similarly, the concentration at node **B** $(C^n_{\mathbf{B}})$ is obtained as,

$$C^n_{\mathbf{B}} = \frac{C^n_{k,l} + C^n_{k+1,l} + C^n_{k,l-1} + C^n_{k+1,l-1}}{4}.$$

The concentrations on the upper and lower boundaries of the microscale model are evaluated as,

$$c_{i,j} = C^n_{\mathbf{B}} + \xi_j \frac{C^n_{\mathbf{A}} - C^n_{\mathbf{B}}}{h} \quad \text{for } i = 2, 3, \ldots, M-1, \text{ and } j = 1 \text{ and } M,$$

where $\xi_1 = \epsilon^-$ and $\xi_M = \epsilon^+$ (the lower and upper boundaries, respectively).

The boundary condition for the microscale model ω^{n_f} is obtained as follows. The boundary values on the upper and lower boundaries are determined using the old reconstruction operator. For the left and right boundaries, the concentration at node **A** is already determined and the concentration $(C^n_{\mathbf{B}'})$ at node **B**′ (see Fig. 5.3) is calculated as,

$$C^n_{\mathbf{B}'} = \frac{C^n_{k,l} + C^n_{k-1,l} + C^n_{k,l+1} + C^n_{k-1,l+1}}{4}.$$

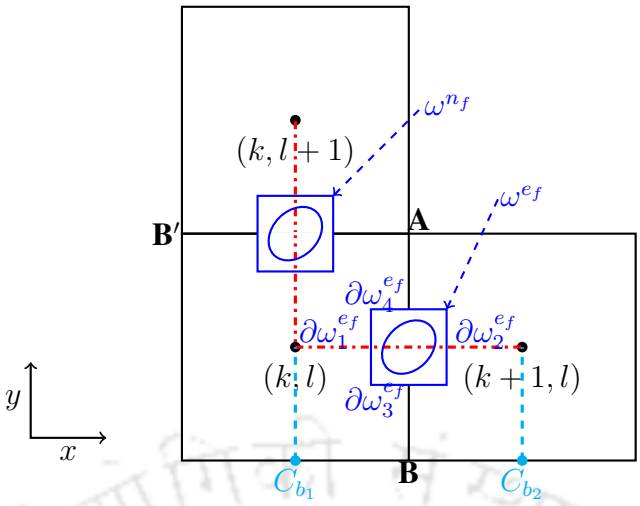

Figure 5.3: Schematic for the implementation of novel reconstruction operators.

The reconstruction is used as

$$c_{i,j} = C^n_{\mathbf{B}'} + \xi_i \frac{C^n_{\mathbf{A}} - C^n_{\mathbf{B}'}}{h} \quad \text{for } j = 1, 2, \ldots, M, \text{ and } i = 1 \text{ and } M,$$

for $\xi_1 = \epsilon^-$ and $\xi_M = \epsilon^+$ (left and right boundaries, respectively).

Consider the CV (k, l) (in Fig. 5.3) is adjacent to the boundary of the macroscale domain and its lower face coincides with the macroscopic boundary. If the concentration (Dirichlet condition) is prescribed at the boundary node **B**, it can be used for reconstruction directly. In the case of convection boundary condition, the concentration is determined at node **B** (discussed in the later part of this section) and then it is used for reconstruction.

Type-II

In the type-II reconstruction, bilinear interpolation is used. Consider the CV (k, l) is an interior one. Firstly, the reconstruction operator is discussed for the microscale model constructed on the east face (ω^{e_f}) (see Fig. 5.3). Two interpolating functions are determined using the bilinear interpolation; $f_1(x, y)$ using the macroscopic concentrations $C_{k,l}$, $C_{k+1,l}$, $C_{k,l+1}$, and $C_{k+1,l+1}$, and $f_2(x, y)$ using $C_{k,l}$, $C_{k+1,l}$, $C_{k,l-1}$, and $C_{k-1,l-1}$. $f_1(x, y)$ is used to evaluate the microscopic concentration values $(c_{i,j})$ that lie above the dash-dotted line joining (x_k, y_l) to (x_{k+1}, y_l) (in Fig. 5.3), while $f_2(x, y)$ is used to compute $c_{i,j}$'s that are below to the line.

The bilinear interpolating function $f(x, y)$ for any four points (x_1, y_1), (x_2, y_1), (x_1, y_2), and (x_2, y_2) and their respective functional values f_{11}, f_{21}, f_{12}, and f_{22}, can be written as,

$$f(x, y) = \frac{(y_2 - y)\left[(x_2 - x)f_{11} + (x - x_1)f_{21}\right] + (y - y_1)\left[(x_2 - x)f_{12} + (x - x_1)f_{22}\right]}{(x_2 - x_1)(y_2 - y_1)}.$$

So, the boundary values for the microscale model are calculated as,

$$c_{i,j} = f(x_i, y_j),$$

where f is either f_1 or f_2.

For the microscale model (ω^{n_f}), $f_1(x, y)$ is determined using $C_{k,l}$, $C_{k+1,l}$, $C_{k,l+1}$, and $C_{k+1,l+1}$, and the second function, (say it) $f_3(x, y)$ using $C_{k-1,l}$, $C_{k,l}$, $C_{k,l+1}$, and $C_{k-1,l+1}$ concentration values. $f_1(x, y)$ is used to evaluate the $c_{i,j}$'s that lie right to the dash-dotted line joining points (x_k, y_l) and (x_k, y_{l+1}) while $f_3(x, y)$ is used for other side.

For boundary CV, if its face lies in the interior, similar procedure is adopted. However, as on the boundary there is no macroscopic grid point, two points , b_1 and b_2 (see Fig. 5.3), are introduced on the boundary, where the concentrations are C_{b_1} and C_{b_2}, respectively. These macroscopic concentrations are either given by Dirichlet boundary condition or in the case of convection boundary condition, a discussion is presented in the next.

Now on, for convenience, FVHMM-p is written as FVHMM-p(I) for type-I reconstruction operator and FVHMM-p(II) for type-2, while FVHMM-p is used for the multiscale method with old reconstruction operator developed in Chapter 2.

Implementation of convection boundary condition

The convection boundary condition given by expression (5.3) or (5.4) can be incorporated in the finite volume discretization. The discretization for the CV (k, l), whose south face is on the boundary of Ω (Fig. 5.3), can be written as,

$$\frac{C_{k,l}^{n+1} - C_{k,l}^{n}}{\Delta t} \approx \frac{1}{h^2}\left[F_{e_f}^{n} + F_{n_f}^{n} - F_{w_f}^{n} - \kappa(C_{b_1} - C_\infty)\right]. \tag{5.5}$$

In this equation, C_{b_1} needs to be determined. For boundary condition given by (5.3), C_{b_1} is obtained from the extrapolation of two consecutive interior grid points as,

$$C_{b_1} = C_{k,l} + (y - y_l)\frac{C_{k,l+1} - C_{k,l}}{h}. \tag{5.6}$$

For the case, where convection boundary condition given by (5.4), the concentration at boundary node is determined as,

$$C_{b_1} = \frac{C_{k,l} - k_m C_\infty h/2}{1 + k_m h/2},$$

where $k_m = \frac{\kappa}{D_{eff}}$.

In type-I reconstruction, the concentration at node **B** (Fig. 5.3) is calculated as,

$$C_{\mathbf{B}} = \frac{C_{\mathbf{A}}}{1 + k_m h}.$$

5.1.2 Estimation of macro flux

The microscale models are simulated using the permeable interface method (PIM), where the resulting set of equations are solved using BICGSTAB II with SSOR preconditioning for tolerance value 10^{-15}. Then, the macro flux is estimated as for the FVHMM-p. For boundary face, if the Dirichlet boundary condition is specified, the approach suggested in Chapter 2 is adopted, while if the flux condition is specified, the implementation is similar as for the convection boundary condition (Section 5.1.1).

5.2 Results and discussion

In this section, numerical convergence of the proposed multiscale method is demonstrated with an example whose analytical solution is available. The results are compared with the ones of the FV-HMM. Also, the results obtained from FVHMM-p(II) are compared with the ones from FVHMM-p followed by a grid independency test, and a validation is also performed with the experimental results. Finally, the effects of cell orientation on drug penetration and distribution are studied in the tissue domain.

5.2.1 Numerical convergence and comparison with the FV-HMM

To examine the convergence of the FVHMM-p(I) and FVHMM-p(II), Problem 3 is considered with the cell-free microscale domain.

Table 5.1 displays the maximum error estimates on macro-spatial grid refinement. It shows that the mesh refinement reduces the errors. On comparison, it can be observed that the results obtained from the FVHMM-p(II) are of similar accuracy as that of the FV-HMM, however, more accurate than that from FVHMM-p(I). The better accuracy of the FVHMM-p(II) than of the FVHMM-p(I) is due to the fact that, for type-I, fixed values are used as the boundary condition at each side of the microscale boundaries, whereas in the old operator as well as in the type-2 operator, concentration gradient (linearly varying concentrations) is imposed on the boundary. From this discussion, it can be concluded that the reconstruction operator can affect the overall accuracy of the results. In Fig. 5.4, surface plots for the numerical and analytical solutions on the finite volume mesh of size 20×20 are displayed. It shows that the numerical solution is in very good agreement with the analytical one.

As the type-II is more accurate than the type-I, it is used in rest of the calculations unless stated explicitly.

Table 5.1: Maximum error estimates ($||E_h||_\infty$) for the FVHMM-p with the type I and type II reconstruction operators and for the FV-HMM.

Mesh size (macro)	FVHMM-p(I)	FVHMM-p(II)	FV-HMM
	$\|\|E_h\|\|_\infty$	$\|\|E_h\|\|_\infty$	$\|\|E_h\|\|_\infty$
10×10	1.349×10^{-9}	4.059×10^{-10}	3.993×10^{-10}
20×20	1.037×10^{-9}	5.974×10^{-11}	5.666×10^{-11}
30×30	9.982×10^{-10}	1.829×10^{-12}	3.831×10^{-12}

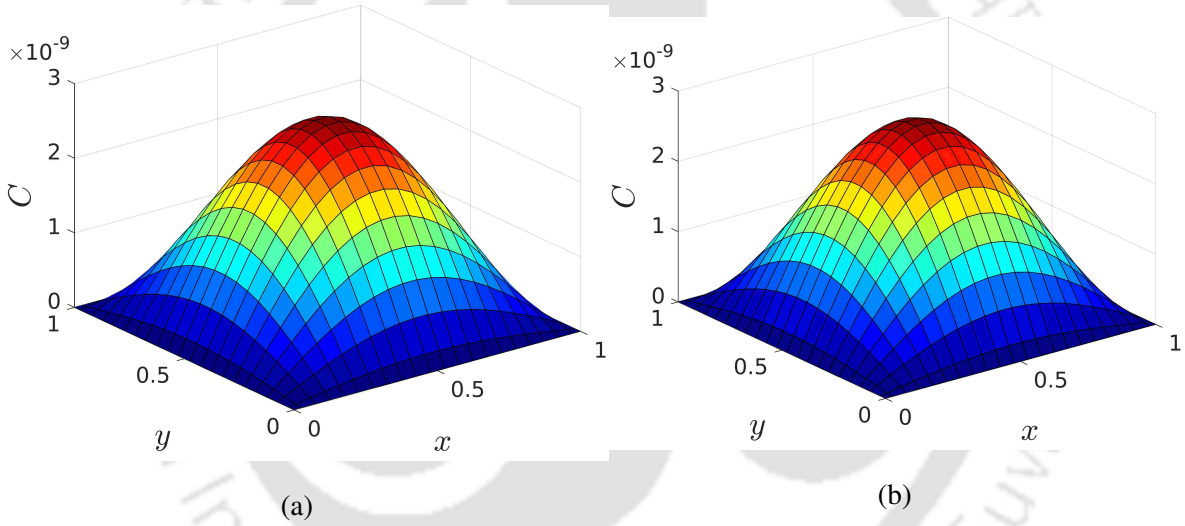

Figure 5.4: A comparison between the (a) analytical and (b) numerical (FVHMM-p(II)) solutions on the finite volume mesh of size 20×20 at $t = 1$.

5.2.2 Grid independency

Prior to simulate the model, grid independency of the results is ensured. The boundary conditions for the macroscale model are chosen as; $C'_{in} = 1$ M (M = molar) (left boundary), $C'_{out} = 0$ M (right boundary), zero flux condition on the upper and lower boundaries, i.e., $\frac{\partial C'}{\partial y'} = 0$ M/cm, and the initial condition $C'_0 = 0$ M in the whole domain. Parameters for the model are chosen as: $a_1 = 4.57$ μm, $a_2 = 2.1$ μm, $\mu_I = 5$ cP, $\mu_E = 1$ cP, $r = 1$ nm (nm – nanometer and r is the radius of the cell), and $P' = 0.1$ cm/h. Microscale domain is chosen to be a square domain of

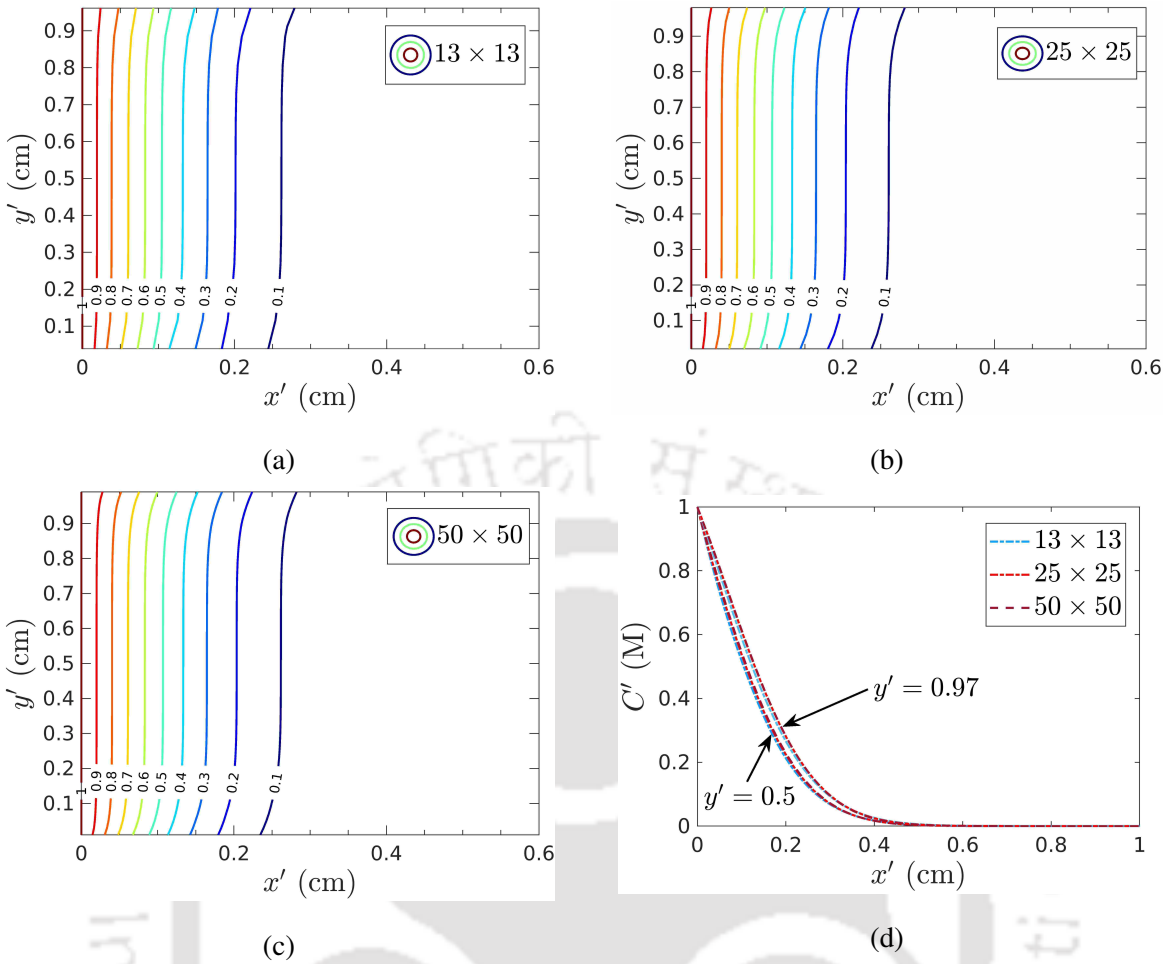

Figure 5.5: Grid independency results for the FVHMM-p(II) on macro-spatial grid (a) 13×13, (b) 25×25, and (c) 50×50. (d) Concentrations along the lines $y' = 0.5$ and $y' = 0.97$ from each of the contour.

edge length 10 μm, where the cell is taken to be placed at the centre with $\phi = \frac{\pi}{4}$. Numerical experiments are conducted in 1×1 cm^2 macroscale domain for $t' = 3$ h.

For grid independency test, the macroscale model is simulated for three macro-spatial grids: 13×13, 25×25, and 50×50 with $\Delta t' = 10^{-3}$ h, and the micro-spatial grid is chosen of size 100×100. Fig. 5.5 displays the contour plots of concentration distribution for each choice of macro-spatial grids. Also, the concentrations along the lines $y' = 0.5$ and $y' = 0.97$ are displayed in Fig. 5.5(d). It can be seen that the results for the macro-spatial grids 25×25 and 50×50 overlap. Thus, the grid size 25×25 is chosen as the working macro-spatial grid. It is also tested that further refinement in macro-temporal step size and micro-spatial step size does not affect the results obtained on 25×25 macro-spatial grid.

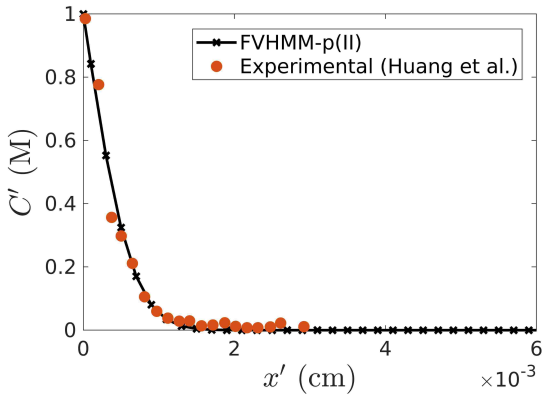

Figure 5.6: Comparison of the FVHMM-p(II) results with the experimental values of Huang et al. [23].

5.2.3 Validation with the experimental results

Experimental results of Huang et al. [23] are used to validate the results of the FVHMM-p(II). They investigated drug penetration in an *in vitro* setup, which was a spheroid-on-chip system. Numerical experiment is conducted with the parameters $D'_E = 1.8\times10^{-7}$ cm^2/h, $D'_I = 10^{-8}$ cm^2/h, and $P' = 0.1$ cm/h in the macroscale domain $[0, 0.01] \times [0, 0.01]$ for $t' = 2$ h. Results are displayed in Fig. 5.6. One can clearly observe that the results are in very good agreement.

5.2.4 Convection boundary condition

The correctness of implementation of the convection boundary condition in the multiscale algorithm is assessed by comparing the results with the ones obtained from package 'pdetool box' in the MATLAB [37]. The microscale model is considered to be cell-free. The model parameters are chosen to be the same as stated in Section 5.2.2. However, at the upper and lower boundaries, the convection boundary condition is specified with $\kappa' = 8.174217762 \times 10^{-2}$ cm/h and $D'_E = 8.174217762 \times 10^{-3}$ cm^2/h, and D'_{eff} is chosen to be the same as D'_E since the tissue is cell-free. Fig. 5.7 shows the results obtained from MATLAB and also from the FVHMM-p(II) with two choices of convection boundary conditions given by (5.3) and (5.4). One can see that all three sets of contour are exactly similar.

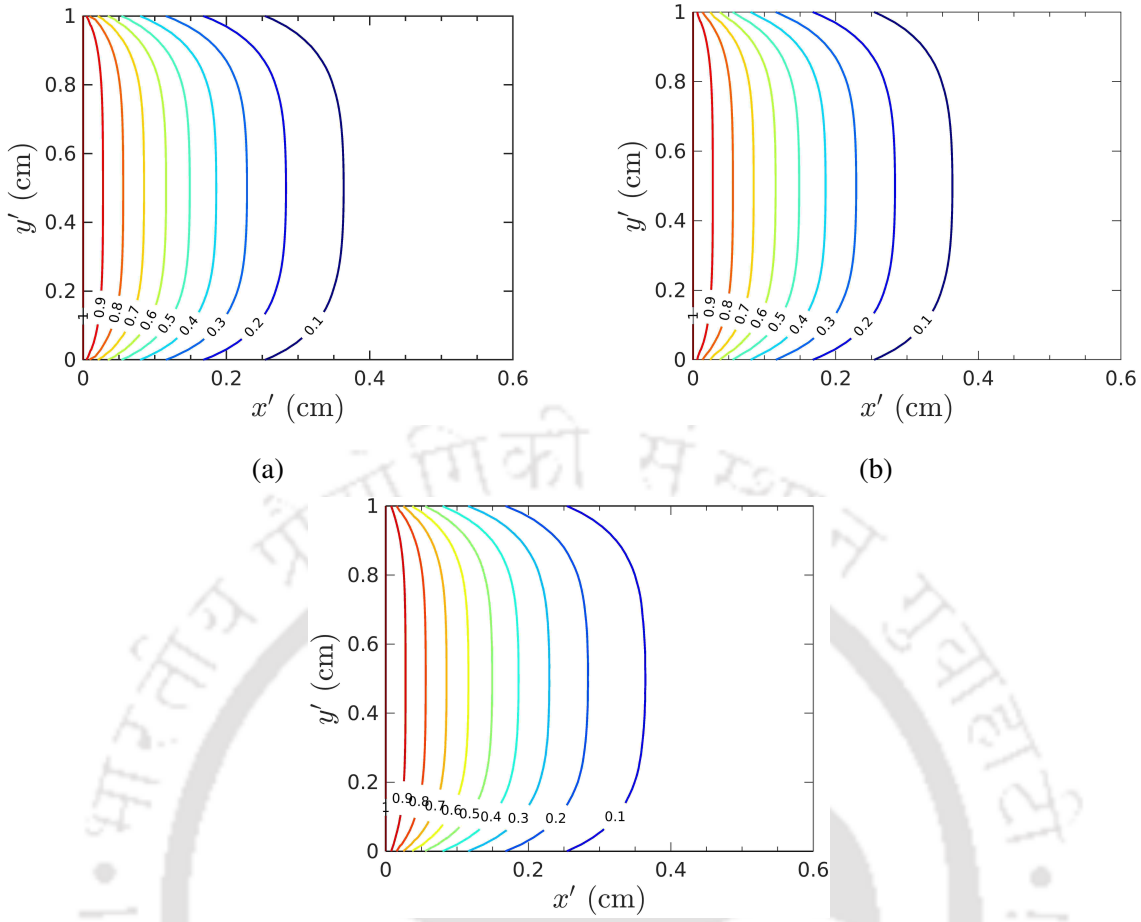

(a) (b)

(c)

Figure 5.7: Contour plots for concentration distribution on application of convection boundary condition on upper and lower boundaries, (a) FVHMM-p(II) along with Eq. (5.4), (b) FVHMM-p(II) along with Eq. (5.3), and (c) MATLAB solution.

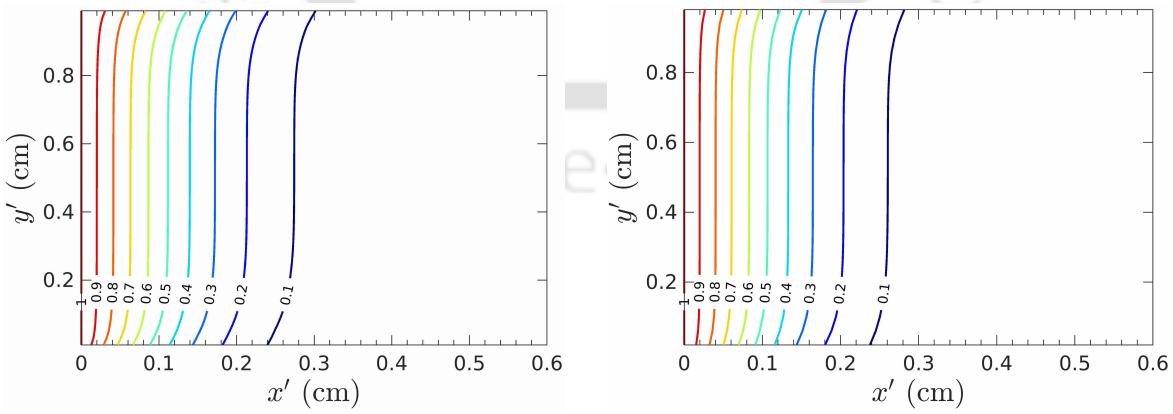

(a) (b)

Figure 5.8: Results for drug transport in tissue using (a) FVHMM-p(I) and (b) FVHMM-p(II) for $\phi = \frac{\pi}{4}$.

5.2.5 Type-I versus type-II operators

In this section, the results are compared to assess the abilities of type-I and type-II operators to capture the effects of cell orientation on drug delivery process. Numerical experiments are conducted with the model parameters as stated in Section 5.2.2. Fig. 5.8 shows the contour plots of concentration distribution for each of the methods FVHMM-p(I) and FVHMM-p(II) with $\phi = \frac{\pi}{4}$. Similar results are obtained from both the operators, and it can be seen that the resulted multiscale model can capture the effects that appeared on the boundary due to a specific orientation of the cells.

5.2.6 Old versus new reconstruction operators

In this section, it is discussed that how does the projection of concentration gradient on the microscale model, due to the new reconstruction operator (FVHMM-p(II)), lead to the physically realistic effective concentration distribution in tissues? The experiments are conducted with the model parameters as mentioned in Section 5.2.2. Experiments are performed for two situations; first, with the elliptical cell having axes along the coordinate directions, and second, with the cell rotated by an angle $\phi = \frac{\pi}{4}$ in the anti-clockwise direction.

Fig. 5.9 shows the concentration variation along the x'-direction. For $\phi = 0$, the concentration distribution is uniform along y'-direction for both FVHMM-p and FVHMM-p(II), and the results are shown in Fig. 5.9(a). It can be seen that the results are similar for both the methods. Hence, the choice of reconstruction operator does not make any difference in perspective of macroscopic physics when the elliptical cells are aligned along the coordinate axes.

For $\phi = \frac{\pi}{4}$, results are shown in Fig. 5.9(b). The concentration is uniform along the y'-direction for the FVHMM-p; however, for the FVHMM-p(II), the concentration gradient along y'-direction is non-zero near the upper and lower boundaries (one can see contour plot in Fig. 5.8(b)). So, in the Fig. 5.9(b), concentration distributions along the lines: $y' = 0.02$, $y' = 0.5$, and $y' = 0.98$ are shown. The results along the line $y' = 0.5$ agrees well for both the methods. However, drug penetration is larger near the upper boundary ($y' = 0.98$) whereas lesser in the vicinity of lower boundary ($y' = 0.02$) in the case of the FVHMM-p(II).

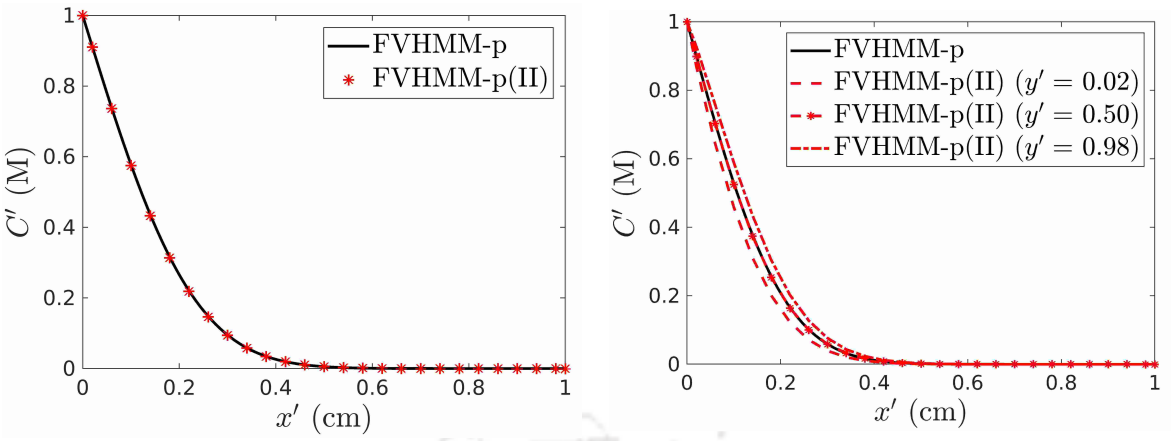

(a) $\phi = 0$. (b) $\phi = \frac{\pi}{4}$.

Figure 5.9: Prediction of concentration distribution and penetration using the FVHMM-p and FVHMM-p(II) for (a) the elliptical cell whose axes lie along with the coordinate directions ($\phi = 0$) and (b) the elliptical cell is rotated by an angle $\phi = \frac{\pi}{4}$ anticlockwise.

5.2.7 Effects of cell orientation on drug penetration and distribution

In treating chronicle diseases, it is well known that either the drug does not reach the diseased site or its efficacy may not be well understood. Biological cells hinder the drug penetration and ultimately determine the drug distribution in tissues. So, the understanding of drug penetration and distribution in the presence of cells is paramount. In reality, cells may not be aligned in some fixed direction. So, it is imperative to study the effects of cell orientation on drug transport. This may help optimize the drug efficacy and predict the drug penetration and distribution in the tissue domains.

In the following, effects of cell orientation on drug distribution are investigated with the choice of $\phi \in \left[0, \frac{\pi}{2}\right]$, which is chosen as $\frac{i\pi}{16}$ for $i = 0, 1, \ldots, 8$. The other model parameters are taken to be the same as in Section 5.2.2. The model is simulated for various values of κ'; here, results are discussed for $\kappa' = 0.01$ and 0.1 cm/h.

For $\kappa' = 0.01$ cm/h, the contour plots are displayed in Figs. 5.10(a)–(e) for different values of ϕ. Drug loss (or movement) can be seen across the upper and lower boundaries. This fact of drug loss is an eventual effect of convection boundary condition. Also, from the figures, it can be readily seen that the overall drug penetration decreases with the increase in ϕ. Note that $a_1 > a_2$ for $\phi = 0$. Thus, on cell rotation, i.e. for $\phi > 0$, (shown in Fig. 5.10(f)), the cell height increases that leads to decrease the penetration. It can be noticed that the overall extracellular volume is unchanged for any ϕ, but the drug penetration is affected. Also note

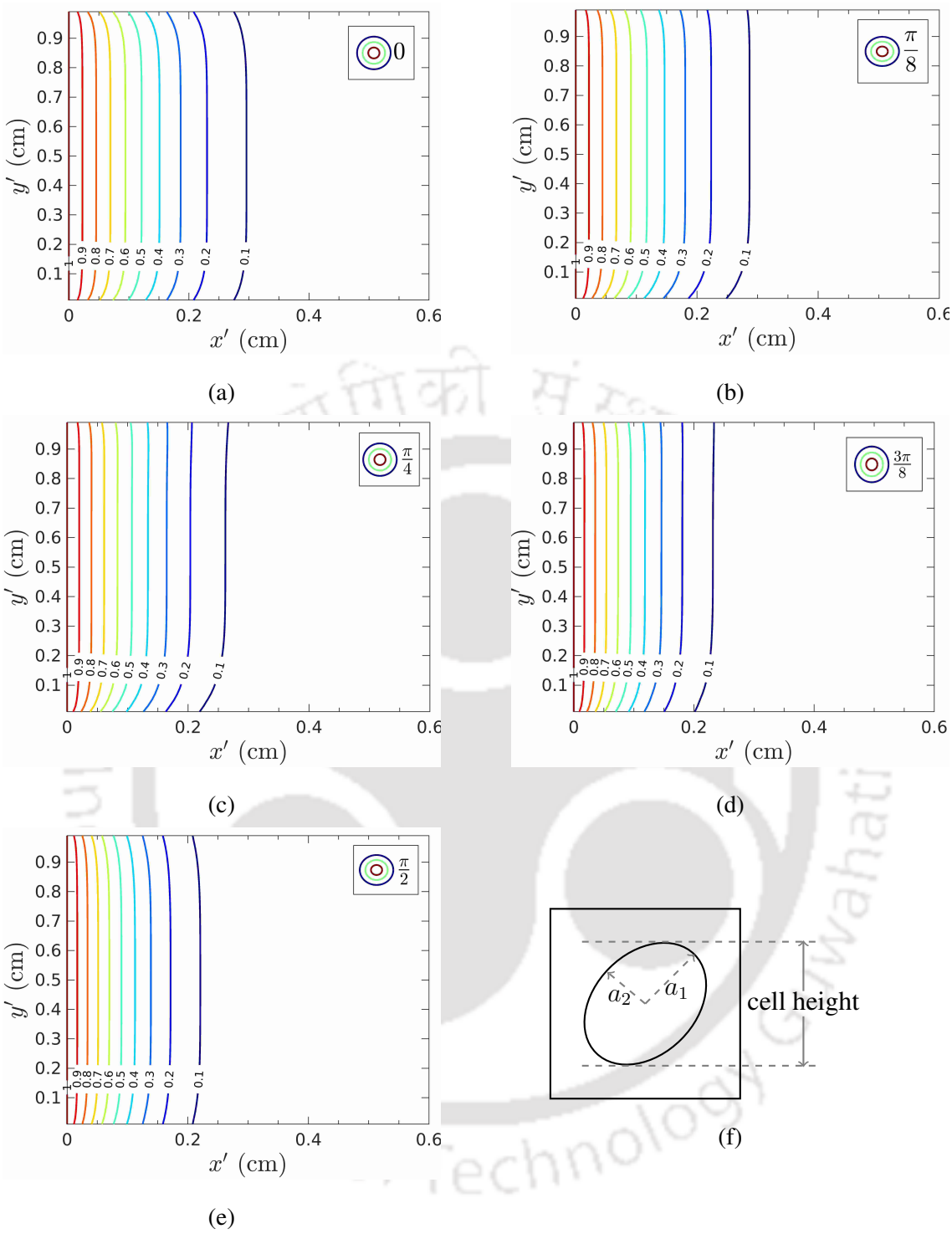

Figure 5.10: (a)–(e) Results for drug concentration distribution and penetration for various ϕ ($\kappa' = 0.01$). (f) Schematic of the cell height.

that drug achieves maximum penetration for $\phi = 0$ and minimum for $\phi = \frac{\pi}{2}$, which is true for the case where semi-major axis of the elliptical cell (with $\phi = 0$) lies in the x'-direction. Thus, the cell orientation could be pivotal in drug delivery.

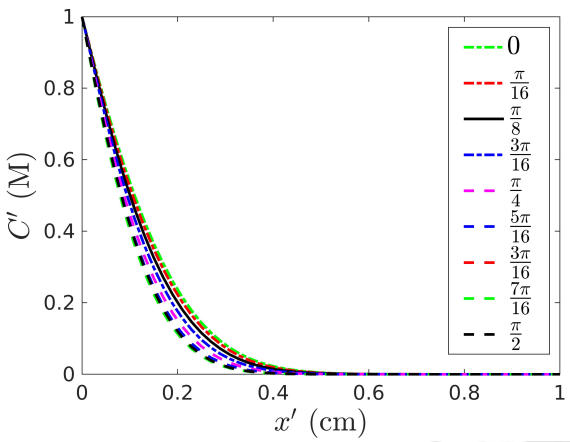

(a) Line: $y' = 0.05$.

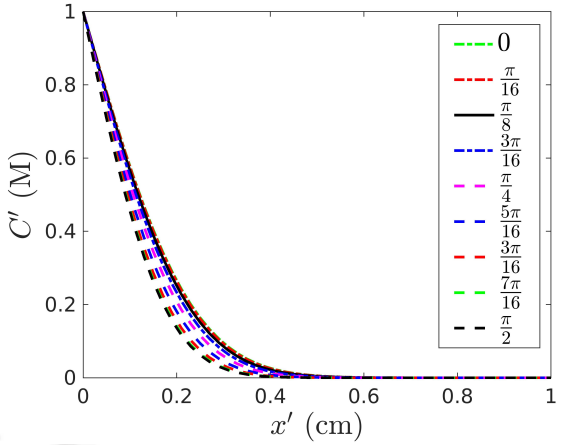

(b) Line: $y' = 0.49$.

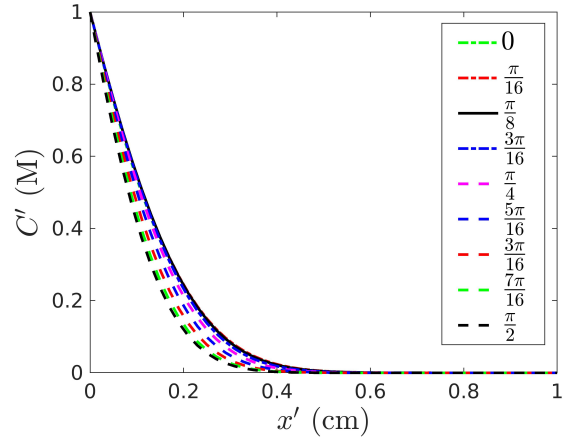

(c) Line: $y' = 0.95$.

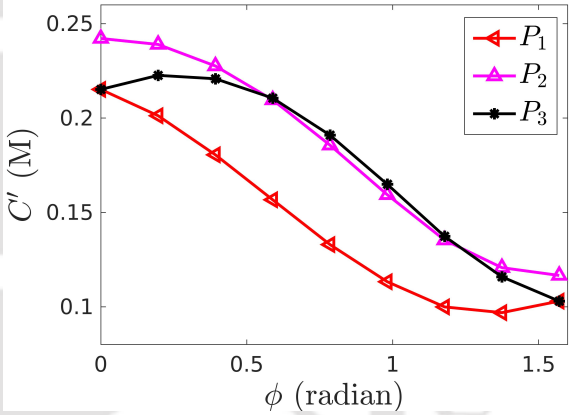

(d)

Figure 5.11: Drug concentrations along the lines (a) $y' = 0.05$, (b) $y' = 0.49$, (c) $y' = 0.95$, and (d) on the selected probes.

In order to further quantify the effects of cell orientation on drug penetration and distribution, results are analysed along some cross-sections of the tissue domain (Ω), and also $P_1 = (0.21, 0.05), P_2 = (0.21, 0.49)$, and $P_3 = (0.21, 0.95)$ are selected as the probes for investigation. Figs. 5.11(a)–(c) display the concentration distribution along the lines, $y' = 0.05$, $y' = 0.49$, and $y' = 0.95$, respectively, and the concentrations on the probes are shown in Fig. 5.11(d). Along the line $y' = 0.49$, drug penetration decreases monotonically with the increase in ϕ, and the difference in concentration on the probe P_2 is ≈ 0.1 M when ϕ changes from 0 to $\frac{\pi}{2}$. The difference in concentration is calculated as, $C_{max} - C_{min}$ for $0 \leq \phi \leq \frac{\pi}{2}$, where C_{max} and C_{min} are the maximum and minimum concentrations, respectively.

In the proximity of upper $(y' = 0.95)$ and lower $(y' = 0.05)$ boundaries, different patterns are observed. It is noticed that the drug concentration may not decrease monotonically with the

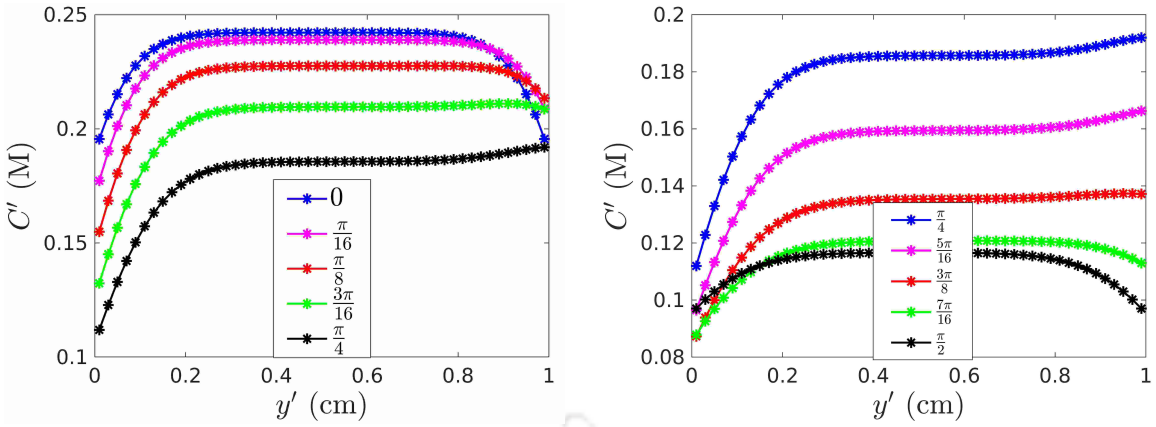

(a) (b)

Figure 5.12: Concentration distribution along the cross-section $x' = 0.21$. (a) $0 \leq \phi \leq \frac{\pi}{4}$ and (b) $\frac{\pi}{4} \leq \phi \leq \frac{\pi}{2}$.

increase in ϕ. For $y' = 0.95$, in the first half $\left(0 \leq \phi \leq \frac{\pi}{4}\right)$, the concentration forms a concave down curve (probe P_3, see Fig. 5.11(d)), whereas drug concentration decreases monotonically as ϕ increases for $\frac{\pi}{4} \leq \phi \leq \frac{\pi}{2}$. It could be the simultaneous effect of two parameters; cell height and the orientation of cell (ϕ). The rotation of ellipse causes to increase the drug accumulation near the upper boundary (see Fig. 5.9(b), the case of impermeable lateral boundaries), while an increase in ϕ increases the cell height in the path of drug diffusion. So, there are two factors that affect drug penetration oppositely. Next, the drug concentration in the proximity of lower boundary along the line $y' = 0.05$ is displayed in Fig. 5.11(a). The concentration decreases monotonically for the first half of ϕ $(0 \leq \phi \leq \frac{\pi}{4})$, while there is a concave up type curve for the concentration distribution in the second half $(\frac{\pi}{4} \leq \phi \leq \frac{\pi}{2})$ (probe P_1, see Fig. 5.11(d)). In all the experiments listed here, the drug concentration difference is approximately 10 % (of initial input concentration, $C'_{in} = 1$ M) on the probes for the selected range of ϕ. However, the concentration difference may vary across the tissue domain, but it is found to be a minimum of nearly 8 % in most of the tissue domain, which is a significant one.

Results are also analysed along the cross-section $(x' = 0.21)$ in the y'-direction. For discussion, the values of ϕ are taken again in two ranges $0 \leq \phi \leq \frac{\pi}{4}$ and $\frac{\pi}{4} \leq \phi \leq \frac{\pi}{2}$. Fig. 5.12 shows the concentration distribution along the line $x' = 0.21$ for both the ranges of ϕ separately. It is seen that the drug concentration is largely affected near the lower boundary (where concentration difference is $\approx$ 7–10 %) as compared to the upper one ($\approx$ 2 %) for the first range of ϕ, $0 \leq \phi \leq \frac{\pi}{4}$ (Fig. 5.12(a)), and for the latter range $(\frac{\pi}{4} \leq \phi \leq \frac{\pi}{2})$, drug concentration is

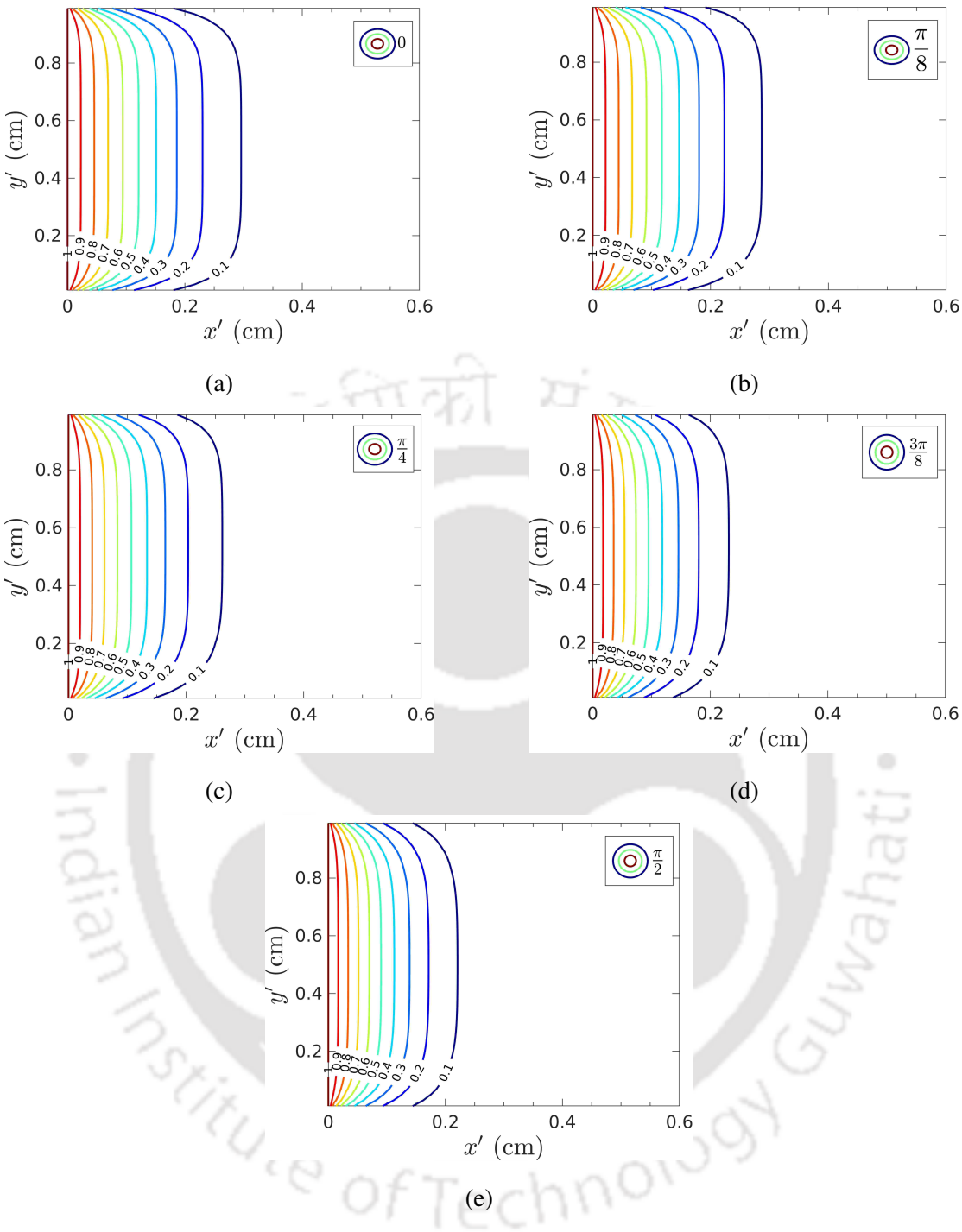

Figure 5.13: Drug concentration distribution and penetration with $\kappa' = 0.1$ cm/h for various values of ϕ.

largely affected at the upper boundary while the effect is less near the lower boundary. One can also see that for $\phi \approx \frac{\pi}{4}$, drug concentration is more at the upper boundary than that at the lower one (≈ 8 % concentration difference for $x' = 0.21$, see Fig. 5.12) but almost equal as ϕ approaches to either $\frac{\pi}{2}$ or 0. From this discussion, it can be concluded that $\phi = \frac{\pi}{4}$ is a critical

value, as above and below of this value different patterns are noticed.

The results for $\kappa' = 0.1$ cm/h are also investigated. The first observation is that the drug loss through the tissue's lateral boundaries is more in this case than that for $\kappa' = 0.01$ cm/h (see Fig. 5.13). Figs. 5.14(a) and (b) display the drug concentration distributions along the cross-section in y'-direction, and Fig. 5.14(c) displays concentrations on the selected probes. All qualitative observations for $\kappa' = 0.01$ cm/h also hold true for $\kappa' = 0.1$ cm/h, however their quantitative significance are much lesser.

From the discussion, one can conclude that the cell orientation affects drug transport significantly. The application of the convection boundary condition on the lateral boundaries leads to different drug distribution patterns in the proximity of the boundary. Hence, the orientation of the cell will be an important parameter for drug delivery applications in the tissues.

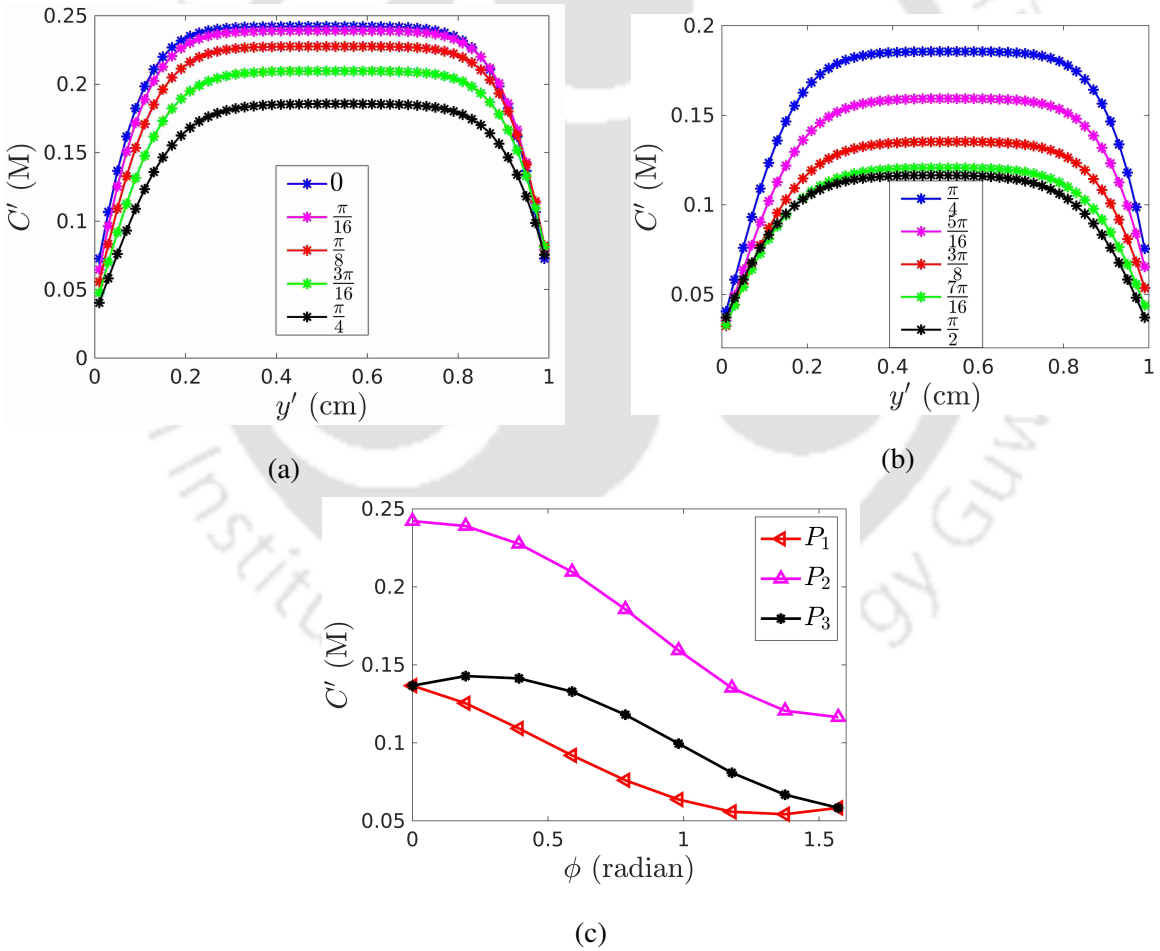

Figure 5.14: Drug concentrations along the cross-section $x' = 0.21$ for (a) $0 \leq \phi \leq \frac{\pi}{4}$ and (b) $\frac{\pi}{4} \leq \phi \leq \frac{\pi}{2}$. (c) Drug concentrations against ϕ on the probes.

5.2.8 Effects of cell dimensions and cell permeability

Effects of cell dimensions

The dimensions (more precisely, the parameters a_1 and a_2) of a cell are important and could be a deciding factor in drug delivery, as examined in Chapters 3 and 4. In order to understand the effects on cell orientation, the values of a_1 and a_2 are chosen in such a way that the area occupied by the cell remains same ($a_1 = 4.57$ μm and $a_2 = 2.1$ μm; call it cell E_1) as used in the above analysis. For another cell (call it cell E_2), $a_1 = 3.84$ μm and $a_2 = 2.5$ μm are chosen. In order to compare the results for the cells E_1 and E_2, numerical experiments are conducted keeping values of the other model parameters as stated in Section 5.2.2 except κ'. Here, $\kappa' = 0.1$ cm/h is considered.

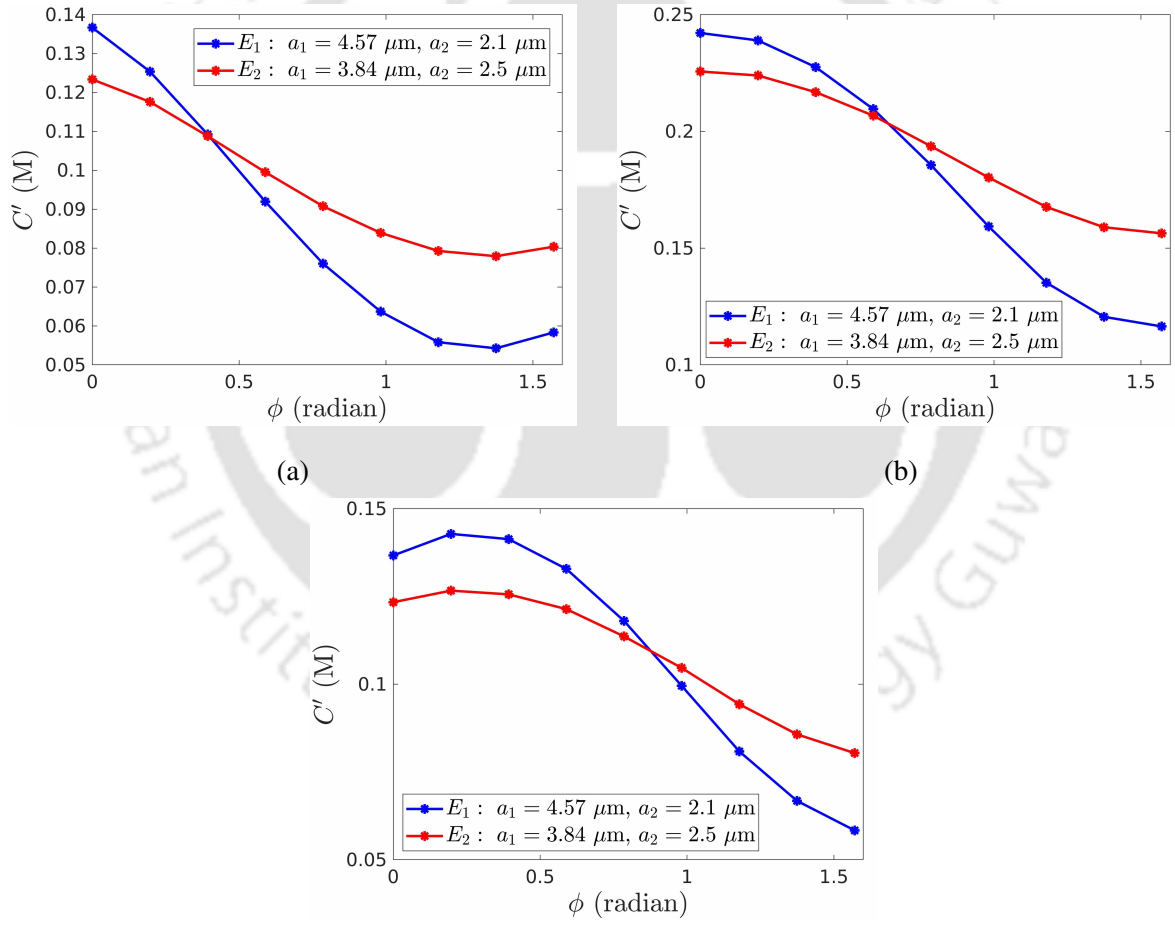

Figure 5.15: Drug concentrations for two different elliptical cells on probes (a) P_1, (b) P_2, and (c) P_3.

Fig. 5.15 displays the concentrations on probes P_1, P_2, and P_3 against the angle of orienta-

tion ϕ. The trends of the results are similar (or the patterns in drug distribution are observed to be similar) for E_1 and E_2. However, the drug concentration is less for E_2 with smaller values of ϕ, while more in the case of larger values of ϕ. It is because a_2 is larger for E_2, and hence, the cell height leads to less drug penetration for smaller values of ϕ; however, the cell height for E_1 is greater than that for E_2 for larger ϕ and hence leads to more drug concentration for E_2. The overall concentration difference for E_2 is ≈ 4 % for $0 \leq \phi \leq \frac{\pi}{2}$, which is significantly lower than that for the case of E_1 (where a minimum of ≈ 8 %).

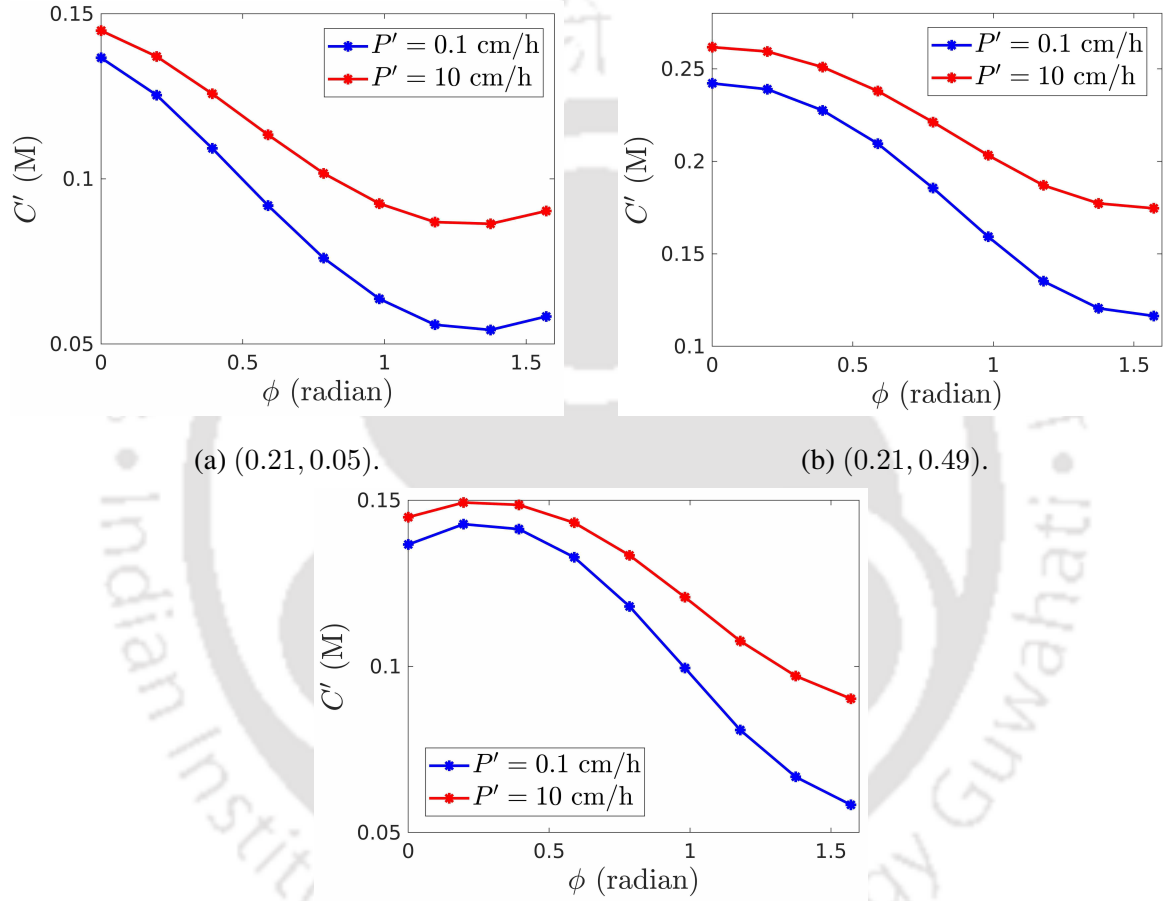

(a) $(0.21, 0.05)$. (b) $(0.21, 0.49)$.

(c) $(0.21, 0.95)$.

Figure 5.16: Drug concentrations for two different permeability values on probes (a) P_1, (b) P_2, and (c) P_3.

Effects of cell permeability

As the permeability of cell membrane varies across the different types of cells [43], and also across the tissues, it is important to study its effects on drug distribution. The experiments are conducted with the model parameters as stated in Section 5.2.2 with $\kappa' = 0.1$ cm/h for

$P' = 0.1$ and 10 cm/h.

Fig. 5.16 shows drug concentrations against ϕ on the probes $P_1, P_2,$ and P_3. One can observe that the drug distribution patterns are qualitatively similar for $P' = 0.1$ and 10 cm/h as the drug concentration either decreases or increases with ϕ for both the cases. However, the drug concentration is higher for $P' = 10$ cm/h, which is expected as the large permeable membrane will allow more drug to penetrate into the tissue. For these values of P', the gap in the curves of drug concentration increases with ϕ.

5.3 Sensitivity analysis

The values of the model input parameters are usually obtained from the experiments or estimated by specific mathematical tools, which are prone to uncertainties as the measuring instruments are embodied with certain errors. The experimental setup itself may not mimic the reality and may lead to incorrect findings usually with acceptable errors. Due to the possible uncertainties in the input parameters, theoretical predictions of a mathematical model may overestimate the findings. Sensitivity analysis is a useful tool for predicting the effects of variations in the input parameters on the model output and help in the physical interpretation of the model.

The normalized sensitivity coefficient (NSC) used for the analysis of sensitivity of the input parameters to the model response is defined as,

$$\text{NSC} = \frac{X}{\text{mean}(C')} \frac{\partial C'}{\partial X}, \tag{5.7}$$

where X is an input parameter, and mean(C') denotes the mean value of C' over the spatial domain. As the input parameters differ by several orders, normalized values are particularly useful to compare the sensitivity of different parameters. The nominal values of the parameters are mentioned in Section 5.2.2, and the NSC is calculated by perturbing the nominal values by 10 %. The results are displayed in Fig. 5.17.

From the figure, one can observe that the highest deviation in NSC value from zero is obtained for λ' (edge length of the microscale domain), and hence, λ' is the most sensitive model input parameter. The order of importance in terms of sensitivity is as λ', a_1, D'_E, ϕ, a_2, and κ', so accordingly the amplitude of their curve diminishes to zero. The system is least sensitive to P' and D'_I due to the small contribution of cell properties on drug penetration. The NSC values are positive for some parameters such as λ' and D'_E, since the concentration

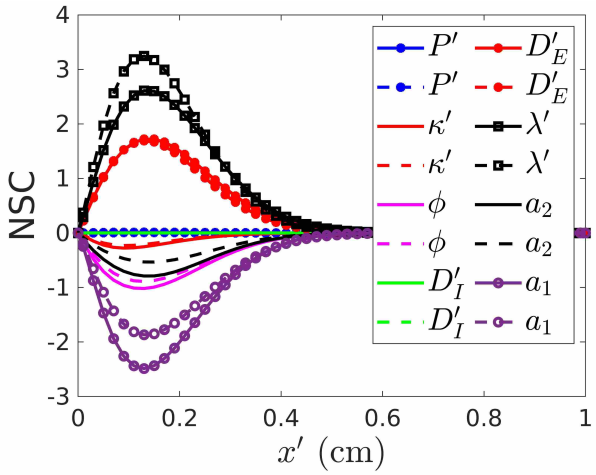

Figure 5.17: Normalized effect of the input parameters on the model output. Results with 'dashed lines' are shown for the 10% reduction in the input parameter value while 'solid lines' are for the 10% increase. These results are along the line $y' = 0.49$.

increases on increasing their values. Whereas, the NSC values are negative for parameters a_1, a_2, and ϕ, as the concentration increases with a decrease in the parameter value. Note that the NSC values tend to zero for $x' = 0.4$ onwards owing to the concentration approaches zero.

These analyses will be advantageous for biological applications. It can be noticed that the extracellular parameters are more sensitive to the model response compared to the intracellular parameters.

5.4 Conclusions

In this chapter, the FVHMM-p is improved to accurately simulate the effects of biological (elliptical) cell orientation on drug penetration and distribution in the tissue domain. As a part of this improvement, two novel reconstruction operators are proposed to get physically realistic results. It is observed that the reconstruction operator may affect the macroscopic physics of the problem. The convection boundary condition is also modelled in the HMM framework to account for the drug movement through the tissue boundary owing to the realistic physiological conditions. Numerical results are validated with the experimental results.

The effects of cell orientation on penetration and distribution of drug in the biological tissues are investigated for the first time. The following findings are observed from the simulation results:

1. The orientation of a cell is a prominent factor that can affect the penetration and distribu-

tion of a drug in tissues significantly.

2. In the proposed model, drug achieves maximum penetration for (the angle of cell rotation) $\phi = 0$ and minimum for $\phi = \frac{\pi}{2}$, which is true for the case where semi-major axis of the elliptical cell (with $\phi = 0$) lies in the x-direction.

3. The application of the convection boundary condition on the lateral boundaries leads to different drug distribution patterns in the proximity of the boundary.

4. The drug concentration in the tissue domain can be affected by approximately 8 % on cell rotation from 0 to $\pi/2$, which is a significant one.

5. The angle of cell orientation $\phi = \frac{\pi}{4}$ is a critical value for ϕ, above and below of which different patterns are observed in drug distribution and penetration near the tissue boundary.

6. It is observed that the drug distribution patterns are qualitatively similar for different cell membrane permeabilities; however, the drug concentration increases for larger permeability values.

7. The local sensitivity analysis is performed to determine the dependency of the model response on the input parameters. It is observed that the model is most sensitive to the size of the microscale domain, whereas least sensitive to the cell membrane permeability and intracellular diffusivity.

8. The parameters related to the extracellular space are more sensitive to the model response as compared to the ones related to the intracellular space.

Thus, the cell orientation is a vital factor in drug delivery.

भारतीय प्रौद्योगिकी संस्थान गुवाहाटी
Indian Institute of Technology Guwahati

CHAPTER 6

EFFECTS OF FLUID FLOW AND METABOLISM ON DRUG DELIVERY

Due to the geometrical resistances and increase in interstitial fluid pressure, the effects of advection is so small that it is neglected in some studies. However, the transport of drugs from capillary to the interstitial space (tissue) happens through diffusion as well as by advection in most of the regions [69]. As the advection of a solute merely depends on its size, fluid flow is specifically helpful for transporting larger constituents in the human body. The role of advection versus that of diffusion in the extracellular space depends on the molecular weight of solute and the glycosaminoglycan content [54]. Another biophysical phenomenon, metabolism, alters the drug molecules chemically once they enter the body. Drug metabolism may deactivate some drugs and increase their water solubility, making elimination easier through the urine or bile from the body. In general, metabolism decreases the therapeutic efficacy of a drug. The enzymes responsible for drug metabolism are found extracellularly as well as intracellularly [57].

The FVHMM-p has considered diffusion phenomenon for the study of drug penetration and distribution into biological tissue (Chapter 4). The above discussion motivates us to comprehend the effects of fluid flow and drug metabolism in the FVHMM-p. It is observed that the drug penetration and distribution into tissues are affected by the cellular geometry and the cell membrane permeability in diffusion-based mass transport. Also, the size of the particle may play a crucial role in the penetration of a drug. The present chapter incorporates the advected transport and drug metabolism in the FVHMM-p. This improved model is simulated to answer

the following questions. Does the cell geometry play a significant role in drug delivery into the tissues where fluid flow has a crucial role in transporting the essential constituents? As the advective transport of a drug merely depends on the particle size, does the particle size play a key role in drug penetration? Under what situations fluid flow is more useful than the diffusion in drug delivery process? Does the permeability of the cell membrane affect drug penetration into the tissues? What is the significance of metabolism in the penetration and distribution of a drug into the tissue? The results are analysed with and without fluid flow. It is observed that drug penetration may be affected by the drug metabolism.

As the proposed model involves several parameters, the understanding of the importance of input parameters is not readily available. The variations in the parameter values may produce significant effects on the model output. To address this issue, local sensitivity analysis is also performed for the model to determine its response owing to the variations in input parameters.

6.1 Model formulation

In order to model drug transport process, the tissue domain $(\Omega'(\subset \mathbb{R}^2))$ is considered to be a two-dimensional cross-section, and the cells are assumed to be dispersed therein. The intra- and extra-cellular fluids are considered to be isotropic and homogeneous. The model, based on the HMM framework, involves two scales: tissue (macro) scale and cellular (micro) scale. At the macroscale, the tissue domain is treated as a porous medium. The diffusion phenomenon is incorporated through the microscopic level as in Chapter 5, and the transportation due to advection is implemented at the continuum scale. Assume that the drug is mixed with the biological fluid, the general mass-balance relation at macro level, which includes the drug source/sink (S'), can be written as,

$$\frac{\partial C'(t', x', y')}{\partial t'} + \nabla' \cdot (\mathbf{v}' C') = \nabla' \cdot \mathbf{F}' + S', \quad (t', x', y') \in (0, \tau'] \times \Omega', \tag{6.1}$$

with the initial condition

$$C'(0, x', y') = C'_0(x', y'), \quad (x', y') \in \Omega', \tag{6.2}$$

where C' denotes the drug concentration. $\mathbf{F}' = (F'_{x'}, F'_{y'})$, the diffusive flux vector, is unknown at the macroscale and can be determined using the microscopic cellular level information. $\mathbf{v}' = (u', v')$ is a velocity vector. The right-most term (S') accounts for the source/sink in the tissue

domain. It incorporates the drug metabolism in the present study and is defined as [32],

$$S' = -\frac{V'_{max}C'}{K'_m + C'}, \tag{6.3}$$

where V'_{max} denotes the maximum drug metabolism rate due to the enzymatic reaction, and K'_m denotes the drug concentration at which metabolism is half maximal. The boundary conditions at the left and right boundaries are used as,

$$C'(t, 0, y) = C'_{in}, \tag{6.4}$$

$$C'(t, L, y) = C'_{out}, \tag{6.5}$$

respectively. The length L is taken to be sufficiently large to ensure that $C'_{out} = 0$ for the stipulated time. At the lateral boundaries, no flux condition is specified.

Consider that the drug is mixed with the biological fluid, and it does not affect the transport of fluid. Then velocity vector obeys the Darcy's law, which is defined as,

$$\mathbf{v}' = K\nabla' p, \tag{6.6}$$

where p denotes the pressure and K is Darcy's coefficient. The inlet velocity is specified as $u' = u'_0$ and $v' = 0$, and the lateral boundaries are considered as no flux boundaries. Note that the velocity vector in the tissue domain is given to be $\mathbf{v}' = (u'_0, 0)$.

Let $\tilde{C}$ be the typical concentration scale (maximum of initial concentration), $\tilde{L}$ be the typical length scale (x'-directional length of tissue domain) and $\tilde{U}$ be the typical velocity scale (inlet velocity). The typical time-scale $\left(\tilde{t}\right)$ is obtained as $\tilde{t} = \tilde{L}/\tilde{U}$. Then, the following non-dimensional parameters are used for the non-dimensionalization of the macroscale model,

$$x = \frac{x'}{\tilde{L}}, y = \frac{y'}{\tilde{L}}, u = \frac{u'}{\tilde{U}}, v = \frac{v'}{\tilde{U}}, t = \frac{t'}{\tilde{t}}, C = \frac{C'}{\tilde{C}}, \text{ and } \mathbf{F} = \frac{\mathbf{F}'}{\tilde{C}\tilde{L}/\tilde{t}},$$

The non-dimensional macroscale model can be written as,

$$\frac{\partial C(t, x, y)}{\partial t} + \nabla \cdot (\mathbf{v}C) = \nabla \cdot \mathbf{F} + S, \quad (t, x, y) \in (0, \tau] \times \Omega, \tag{6.7}$$

with the initial condition

$$C(0, x, y) = C_0(x, y), \quad (x, y) \in \Omega. \tag{6.8}$$

The term $S = -\frac{V_{max}C}{K_m + C}$, where $V_{max} = V'_{max}\frac{\tilde{L}}{\tilde{U}\tilde{C}}$ and $K_m = K'_m/\tilde{C}$. $\mathbf{F}, \Omega,$ and τ are the dimensionless variants of $\mathbf{F}', \Omega',$ and τ', respectively. The model can be defined schematically as in the Fig. 6.1.

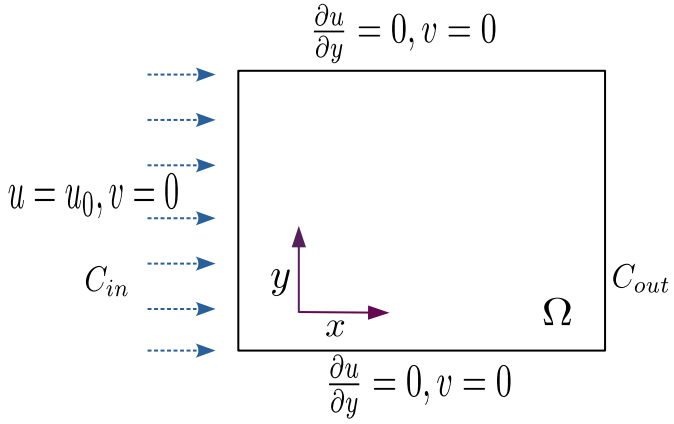

Figure 6.1: Schematic diagram of the tissue domain and the specified boundary conditions.

6.2 Solution procedure

The FVHMM-p (Chapter 5) is employed for the diffusion part and further the model (FVHMM-p) is extended to incorporate the advection and metabolism phenomena. The solution procedure includes the macro-micro coupling of the microscopic cellular phenomenon to the macroscopic level (schematically shown in Fig. 4.1). The method is briefly explained as follows.

- The finite volume discretization is adopted for the solution of the macroscale model given in the Eq. (6.7), and the discretized form for a typical CV is obtained as [42],

$$\frac{C_{k,l}^{n+1} - C_{k,l}^{n}}{\Delta t} + u\frac{C_{e_f}^{n} - C_{w_f}^{n}}{h} + v\frac{C_{n_f}^{n} - C_{s_f}^{n}}{h} = \frac{1}{h^2}\left[F_{e_f}^{n} + F_{n_f}^{n} - F_{w_f}^{n} - F_{s_f}^{n}\right] - \frac{V_{max}C_{k,l}}{K_m + C_{k,l}}, \tag{6.9}$$

where $C_{k,l}^{n}$ denotes the macroscopic concentration in the CV (k,l), $k,l = 1,2,\ldots,N$, at time $t_n = n\Delta t$, Δt is the macroscopic time step and n is a non-negative integer. F_f^n and C_f^n denote the diffusion flux and concentration on the face f $(= e_f, w_f, n_f, s_f)$, respectively. The first-order schemes display artificial diffusivity, whereas the second-order schemes, such as upwind and central difference schemes, develop spurious oscillations in the results of advection dominated transport processes. A bounded upwind scheme namely SUPERBEE adopted to approximate the concentration at the face (for advection

part) is defined as [13],

$$C_f = \begin{cases} C_U, & \text{if } \hat{C}_U \notin [0,1], \\ 2C_U - C_R, & \text{if } 0 \le \hat{C}_U < 1/3, \\ \frac{1}{2}(C_D + C_U), & \text{if } 1/3 \le \hat{C}_U < 1/2, \\ \frac{3}{2}C_U - \frac{1}{2}C_R, & \text{if } 1/2 \le \hat{C}_U < 2/3, \\ C_D, & \text{if } 2/3 \le \hat{C}_U \le 1, \end{cases} \tag{6.10}$$

where C_f is the concentration on a face of the CV as depicted in Fig. 6.2. C_R, C_U, and C_D are the concentrations in the three consecutive control volumes as shown in the Fig. 6.2. $\hat{C}_U$ is the normalized variable defined as,

$$\hat{C}(t,x,y) = \frac{C(t,x,y) - C_R^n}{C_D^n - C_R^n}. \tag{6.11}$$

- The fluxes are obtained from the microscale models constructed on each face of the CV as discussed in Section 4.1.1.

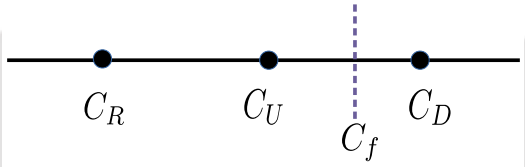

Figure 6.2: Stencil for the SUPERBEE upwind scheme.

6.3 Numerical convergence and validation with the experimental results

In this section, the convergence of the method is discussed, and a comparison with experimental results is also shown.

6.3.1 Convergence of the method

An example is constructed by taking a cell-free domain (i.e., no cell is considered), so that the analytical solution can be obtained. The macroscale domain is considered to be $\Omega = (0,1) \times$

$(0, 1)$. The velocity vector is chosen to be $\mathbf{v} = (1, 1)$ and the diffusivity $D = 1$. The initial and Dirichlet boundary conditions for the macroscale model (Eq. 6.7) are chosen as,

$$C_0(x, y) = 0, \quad (x, y) \in \Omega, \tag{6.12}$$

and

$$C(t, x, y) = \sin(\pi x)\sin(\pi y), \quad (t, x, y) \in (0, 1] \times \partial\Omega, \tag{6.13}$$

respectively, and the source term is considered as,

$$S = \exp(-t)\left[\pi \sin(\pi(x + y)) + (2\pi^2 - 1)\sin(\pi x)\sin(\pi y)\right], \quad (t, x, y) \in (0, 1] \times \Omega, \tag{6.14}$$

to obtain the exact solution

$$C(t, x, y) = \exp(-t)\sin(\pi x)\sin(\pi y), \quad (t, x, y) \in (0, 1] \times \Omega. \tag{6.15}$$

In the numerical experiments, λ is chosen to be 10^{-3} and the microscale domain is discretized by the mesh size 30×30. The simulation results are obtained for $t = 1$ with the macroscopic temporal step $\Delta t = 10^{-4}$. The convergence results are shown in Table 6.1 where maximum error estimates obtained at various macro-spatial grids are displayed. It is evident that the macro-spatial grid refinement decreases the maximum errors; hence, the method converges. Fig. 6.3 shows that the contour plots for analytical and numerical solutions are indistinguishable on a mesh 20×20.

Table 6.1: Maximum error estimates for the macro-spatial grid refinement.

Mesh size	$\|\|E_h\|\|_\infty$
10×10	3.081×10^{-3}
20×20	1.031×10^{-3}
30×30	5.112×10^{-4}
40×40	3.038×10^{-4}

6.3.2 Validation with the experimental results

The multiscale method is validated with the experimental results of Huang et al. [23]. They performed an *in vitro* experiment on the spheroid-on-chip system where multicellular spheroids

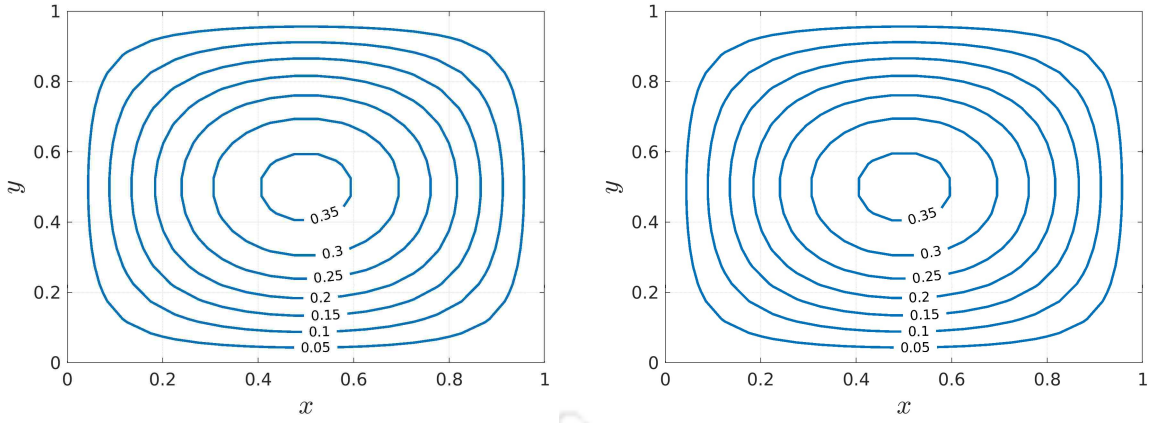

(a) Analytical solution (b) Numerical solution

Figure 6.3: Contour plots of (a) analytical and (b) numerical results on 20×20 finite volume mesh at time $t = 1$.

are fixed to mimic the tissue structure. The comparison is made with the fluid velocity $\mathbf{v}' = (0, 0)$ and $V'_{max} = 0$ M/h, and the other parameters are considered as, $D'_E = 1.8 \times 10^{-7}$ cm^2/h, $D'_I = 10^{-8}$ cm^2/h, and $P' = 0.1$ cm/h. The numerical experiment is performed in the macroscale domain $[0, 0.01] \times [0, 0.01]$ for $t' = 2$ h. The results are shown in Fig. 6.4, and it can be seen that the numerical and experimental results are in good agreement.

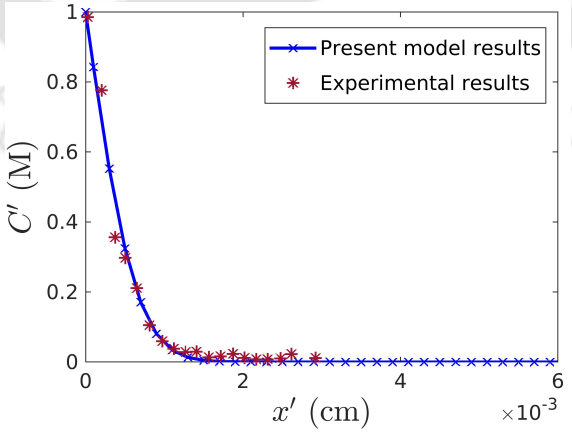

Figure 6.4: Validation with the experimental results of Huang et al. [23].

6.4 Effects of fluid flow and drug metabolism on penetration and distribution of a drug

The intracellular viscosity μ_I is set to 5 cP [15], and μ_E is taken to be 1 cP [63]. The numerical experiments are conducted in 1×1 cm^2 domain, and the drug delivery is studied at $\tau' = 5$ h (h – hour) with $\Delta t' = 5 \times 10^{-4}$ h. The edge length of the microscale domain is taken to be 10^{-3} cm, and the default shape of the cell is considered circular of radius 4.1×10^{-4} cm. The values of other parameters are listed in Table 6.2. Note that the model leads to uniform concentration distribution along the y'-direction. Hence, the macroscale domain is discretized along the x'-direction with the mesh size 100×1 (i.e., 100 control volumes in x'-direction and one control volume in y'-direction). The microscale domain is discretized by 100×100 mesh size. This discretization results in grid-independent outcomes.

Table 6.2: Values of the physical parameters.

Parameter (units)	Values	Description (Ref.)
P' (cm/h)	0.1	Cell membrane permeability
u_0' (cm/h)	0.036	Darcy's flow velocity ([33])
μ_I (cP)	5	Intracellular viscosity ([15])
μ_E (cP)	1	Extracellular viscosity ([63])
V_{max}' (M/h)	1.8×10^{-2}	Maximal drug metabolism rate ([33])
K_m' (M)	10^{-5}	Concentration at which drug metabolism is half maximal ([33])
τ' (h)	5	Stipulated simulation time (This work)
r (nm)	$1 - 100$	Drug particle size (This work)
T (Kelvin)	310	Temperature (This work)

6.4.1 Effects of drug particle size

In the Chapters 3 and 4, where the diffusion phenomenon was considered to be the driving force, it is observed that the size of a drug particle has a strong correlation with its penetration and distribution efficacy in tissues. This section performs numerical experiments with the drug particles of sizes 1, 10, and 100 nm and the inlet fluid velocity $u_0' = 0.036$ cm/h.

Fig. 6.5 shows the effects of drug particle size on its penetration and distribution efficacy in tissue. Fig. 6.5(a) displays the results with advection while Fig. 6.5(b) shows the results where advection is neglected. It can be observed that the concentration of larger size particles is significantly high near the inlet (up to $x' = 0.2$, Fig. 6.5(a)) as advection (fluid flow) helps the drug particles to move faster into the tissue. The concentration of smaller size particles is relatively low near the inlet region (for $x' \in (0, 0.2)$) due to their fast diffusion. The concentration decays faster in the order of increasing particle size in the region $x' = 0.2$ onwards (Fig. 6.5(a)). However, without advection (i.e., the case of diffusion only), the concentration of larger size particles decays sharply as soon as the drug enters the tissue (Fig. 6.5(b)). The particles of sizes 10 and 100 nm fail to reach the location $x' = 0.2$ in the stipulated time (5 h).

Fig. 6.5(c) shows the drug penetration depth, the distance measured from the inlet to the location where drug concentration reaches 1 % of 1 M (the input concentration). For $r = 1$ nm, drug penetrates up to a depth $x' = 0.4$ without advection (Fig. 6.5(b)), and it reaches to $x' = 0.6$ with advection (Fig. 6.5(a)). Whereas, for $r = 10$ nm, penetration is almost twice with advection phenomenon in comparison to the diffusion only and nearly thrice for 100 nm particles (see Fig. 6.5(c)). So, advection improves the penetration of larger size particles significantly. From the results, one can also conclude that the smaller size drug particles penetrate deeper in fluid flow regions though the advection merely depends on the size of solute particles.

6.4.2 Effects of cell geometry

As the tissue morphology is determined by the cells, it is paramount to understand the impact of cell geometry on drug delivery. Numerical experiments are conducted in three ways by varying cell parameters a_1 and a_2 to incorporate the different scenarios of cellular structure in the tissue domain. Firstly, the experiments are conducted by varying cell radius (for circular cell), secondly, the height of the cell is varied by keeping the cell width unchanged, and lastly, by varying the cell width with fixed cell height.

The experiments are performed with cell radii, $2.1 \times 10^{-4}, 3.1 \times 10^{-4}$, and 4.1×10^{-4} cm. Fig. 6.6 shows the results for particles of sizes 1, 10, and 100 nm. For $r = 1$ nm, one can observe that the drug penetration is affected by the change in cell size (Fig. 6.6(a)), on the other hand, no effect is noticed for $r = 100$ nm (Fig. 6.6(c)), whereas the moderate effects are seen for $r = 10$ nm (Fig. 6.6(b)). Larger size particles ($r = 100$ nm) show very small difference in their penetrations for different cell sizes because advection dominates over

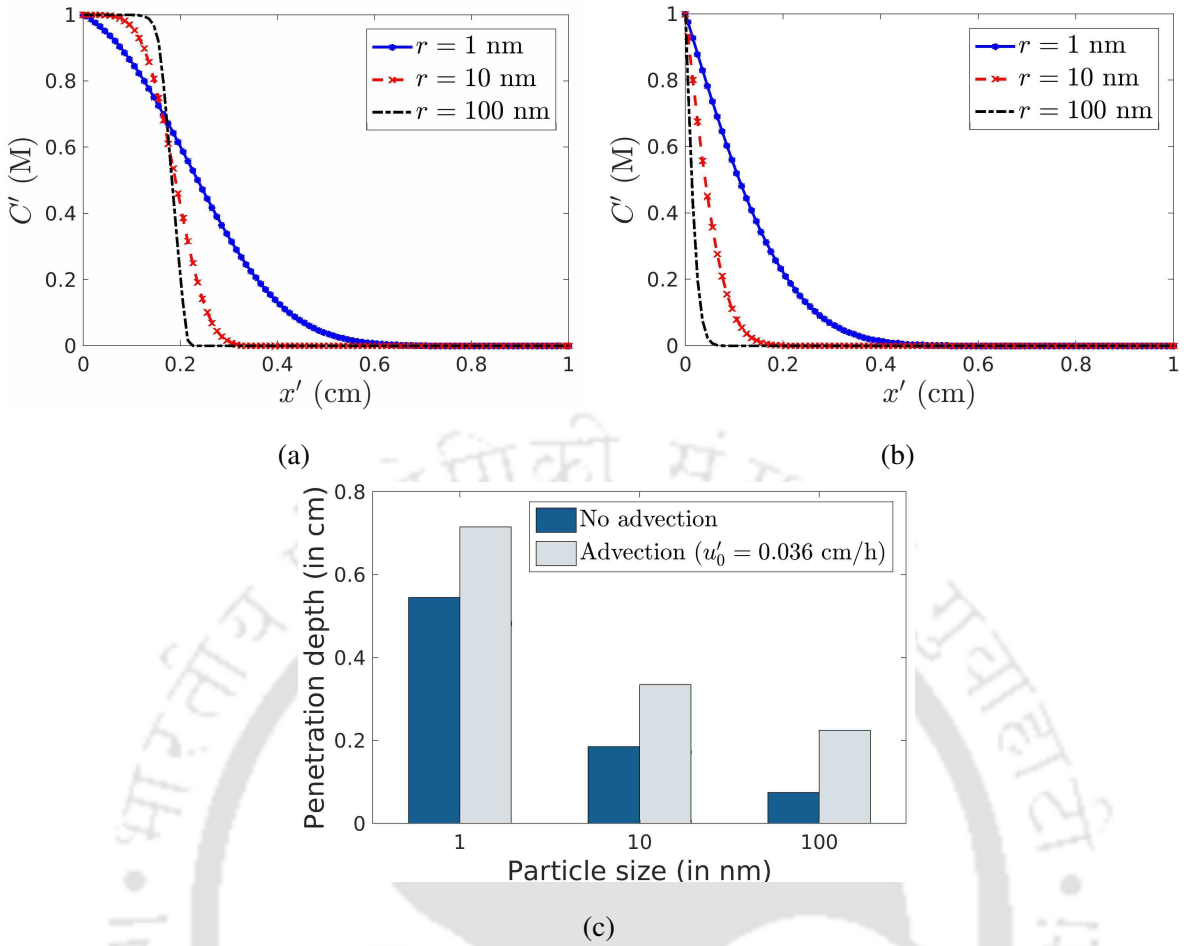

Figure 6.5: Effects of drug particle size on its penetration and distribution for (a) $u_0' = 0.036$ cm/h and (b) $u_0' = 0$ cm/h. (c) Penetration depths of drugs observed in (a) and (b).

diffusion in their transportation (Fig. 6.6(c) and (d)). While the penetration of 1 nm particles increases significantly from 0.715 cm to 0.965 cm on decreasing the cell radius from 4.1×10^{-4} to 2.1×10^{-4} cm (Figs. 6.6(a) and (d)). It is clear that the drug penetration increases on decreasing the cell size irrespective of drug particle size (Fig. 6.6(d)). Since the microscale domain (λ) is fixed, a change in cell size increases/decreases the extracellular spatial volume, which is the main medium of drug transport. A smaller cell leads to more extracellular space and consequently greater penetration is obtained. From the results, it is easy to conclude that the smaller size particles take the advantage of extracellular space created in the case of smaller cells. Thus, the smaller particles are capable to penetrate through the available pores of the tissue domain.

The other experiment is performed by keeping cell width ($a_1 = 2.1 \times 10^{-4}$ cm) fixed and varying the cell height (a_2) as, $2.1 \times 10^{-4}, 3.5 \times 10^{-4}$, and 4.5×10^{-4} cm. Note that the

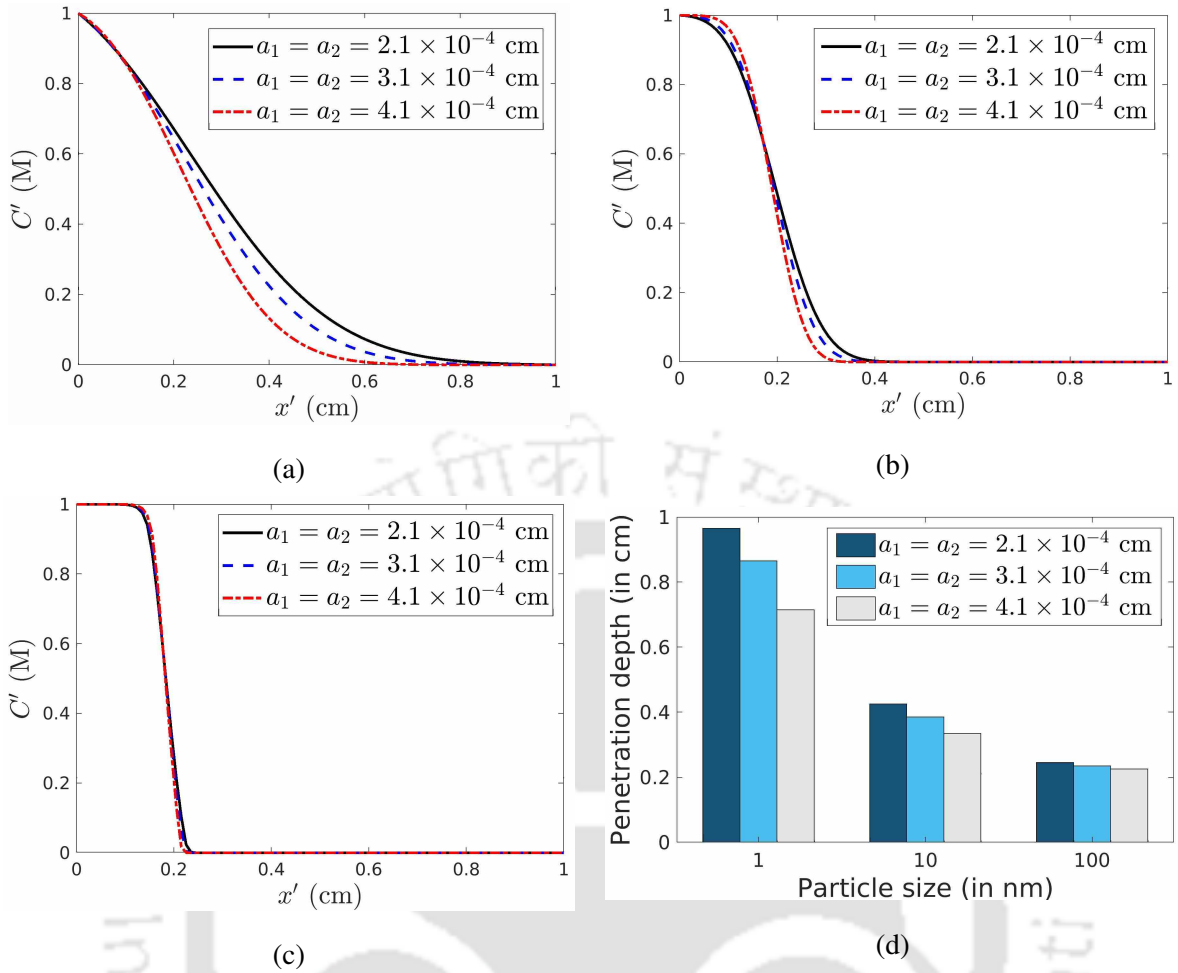

Figure 6.6: Effects of cell size on dug penetration ($u_0' = 0.036$ cm/h, $V_{max}' = 0$ M/h) for (a) $r = 1$ nm, (b) $r = 10$ nm, and (c) $r = 100$ nm. (d) Penetration depths of drugs observed in (a), (b), and (c).

results (Fig. 6.7) are similar to the case where experiments are conducted with different cell radii (Fig. 6.6). The drug penetration decreases with an increase in cell height (Fig. 6.7(d)). It can be noticed that an increase in cell height decreases the penetration of smaller size particles significantly (Fig. 6.7(a)). This is due to inhibition of drug diffusion by the cell height that is incorporated through the microscopic resolution of cellular phenomena.

In the next one, cell height ($a_2 = 2.1 \times 10^{-4}$ cm) is kept fixed and the width (a_1) varies as, $2.1 \times 10^{-4}, 3.5 \times 10^{-4},$ and 4.5×10^{-4} cm. In contrary to the cell height, the cell width does not affect the penetration and distribution of drug irrespective of its particle size (Fig. 6.8).

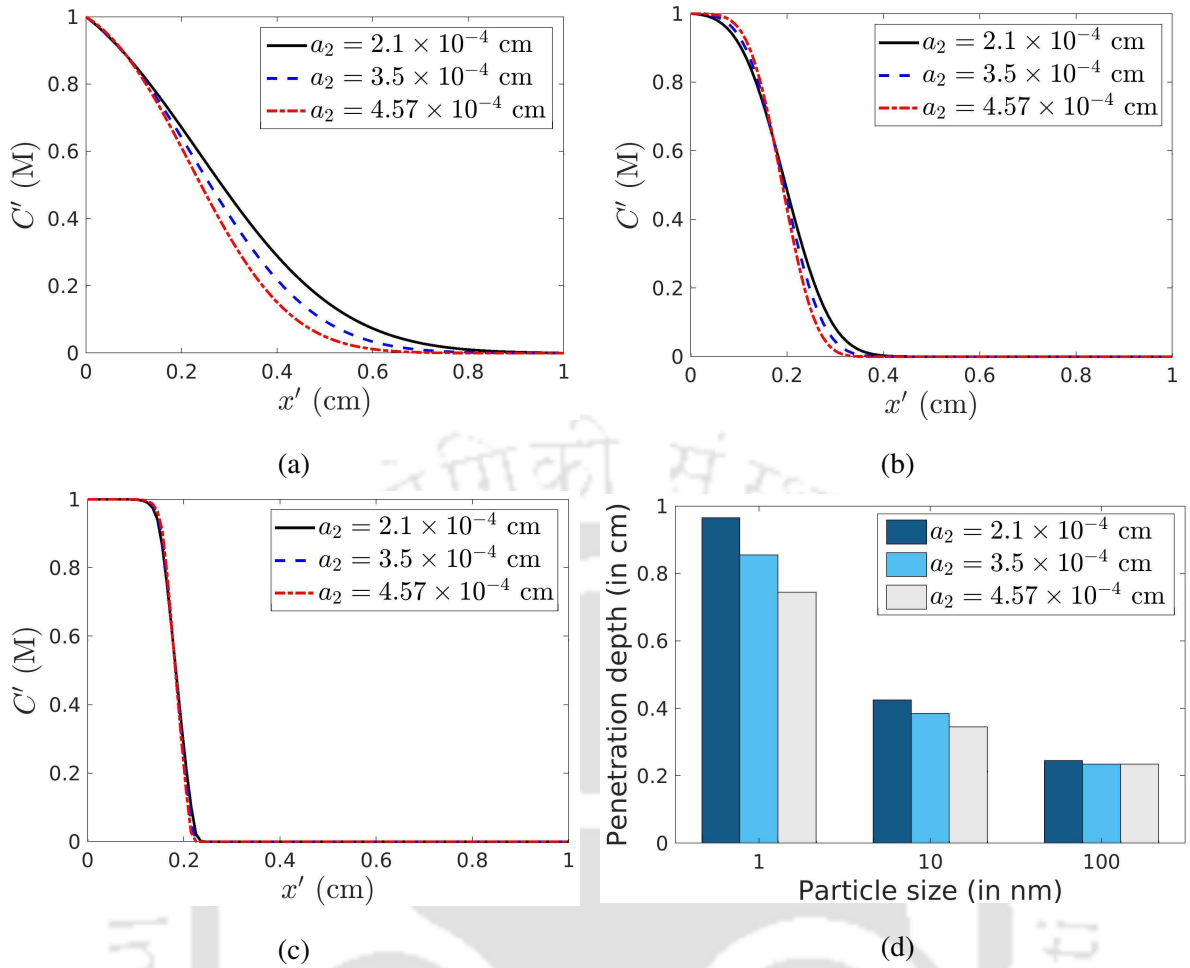

Figure 6.7: Effects of cell height on drug penetration ($a_1 = 2.1 \times 10^{-4}$ cm, $u_0' = 0.036$ cm/h and $V'_{max} = 0$ M/h) for (a) $r = 1$ nm, (b) $r = 10$ nm, and (c) $r = 100$ nm. (d) Penetration depths of drugs observed in (a), (b), and (c).

6.4.3 Effects of permeability

As the cell membrane permeability (P') varies across the tissues, numerical experiments are performed to investigate the permeability effects on drug penetration and distribution. Fig. 6.9 shows the results for $P' = 0.1$ cm/h and 10 cm/h for different size particles. Drug penetration depths are shown in Fig. 6.9(b).

Drug penetration increases with the increase in cell membrane permeability (Fig. 6.9(b)). The effects are significantly large for small particles ($r = 1$ nm), whereas, results for $r = 100$ nm are identical for $P' = 0.1$ and 10 cm/h. The effects are in line with the Chapter 4, which has shown some effects of permeability on drug penetration for each size of particles, where diffusion phenomenon was the only driving force of drug transport.

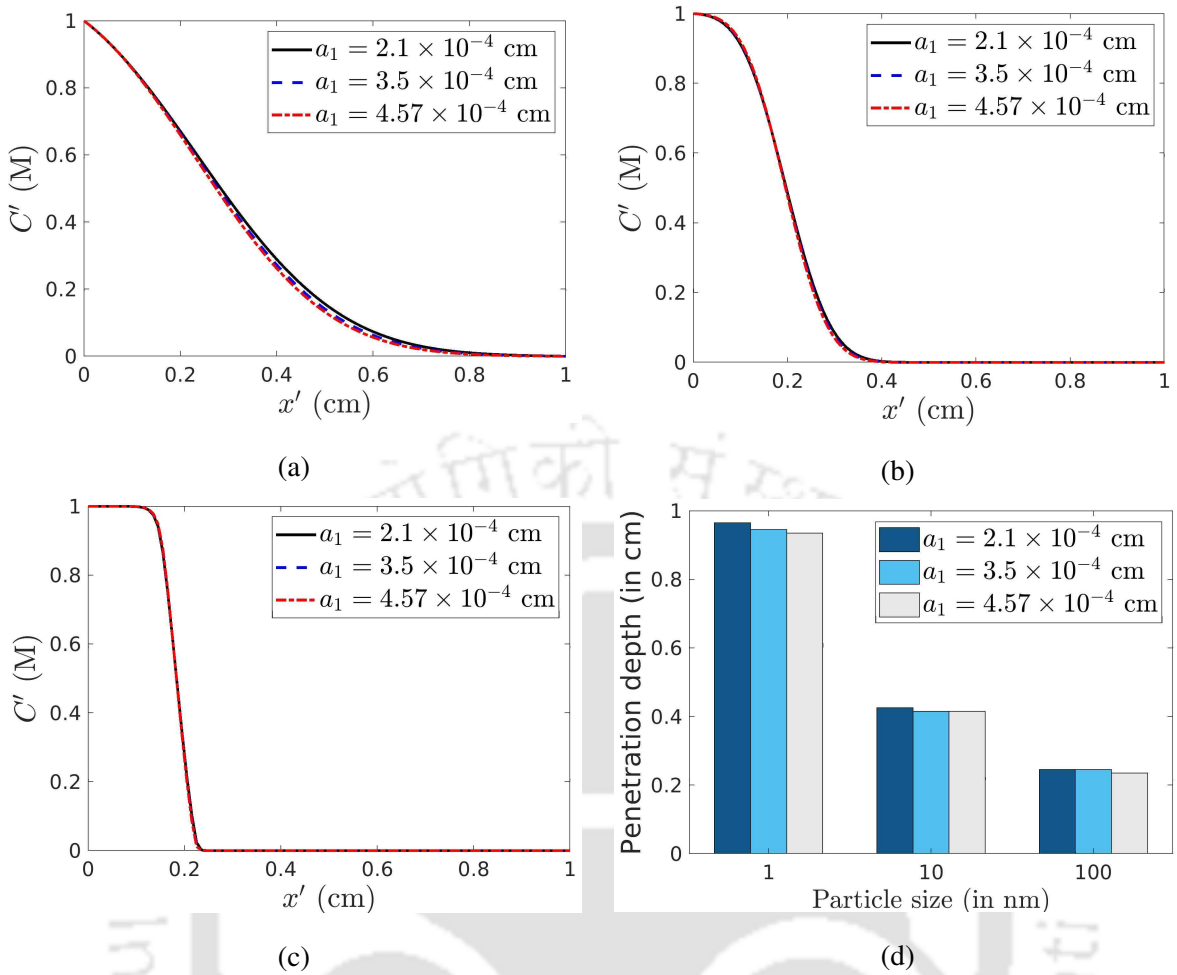

Figure 6.8: Effects of cell width on drug penetration ($a_2 = 2.1 \times 10^{-4}$ cm, $u_0' = 0.036$ cm/h, and $V_{max}' = 0$ M/h) for (a) $r = 1$ nm, (b) $r = 10$ nm, and (c) $r = 100$ nm. (d) Penetration depths of drugs observed in (a), (b), and (c).

6.4.4 Effects of drug metabolism

Drug metabolism is a basic biophysical phenomenon that takes place by enzymatic reactions. Some drugs may be metabolized during their penetration or before reaching the site of action. Metabolism may deactivate some drug already entered the body and make it more water-soluble to excrete easily. Consequently, drug metabolism may affect the penetration and distribution of drug in the tissues. To understand the effects, numerical experiments are conducted with and without fluid flow (advection). For drug metabolism, the parameters are chosen as $V_{max}' = 1.8 \times 10^{-2}$ M/h and $K_m' = 10^{-5}$ M [33].

First, the results are analysed for 1 and 10 nm particles by neglecting advection ($u_0' = 0$ cm/h). The experiments are conducted with and without drug metabolism, and the results are shown in Fig. 6.10(a). It can be observed that the drug penetration decreases due to metabolism

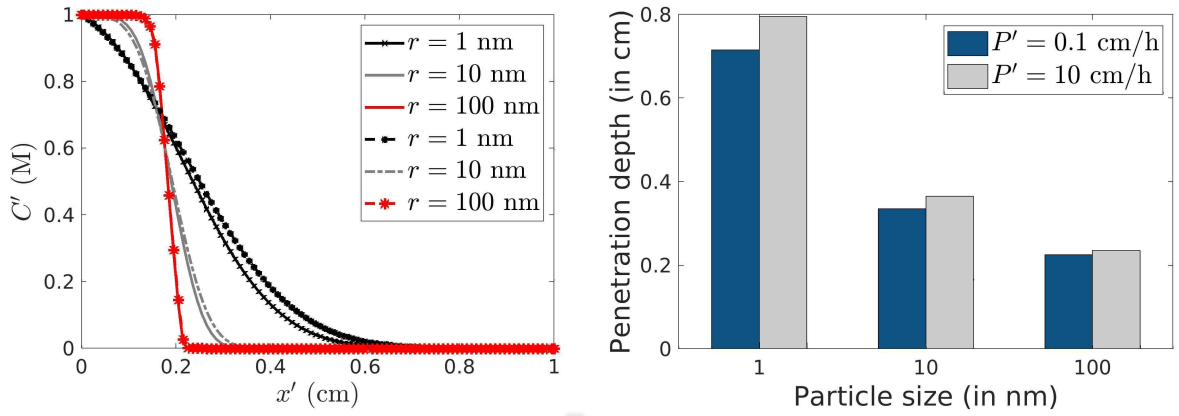

(a) (b)

Figure 6.9: (a) Effects of cell membrane permeability on drug penetration ($u_0' = 0.036$ cm/h, $V_{max}' = 0$ M/h). Dashed lines '- -' show the results for $P' = 10$ cm/h while solid lines '–' display the results for $P' = 0.1$ cm/h. (b) Penetration depth for each permeability values.

that constantly removes the drug from the tissue. For 1 nm particles, it can be observed that the penetration difference with and without drug metabolism is ≈ 0.2 cm. The penetration reduction due to metabolism is significant as the penetration depth is reduced from 0.54 cm to 0.35 cm. Also, for 10 nm particles, penetration reduces from 0.185 cm to 0.125 cm, almost an 1/3rd reduction, due to drug metabolism. Clearly, metabolism can reduce drug penetration in no flow condition.

Next, to investigate the results in fluid flow regions of tissue (i.e., with advection), the inlet fluid velocity is considered as $u_0' = 0.036$ cm/h. Results are shown in Fig. 6.10 (b). The concentration curves are indistinguishable, concluding that the drug metabolism may not affect penetration in fluid flow regions. This may be due to the supply of drug that would be sufficient to surpass the metabolism effects.

6.5 Sensitivity analysis

Sensitivity analysis is performed using the normalized sensitivity coefficient (NSC) as defined in Section 5.3. The nominal values for some parameters are mentioned in the Table 6.2, and the others are taken as, $\lambda' = 10^{-3}$ cm, $a = 4.1 \times 10^{-4}$ cm (cell radius), $D_I' = 1.634843552 \times 10^{-3}$ cm/h, and $D_E' = 8.174217762 \times 10^{-3}$ cm/h. The NSC is calculated by perturbing the nominal values by 10 %.

In order to better interpret the results, the sensitivity analysis is performed by considering

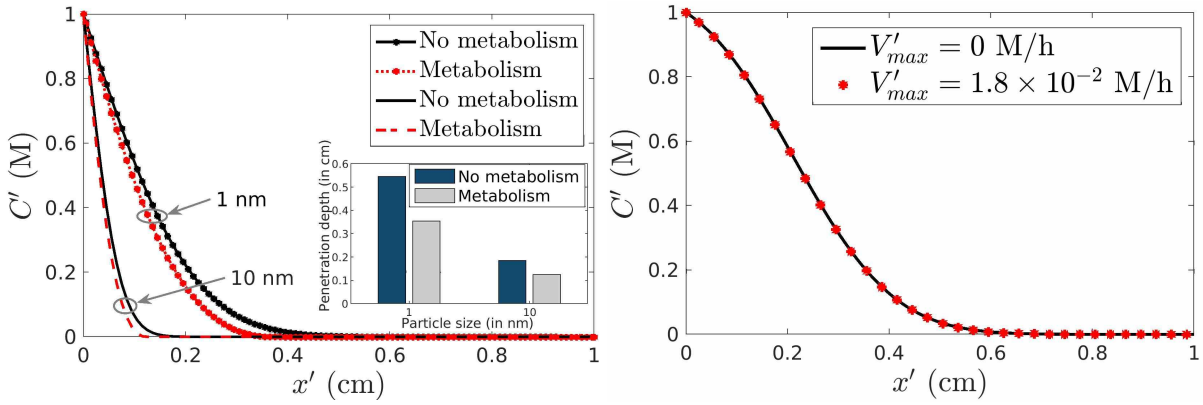

(a) (b)

Figure 6.10: Results of metabolism on penetration and distribution of drug (a) with no fluid flow $(u'_0 = 0)$ for 1 and 10 nm drug particles and (b) with fluid flow $(u'_0 = 0.036)$ cm/h for 1 nm particles ($V'_{max} = 1.8 \times 10^{-2}$ M/h, $K'_m = 10^{-5}$ M).

different processes (advection, diffusion, and drug metabolism) in the model separately.

6.5.1 Sensitivity of the parameters without advection

The model accounts for the diffusion and drug metabolism while, firstly, the advection term is dropped for the sensitivity analysis. The NSC values are shown in Fig. 6.11. The values are positive for the parameters P', λ', D'_I, D'_E, and K'_m while negative for V'_{max} and a. The positive and negative NSC values reflect the positive and negative change in the drug concentration, respectively on an increase in the parameter value. It can be noticed that the cell radius (a) is the most sensitive parameter while K'_m is the least one. The order of importance in sensitivity decreases in the order a, λ', D'_E, V'_{max}, P', D'_I, and K'_m. The pattern is similar for each curve, and each NSC curve retains the same sign throughout the spatial domain. The NSC curves approach zero nearly $x' = 0.5$, which is on account of the drug concentration that reaches zero.

6.5.2 Sensitivity of the parameters with advection

Numerical experiments for sensitivity are conducted with and without drug metabolism term, and the results are shown in Fig. 6.12. Fig. 6.12(a) displays the NSC curves for each parameter of the proposed model that accounts for the effects of drug metabolism, whereas Fig. 6.12(b) displays the NSC curves for the model in which drug metabolism term is neglected. From the figures, one can observe that qualitatively patterns are similar in both the cases. The NSC

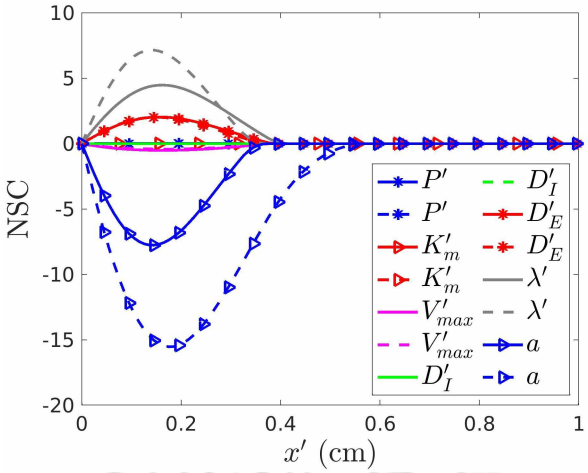

Figure 6.11: Sensitivity of the input parameters on the model response with no advection term. The 'solid lines' display the results for 10% increase in the nominal values while the 'dashed lines' show the results for 10% reduction.

values are found to be positive for the parameters u'_0, D'_I, and K'_m (Fig. 6.12(a)). This implies that on an increase in the mentioned parameter value, the drug concentration also increases. The negative NSC values for V'_{max} reflect the negative change in drug concentration due to the further loss in drug on an increase in drug metabolism rate.

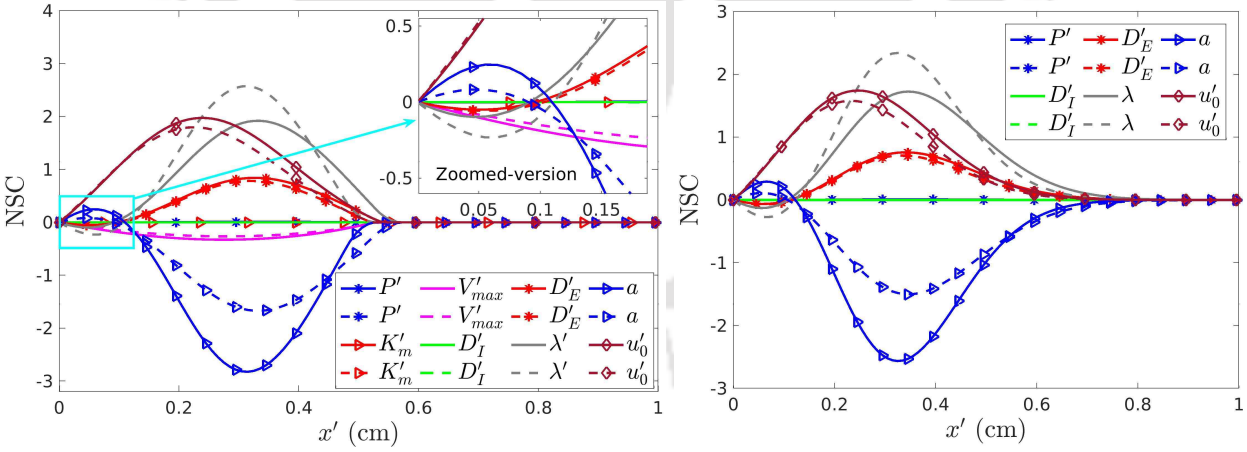

(a) (b)

Figure 6.12: Sensitivity of the input parameters on the model response measured as the NSC values. (a) Results are depicted for the full proposed model and (b) results for the model with no drug metabolism term. The inset in (a) shows the zoomed-version of the results in rectangular box. The 'solid lines' display the results for the 10% increase in the nominal values while the 'dashed lines' show the results for 10% reduction.

For the parameters, D'_E, λ', and P', the NSC values change the sign from negative to positive as one traverse in the spatial domain, while for a (the radius of the cell), the NSC value changes from positive to negative (Fig. 6.12). The results clearly show that the positive change in a parameter may cause a negative as well as a positive change in solute concentration. The sign change of the NSC value for a parameter is the effect of advection. However, the variations near the inlet are smaller than the central ones.

The findings of sensitivity near the inlet can be explained as follows. The NSC value on a positive change in D'_E is negative due to the decrease in drug concentration that takes place due to larger diffusion. For the parameter P', the penetration increases with an increase in the parameter value. However, near the inlet, the NSC value is negative owing to decrease in drug concentration on increasing P'. The behaviour of the results on change in P' is similar to that of D'_E. The sensitivity nature for a and λ' are opposite as these parameters contribute in accounting the extracellular spacial volume in the model. In the case of the prior one (a), the extracellular spacial volume increases on increasing the parameter value, while for the latter one (λ'), extracellular volume decreases on the increase in parameter value.

The sensitivity of the parameters decreases in the order as a, λ', u'_0, D'_E, V'_{max}, P', D'_I, and K'_m. The NSC curves diminish to zero $x' = 0.55$ onwards as the drug concentration decays to zero (Fig. 6.12(a)). However, in Fig. 6.12(b), this is true for $x' = 0.7$ onwards due to the larger drug penetration in absence of drug metabolism. Inspections clearly reveal that the cell size and microscale domain size show larger deviations according to the sensitivity analysis, as these parameters majorly contribute to assimilate the main medium, the extracellular space, for drug transport. In fact, fluid velocity shows the visible effects on model response as it has a direct effect of drug penetration. The parameters P' and D'_I are least sensitive to the model outcome as these incorporate the transport across the intracellular space, contributing much less in drug penetration due to the restrictive cell membrane permeability.

6.6 Conclusions

In this chapter, the FVHMM-p is extended to include the effects of fluid flow and drug metabolism on the penetration and distribution efficacy of a drug in tissues. In the model, fluid flow and drug metabolism are incorporated at the continuum scale, whereas the diffusion phenomenon is assimilated through macro-micro coupling based on the FVHMM-p (Chapter 4). By treating the

tissue as a porous medium, Darcy's law is used for fluid flow, and the drug metabolism is calculated using the Michaelis-Menten equation. The bounded upwind scheme namely SUPERBEE is used to discretize the advection part of the model as the sharp gradient in concentration may result in oscillations with unbounded schemes, particularly when the advection dominates over the diffusion, which is the case in the transport of larger size drug particles in drug delivery. The model is validated with the experimental results.

The model is simulated to understand the effects of drug particle size, cellular geometry, and cell membrane permeability on drug penetration and distribution efficacy in tissues. The effects of metabolism on drug penetration are also analysed. This study of drug penetration and distribution leads to the following findings.

1. The effects of drug particle size are noticeable in the penetration and distribution of a drug. Smaller size particles can penetrate deeper.

2. Larger size particles can penetrate in fluid flow regions of a tissue (i.e., with advection); however, where fluid flow is negligible, such particles may accumulate around the capillary.

3. Smaller size particles are viable to take the advantage of available pores in the extracellular space of tissues.

4. Cell height affects the penetration of smaller size particles ($\approx$ 1 nm), whereas, the larger size particles ($\approx$ 100 nm) show very less effects. The effects decrease as the particle size increases. In other words, cell geometry can affect the penetration of drug particles of size 1 nm.

5. Cell width does not affect the penetration of drug particles.

6. In the fluid flow regions of tissue, drug metabolism may not affect the penetration and distribution of a drug; the results are similar to those without drug metabolism. However, in the absence of advection, penetration distances may get reduced significantly, depending on the intensity of drug metabolism.

7. In the fluid flow regions, cell membrane permeability does not affect the penetration and distribution of a drug.

Furthermore, this work is comprehended with the sensitivity analysis of the proposed model. It is found that the drug concentration is sensitive to the parameters, fluid velocity, microscale domain cell size, extracellular fluid diffusivity. Note that these parameters model the processes related to the extracellular space, which is the main medium of drug transport. The model is least sensitive to the parameters that are related to the transport processes across the intracellular space, such as the cell membrane permeability and intracellular diffusivity.

भारतीय प्रौद्योगिकी संस्थान गुवाहाटी
Indian Institute of Technology Guwahati

CHAPTER 7

PENETRATION AND DISTRIBUTION OF CHEMOTHERAPEUTICS

Chemotherapeutic agents are widely used for controlling tumour growth and limiting proliferation. Over the years, many chemotherapeutic drugs have shown significant anticancer activities during the clinical trials. These drugs are used either alone or combined with the other drugs or treatments. Treatment with chemotherapeutics usually needs a balance between the desired effects and the adverse effects associated with drug accumulation in normal tissues and other organs. Though several drugs are available for treatment, their efficacy is limited in practice. This may be due to the inefficient delivery of chemotherapeutics to the lesion site.

The penetration of prominent chemotherapeutic drugs into tumour tissues is not well investigated in the literature. So, the questions remain, which drug penetrates better and what are their relative penetration depths. As in an organism, biophysical processes change with location and also with time, it is circumvented to understand how the variations in transport processes, such as fluid velocity and drug elimination rate, affect the penetration of chemotherapeutic drugs into tumour. In this chapter the multiscale algorithm developed in Chapter 6 is employed on chemotherapeutic drugs. The model incorporates the drug transport due to diffusion, advection, and embodied with the drug elimination due to enzymatic/non-enzymatic reactions. The effects of cellular microscopic structure on the penetration of several prominent chemotherapeutic drugs are investigated. The chemotherapeutic drugs selected for this study are fluorouracil (FU), carmustine (BCNU), cisplatin (CIS), methotrexate (MTX), doxorubicin (DOX), and paclitaxel (PTX).

7.1 Model formulation

The model used in this chapter is similar to the one developed in Chapter 6. The two-dimensional cross-section of a tissue domain ($\Omega'(\subset \mathbb{R}^2)$) is considered as shown in the Fig. 6.1. The dimensional mass-transport model considered in this chapter is given in Section 6.1 with $S' = -k'_e C'$. The dimensionless macroscale model can be written as,

$$\frac{\partial C(t,x,y)}{\partial t} + \nabla \cdot (\mathbf{v}C) = \nabla \cdot \mathbf{F} + S, \quad (t,x,y) \in (0,\tau] \times \Omega, \tag{7.1}$$

with the initial condition

$$C(0,x,y) = C_0(x,y), \quad (x,y) \in \Omega. \tag{7.2}$$

The drug elimination term $S = -k_e C$, where $k_e = k'_e \tilde{L}/\tilde{U}$ for its dimensional variant k'_e, the elimination rate of drug due to the degradation/metabolism. The schematic diagram of the problem is shown in Fig. 6.1. The solution procedure is the same as discussed in Chapter 6.

7.2 Results and discussion

The penetration and distribution of chemotherapeutic drugs, such as FU, BCNU, CIS, MTX, DOX, and PTX, are studied by considering various physiological situations in tissues. These drugs are selected due to their potency of treatment and the availability of physical parameters in the literature. The analyses are performed with and without advection owing to the varying rate of fluid flow in the living organisms, and the effects of drug elimination on the penetration of the given chemotherapeutic drugs are determined. The impact of microscopic cellular structure of different shapes on the penetration of chemotherapeutic agents in tissues is examined.

The parameters related to the selected chemotherapeutics are shown in the Table 7.1 [72]. Generally, fluid velocity in tissues varies in the range 0–0.72 cm/h with the average value 0.216 ± 0.072 cm/h [9]. The higher velocity of fluid can be seen near the vascular regions, whereas the lower or negligible velocity of fluid is away from the blood vessels. This work does not focus on the transport across the vessels and nearby interstitium. So, the velocity is chosen in the range 0–0.06 cm/h. The transport across the cell membrane becomes very less due to the low permeability of the membrane, $P' = 0$ is considered in this chapter. The microscale domain edge length is set to 10^{-3} cm, and a circular cell (default shape) of radius 4.1×10^{-4} cm is placed at the centre of it. If not prescribed explicitly, the drug penetration study

is performed for $(t' =)5$ h. With these selected parameters, the obtained results are uniform along the y'-direction; hence, the results are presented for the x'-direction only.

Table 7.1: Values of the parameters for chemotherapeutic drugs.

Parameter	FU	BCNU	CIS	MTX	DOX	PTX
D'_E (cm^2/h)	4.32×10^{-2}	5.4×10^{-2}	9×10^{-3}	1.9×10^{-2}	1.23×10^{-2}	3.24×10^{-2}
k'_e (1/h)	2.016	0.396	2.628	0.54	2.088	2.45×10^{-3}

An organism is heterogeneously complex, as a result, the dominating role of mass transport processes vary across different tissues. In order to get insights into the relative importance of transport processes and their effects on drug penetration, the following dimensionless parameters are used.

Peclet number (Pe) that compares the role of advection versus diffusion in the transport of drug is defined as,

$$\text{Pe} = \frac{\tilde{L}u'_0}{D'_E}. \tag{7.3}$$

Thiele modulus (Th) number is used to understand the relative importance of diffusion to the elimination rate, and it is defined as,

$$\text{Th} = \tilde{L}\sqrt{\frac{k'_e}{D'_E}}. \tag{7.4}$$

As the elimination rate in the transport pathway is high for several drugs, it is empirical to know how much drug is available to transport for cytotoxicity at the lesion site. The Karlovitz number (Ka) is used to examine the drug availability for advective transport in the tissue. The number is defined as,

$$\text{Ka} = \frac{u'_0}{\tilde{L}k'_e}. \tag{7.5}$$

The above numbers (Th and Ka) mainly measure the relative effects of individual transport processes. However, it can be noticed that the elimination degrades or removes the drug, in other words, it contributes in the decrement of drug penetration. Whereas, the diffusion and advection transport the drug into the tissue. Therefore, in this chapter, a novel dimensionless number (KT) is introduced to measure the relative effects of the combined process of diffusion and advection of drug to the process of its elimination as,

$$\text{KT} = \frac{\text{Ka}}{\text{Th}^2}. \tag{7.6}$$

This number is the ratio of time constant of elimination of drug to that of the cumulative transport due to diffusion and advection.

The values for the above dimensionless numbers for each drug are listed in the Table 7.2. For calculation, $u_0' = 0.06$ cm/h and $\tilde{L} = 2$ cm are considered.

Table 7.2: Dimensionless numbers.

Parameter	BCNU	CIS	DOX	FU	MTX	PTX
Th	5.416	34.176	26.122	13.663	10.640	0.550
Ka	0.076	0.011	0.014	0.015	0.056	12.255
Pe	2.22	13.33	9.80	2.78	6.29	3.70
KT	0.00258	0.00001	0.00002	0.00008	0.00049	40.54931

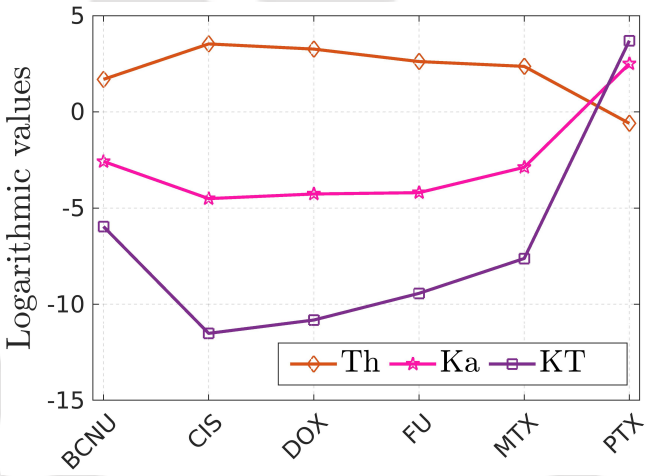

Figure 7.1: Logarithmic plot of the values of the dimensionless numbers.

7.2.1 Validation

The numerical results are validated with the experimental results of Qian et al. [44]. In their article, in vivo experimental results are presented for the penetration of DOX-containing polymer millirods in the ablated rat livers. The transport process was considered to take place due to the diffusion phenomenon only. The estimated effective diffusion coefficient (3.96×10^{-4} cm^2/h) reported in their article is used for validation. As the reported diffusion coefficient is effective, the tissue domain is taken to be cell-free for validation. The model is simulated for

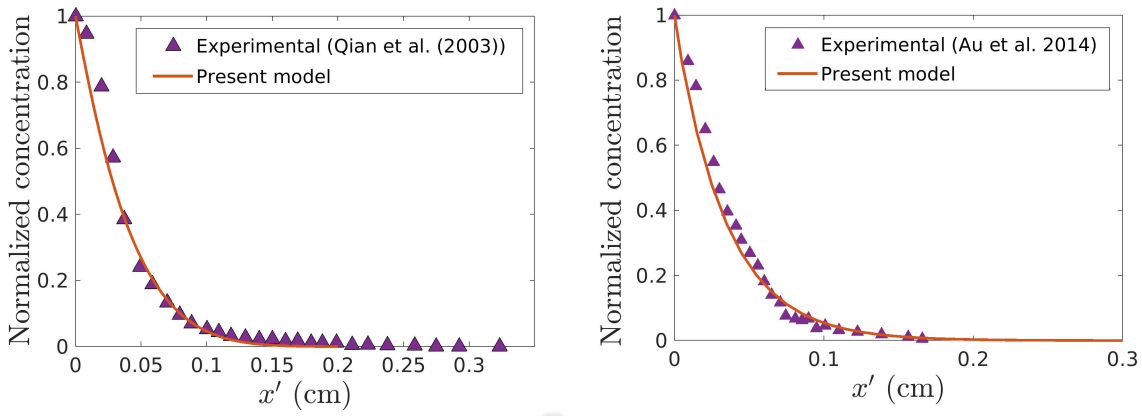

(a) (b)

Figure 7.2: Validation of the present model results with (a) the experimental results of DOX [44] and (b) the experimental results of PTX [5].

$t' = 4$ h, and the results are shown in Fig. 7.2(a). It is evident that both the results are in very good agreement.

Another comparison is made with the experimental results of PTX reported in the article of Au et al. [5]. The parameters are taken as, $D'_E = 8 \times 10^{-3}$ cm^{-2}/h, $k'_e = 2.5$ 1/h, and $u'_0 = 0.01$ cm/h to fit the simulation results with the experimental ones. The results are shown in the Fig. 7.2(b), and it can be observed that the proposed model can successfully capture the experimental concentration distribution qualitatively.

7.2.2 Importance of KT number

In order to investigate the importance of KT number, a new drug (say D) is considered with the parameters as: $u'_0 = 0.0601$ cm/h, $k'_e = 2.016$ 1/h, and $D'_E = 0.02$ cm^2/h. The steady-state results are conducted for FU and D. The relation $\mathrm{Ka_D}(= 0.014906) > \mathrm{Ka_{FU}}(0.014881)$, where subscript denotes the drug, suggests that the drug availability to get advected is higher for drug D as compared to that for the FU. Whereas, $\mathrm{Th_D}(= 20.08) > \mathrm{Th_{FU}}(13.663)$ suggests that elimination is faster for drug D in comparison to that of FU. So, Ka number suggests that D can show better penetration due to the availability of more drug to be advected with fluid flow; but according to the Th number, FU can penetrate deeper due to the lesser elimination factor. So, in this situation, it is inconclusive to determine which drug penetrates deeper. It is because of the fact that the Ka number does not account the diffusion process and the Th number does not consider advection.

This difficulty can be overcome with the novel KT number, which compares the time-scales of drug elimination with that of the cumulative time-scale of advection-diffusion processes. The relation $\mathrm{KT_{FU}}(= 8 \times 10^{-5}) > \mathrm{KT_D}(= 3.697 \times 10^{-5})$ suggests that the elimination is slower for FU or drug transportation takes place faster than the reaction. Hence, FU should penetrate deeper, which is also reflected in the results of the numerical experiments shown in Fig. 7.3. Thus, the KT number is a useful parameter to predict the behaviour of advection-diffusion-reaction processes more precisely.

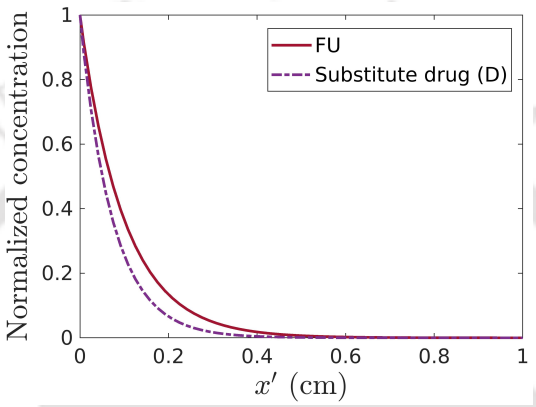

Figure 7.3: Importance of dimensionless parameter KT.

7.2.3 Effects of fluid flow

In some locations of tissues, fluid flow becomes so slow that its effects are neglected many times though fluid flow plays a dominant role to extravasate a drug and other important constituents into the interstitial space. So, it is imperative to understand the effects of fluid flow on the penetration and distribution of chemotherapeutic drugs. In order to identify its effects, numerical experiments are conducted with different inlet fluid velocities as, $u_0' = 0$, 0.01, 0.036, and 0.06 cm/h.

Fig. 7.4 shows the results for each prescribed velocity. The profiles of drug concentrations are shown in Figs. 7.4(a)–(d) while the penetration depths are shown in the Fig. 7.4(e). The penetration depth is measured as the depth from inlet where concentration falls below 1% of the infusion concentration. Clearly, an increase in fluid velocity increases the penetration of each chemotherapeutic drug. On comparison, it can be seen that BCNU penetrates deeper into the tissue, followed by PTX, MTX, FU, DOX, while CIS penetrates least (in the stipulated time 5 h). The order of penetrations of drugs remains unchanged irrespective of fluid velocity.

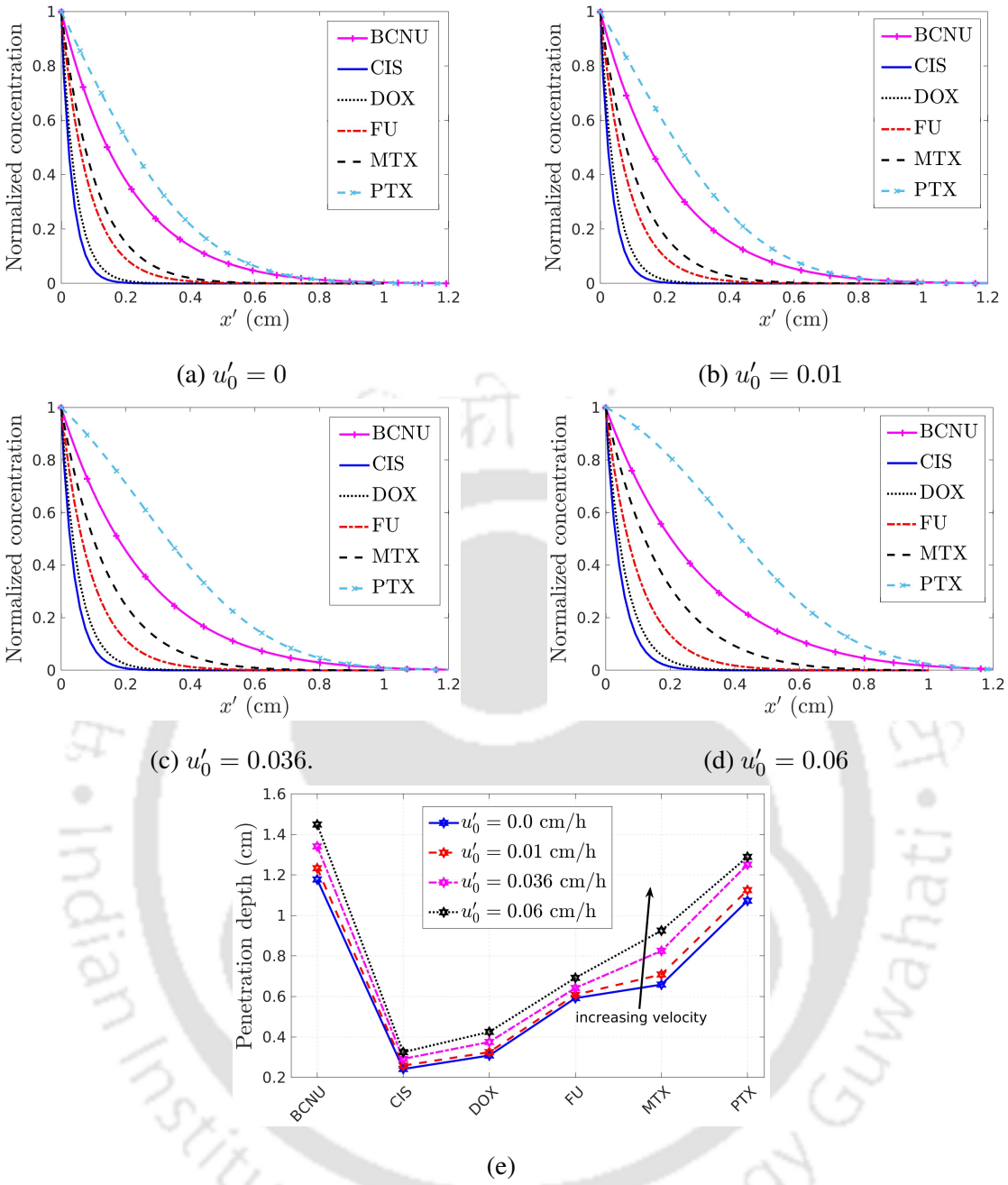

Figure 7.4: Penetration of chemotherapeutic drugs on various fluid velocity. (a) $u_0' = 0$ cm/h, (b) $u_0' = 0.01$ cm/h, (c) $u_0' = 0.036$ cm/h, and (d) $u_0' = 0.06$ cm/h. (e) Penetration depths.

The effects of advection on the concentration of PTX can be seen near the inlet and pertain till the drug reaches zero concentration (Fig. 7.4(d)). This shows that fluid flow affects the distribution of PTX. The drug concentration of PTX is seen to be higher than that of BCNU; however, the penetration depth is greater for BCNU (in the stipulated time 5 h). This is due to the larger diffusion of BCNU. But from steady-state results, it is found that PTX penetrates deeper owing to its lesser elimination rate that makes the higher availability of drug for pene-

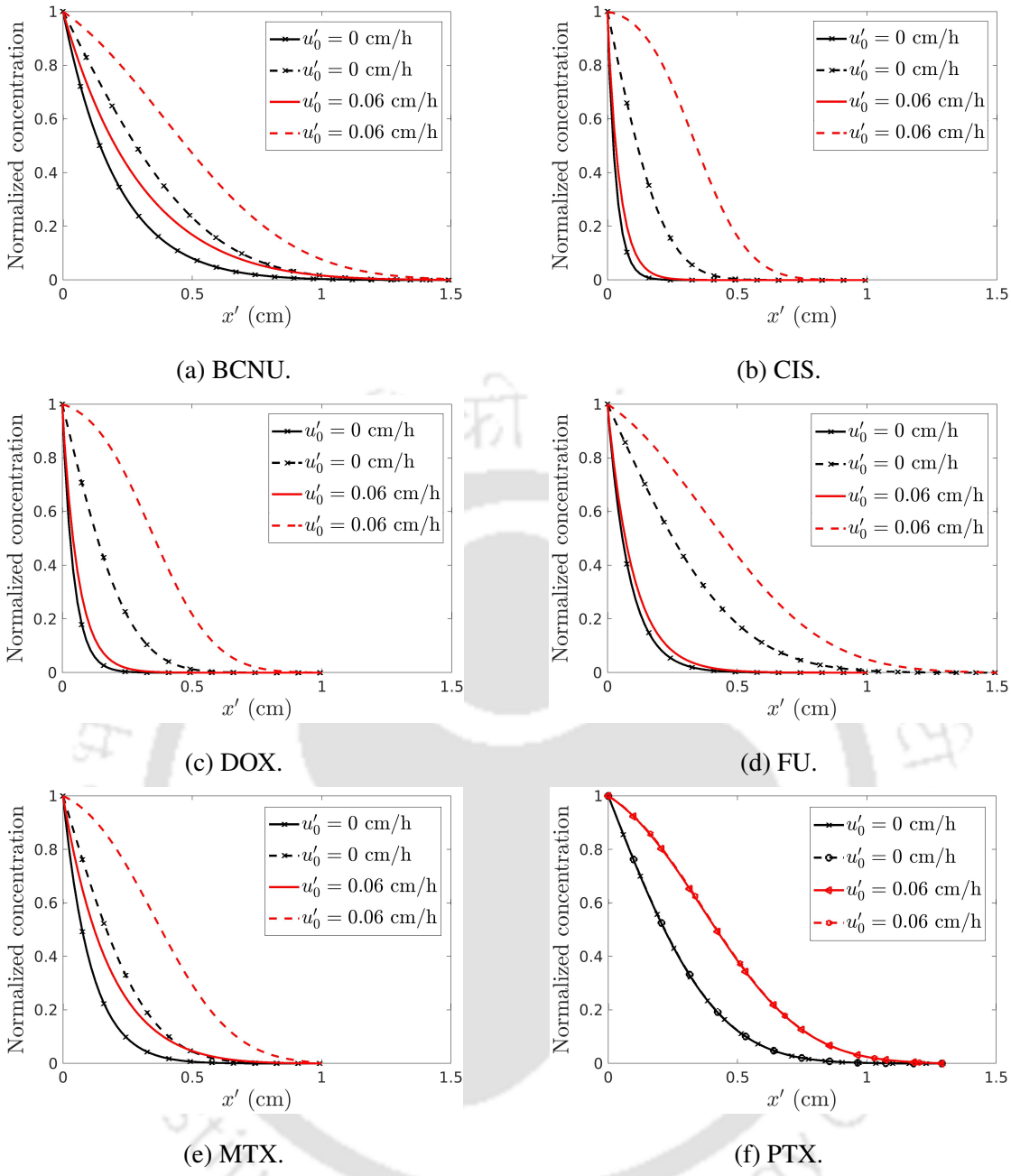

(a) BCNU. (b) CIS.

(c) DOX. (d) FU.

(e) MTX. (f) PTX.

Figure 7.5: Comparison of penetration of chemotherapeutics with and without elimination. Solid lines '–' show the results with elimination while dashed lines '- -' without elimination.

tration, which is reflected by the larger value of KT number.

On comparing penetration depths of FU and MTX (Fig. 7.4(e)), it can be seen that the penetrations are almost same under no flow condition. However, with the increase in fluid velocity, the penetration of MTX increases higher than of the FU. This can be explained by the dimensionless number Ka that has greater value for MTX, showing the dominant effects of advection. The lower value of Ka for FU shows the dominating elimination effects, which

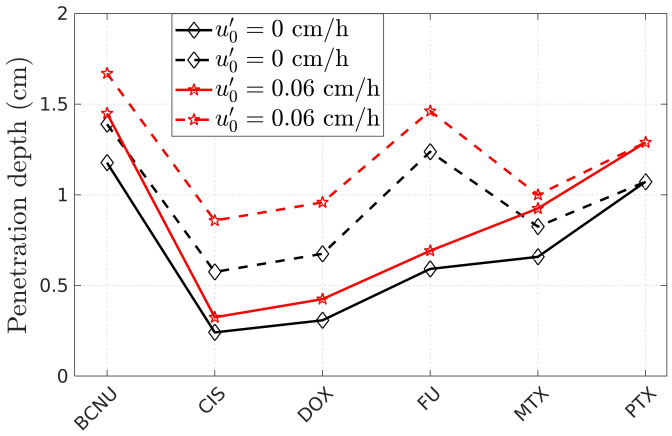

Figure 7.6: Penetration depths of drugs with and without advection. Solid lines '–' show the results with elimination while dashed lines '- -' without elimination.

inhibits the penetration. Though the diffusivity of FU is more than that of the MTX and PTX, it shows lesser penetration owing to the higher elimination rate. This can be easily explained by the KT number which has smaller value for FU than for the MTX and PTX. So, the effects of elimination are more dominating for FU than for the latter drugs.

On comparing dimensionless parameters for CIS and DOX (Table 7.2), some intriguing facts are observed. Note that the relation $\mathrm{Pe}_{\mathrm{CIS}} > \mathrm{Pe}_{\mathrm{DOX}}$ shows that the advection plays a more important role in the transportation of CIS; however, it penetrates less. This behaviour is due to the reaction process, which is not accounted by the Pe number. On comparing the time-scale of reaction process to that of the combined transport process due to diffusion and advection (using the KT number), it is confirmed that DOX should penetrate deeper, which is also reflected from the numerical experiments (Fig. 7.4). Hence, KT is far more efficient for the comparison of advection-diffusion-reaction processes.

The poor penetration of DOX is consistent with the findings of Tunggal et al. [59], where they studied the penetration in an in vitro model. Also, the better penetration of FU compared to that of the DOX is consistent with their findings.

7.2.4 Effects of drug elimination rate

Drug elimination takes place mainly in two ways: (i) direct removal of administered drug in its original form and (ii) elimination after metabolic bio-transformation [16]. Several factors, such as drug properties, genetic variation among the individuals, and pathways of drug transportation in the body, impact the elimination of a drug [16]. So, drug elimination rate can vary across

the tissues and also individuals. Numerical experiments are carried out in this part to better understand the impacts of drug elimination on penetration and distribution of chemotherapeutic drugs. The experiments are conducted with a fluid flow ($u_0' = 0.06$ cm/h) and without a fluid flow.

Results for each of the chemotherapeutics are shown in Fig. 7.5. Clearly, there is a large variation in the effects of drug elimination across the drugs. PTX shows no effect of elimination on its penetration owing to the lower elimination rate, which provides a favourable condition for deeper penetration. The largest values of Th and Ka demonstrate the availability of PTX for diffusion and advection in the tissue; in other words, lesser elimination rate. Also, the KT number confirms that the elimination effects are least for this drug. So, there is another situation where KT number can easily explain the outcomes of the processes.

The other chemotherapeutic drugs (excluding PTX) considered in this chapter show significant effects of elimination on their penetration. It is evident that due to elimination, drug penetrations reduce significantly. FU and BCNU show the penetration beyond 1 cm in absence of elimination; whereas, the penetrations of other drugs does not exceed 1 cm in the stipulated time. CIS and DOX penetrate least with elimination.

The penetration depths are plotted in Fig. 7.6. Note that the penetration depths are greater in the case of "no elimination." Penetration increases significantly for FU, DOX, and CIS. So, the results explain that the penetration can be improved (increased) significantly if one can potentially reduce the elimination rate of a drug, which can be achieved by suitable formulations.

7.2.5 Effects of cell geometry

Drug transport is greatly affected by the presence of cells and other large molecules in the tissue domain. In other words, cells are the key determinant of drug distribution across the tissue and in an organism. The intra- and extra-cellular activities are controlled by the cell owing to their growth, division and death, and these processes lead to changes in morphogenesis [41]. Cells can achieve different shapes, such as elongated, spherical, round, and spindle shape [7]. Thus, the microscopic structure of the tissue is mainly determined by the cellular geometry.

Numerical experiments are conducted to understand the effects of cell geometry on chemotherapeutic penetration. The conducted numerical experiments are of three types. In the first-type experiment, the cell volume is kept fixed and the cell parameters (a_1, a_2) are varied to achieve different shapes. In the second-type experiment, the cell height is varied while keeping the cell

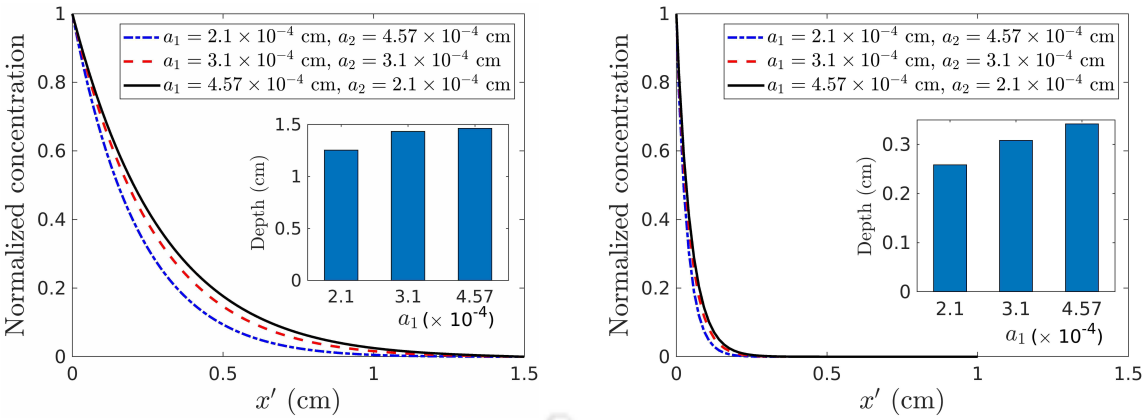

(a) BCNU.

(b) CIS.

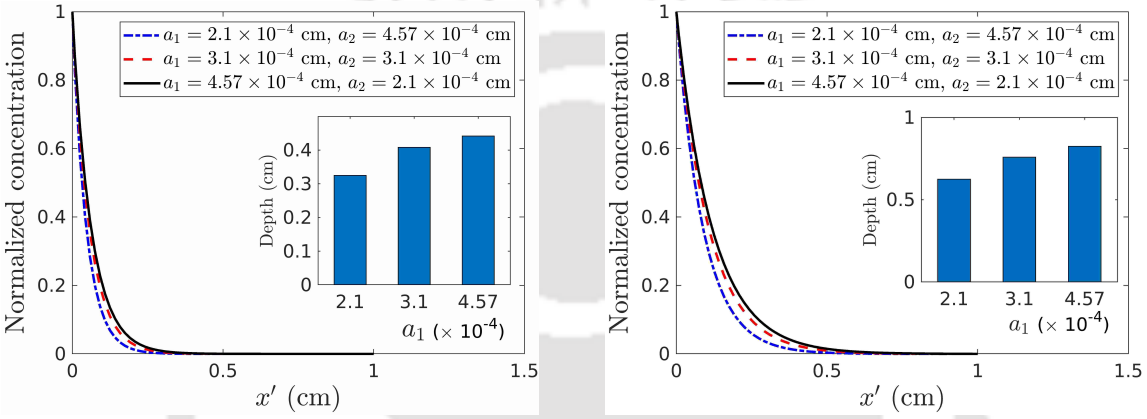

(c) DOX.

(d) FU.

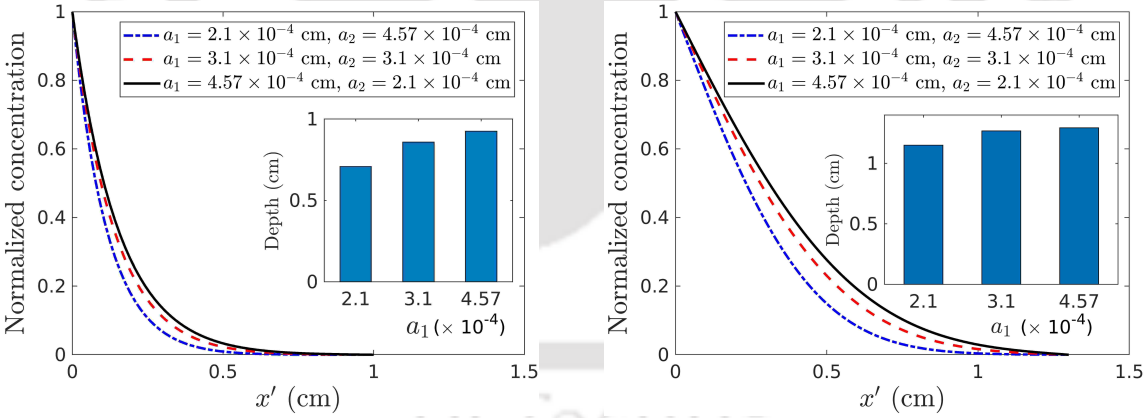

(e) MTX.

(f) PTX.

Figure 7.7: Effects of cell geometry on drug penetration ($u_0' = 0$ cm/h).

width fixed. In the last experiment (third-type), the cell width is varied while the height is kept unchanged. Results are analysed with and without fluid flow.

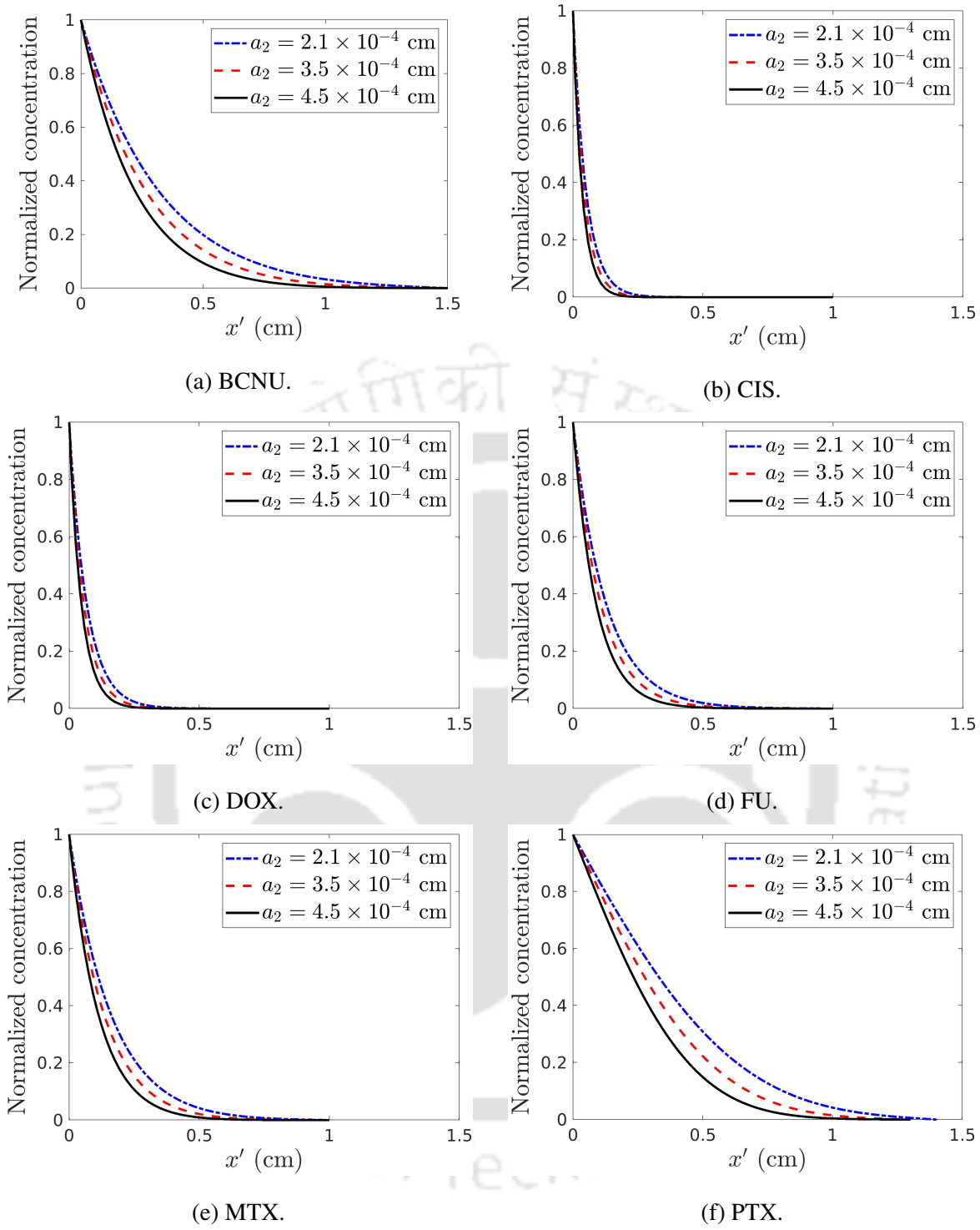

(a) BCNU. (b) CIS.

(c) DOX. (d) FU.

(e) MTX. (f) PTX.

Figure 7.8: Effects of cell height on drug penetration ($u_0' = 0$ cm/h, $a_1 = 2.1 \times 10^{-4}$ cm).

Effects under no flow condition

For the first-type experiment, the cell parameters are selected as, $a_1 = 2.1 \times 10^{-4}$ cm and $a_2 = 4.57 \times 10^{-4}$ cm, $a_1 = 3.1 \times 10^{-4}$ cm and $a_2 = 3.1 \times 10^{-4}$ cm, and $a_1 = 4.57 \times 10^{-4}$ cm and $a_2 = 2.1 \times 10^{-4}$ cm. Note that as the cell occupy the same area, the extracellular volume

of tissue domain does not change; however, the microscopic structure of tissue is different for each choice of the cell. The first choice of a_i's leads to an elliptical cell whose semi-major axis lies along the y'-direction, second one leads to a circular shape while the last one leads to an elliptical cell with semi-major axis along the x'-direction. Fig. 7.7 shows the results on penetration and distribution of chemotherapeutics under no flow condition (i.e., $u_0' = 0$ cm/h). The penetration depths are shown in the insets of respective figures. It can be seen that the drug penetrations are significantly different for different choices (or geometry) of cells and decreases as the semi-major axis along the y'- direction decreases. Even though the extracellular volume does not change but the choice of cell geometry affects the penetration of drug. Thus, the microscopic structure of tissue has an impact on penetration of chemotherapeutic drugs.

For the second type experiment, the cell heights are chosen as, $a_2 = 2.1 \times 10^{-4}$ cm, 3.5×10^{-4} cm, and 4.5×10^{-4} cm and keeping the cell width fixed ($a_1 = 2.1 \times 10^{-4}$ cm). Fig. 7.8 shows the effects of cell height on penetration of chemotherapeutic drugs. Here, one can observe that the penetration decreases significantly on increasing the cell height for each chemotherapeutic drug. This is due to the more obstruction of drug transport on an increase in cell height as the drug penetrates towards the right boundary from the left one (see Fig. 6.1).

In the last one, the experiments are conducted by varying the cell width (as $a_1 = 2.1 \times 10^{-4}$ cm, 3.5×10^{-4} cm, and 4.5×10^{-4} cm) while keeping the cell height fixed ($a_2 = 2.1 \times 10^{-4}$ cm). Fig. 7.9 shows the effects of cell width on penetration and distribution of chemotherapeutic drugs. One can observe that the drug penetration does not get affected much due to a change in the cell width. Note that the drug transport takes place from left to the right direction (see Fig. 6.1); the clear passage for drug does not get disturbed on varying cell width (see Fig. 3.7(d)); hence, the drug penetration is not affected by the cell width.

Effects with fluid flow

Fig. 7.11 shows the effects of cell geometry (first-type experiment) on penetration and distribution efficacy of chemotherapeutic drugs with the inlet fluid velocity ($u_0' = 0.06$ cm/h). Nevertheless, the observations are similar to the case of without fluid flow. The effects of cell height and cell width are also studied; however, the results are similar to the situations as seen in the case of no flow.

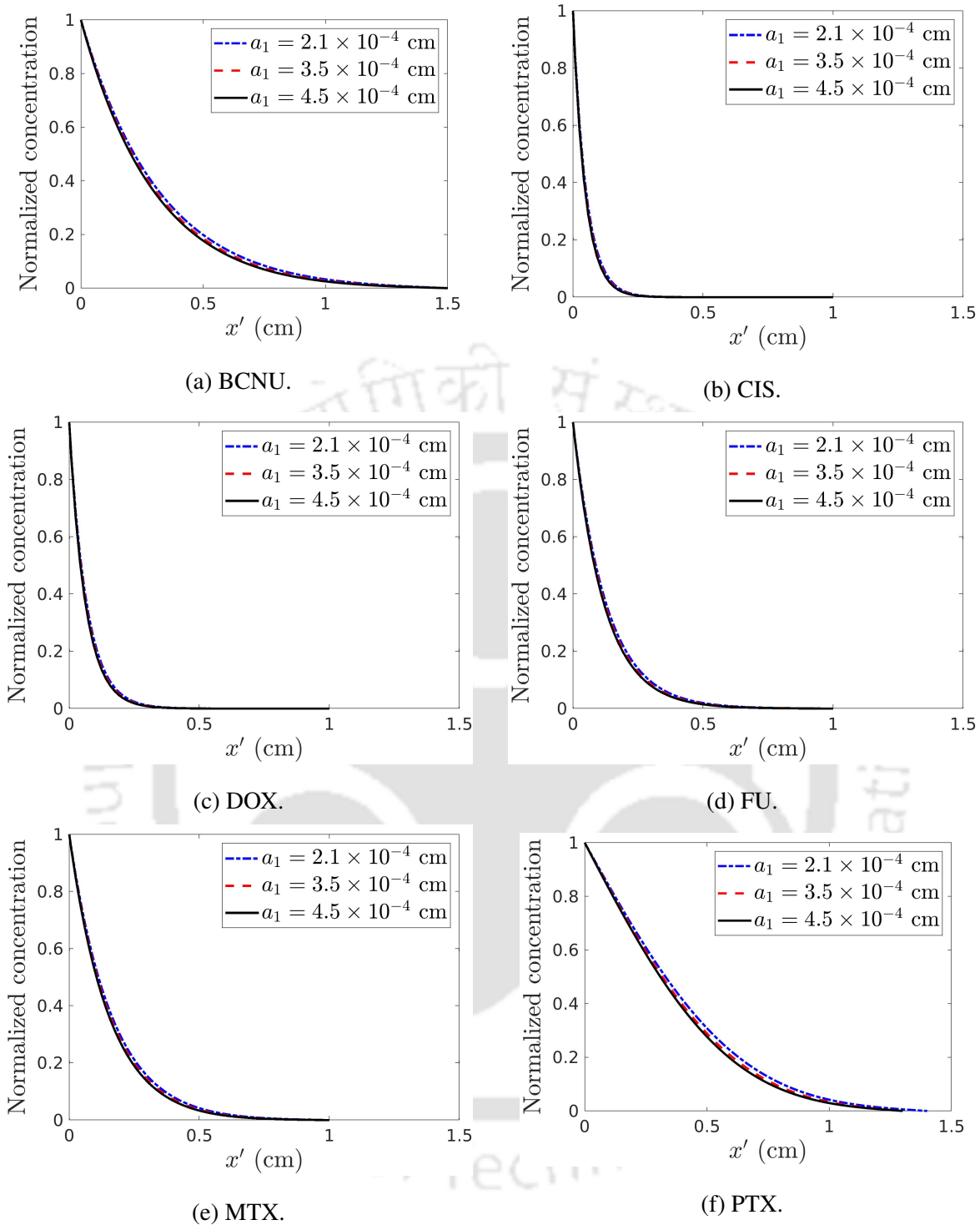

(a) BCNU. (b) CIS.

(c) DOX. (d) FU.

(e) MTX. (f) PTX.

Figure 7.9: Effects of cell width on drug penetration ($u_0' = 0$ cm/h, $a_2 = 2.1 \times 10^{-4}$ cm).

7.3 Conclusions

In this chapter, the penetration and distribution of chemotherapeutic drugs, such as carmustine (BCNU), cisplatin (CIS), doxorubicin (DOX), fluorouracil (FU), methotrexate (MTX), and paclitaxel (PTX), are studied. The model incorporates the multiscale features of the tissue us-

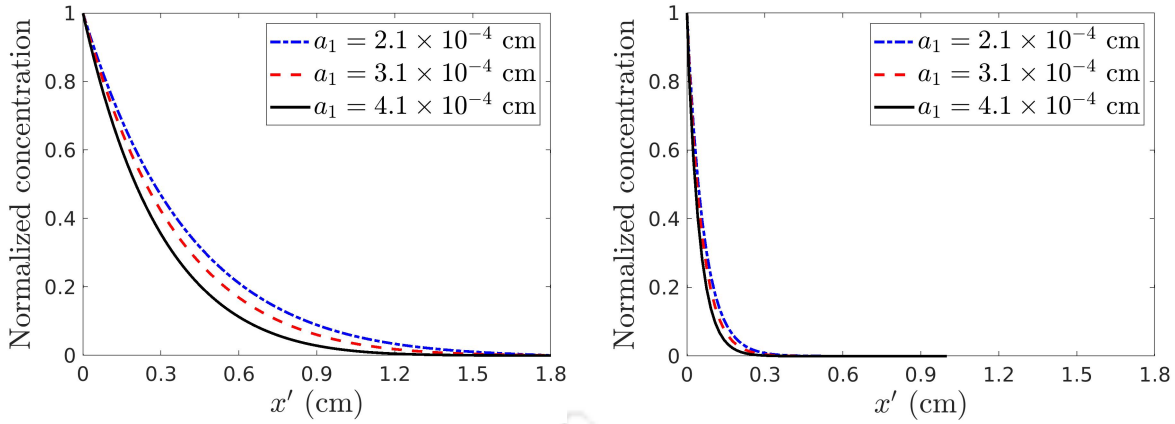

(a) BCNU.

(b) CIS.

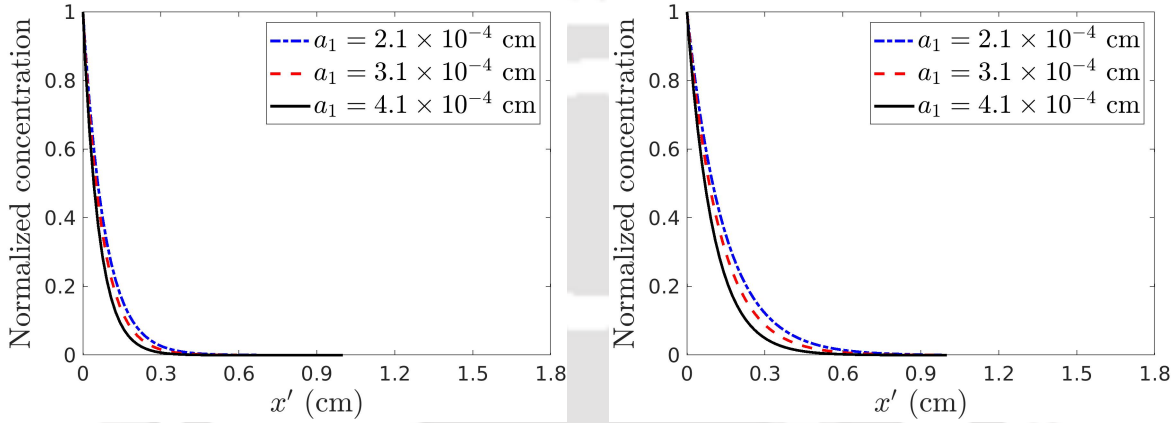

(c) DOX.

(d) FU.

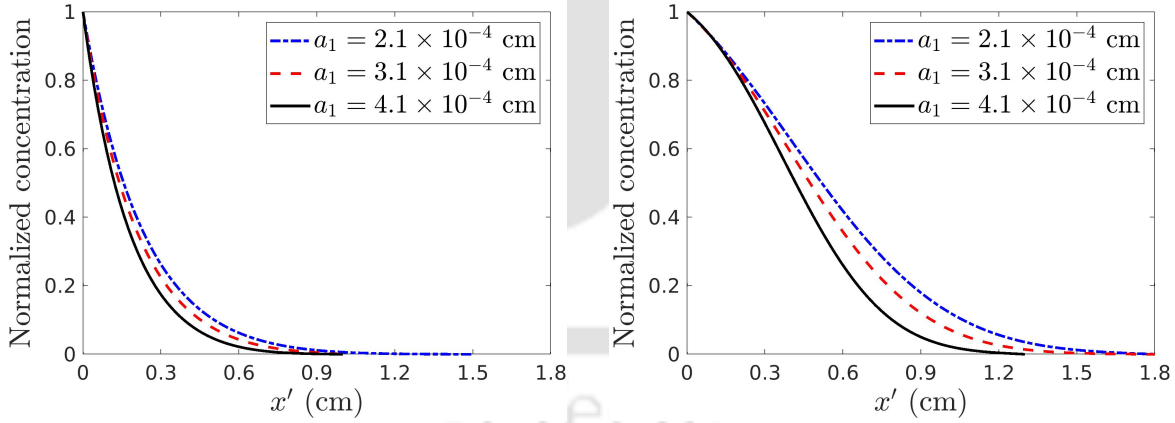

(e) MTX.

(f) PTX.

Figure 7.10: Effects of cell size on drug penetration ($u_0' = 0.06$ cm/h).

ing the finite volume heterogeneous multiscale method, where drug diffusivity is accounted through the macro-micro coupling, and the advection and elimination of a drug are included on the macroscale. The macro-micro coupling assimilates the transport around the cell; as a result, the drug concentration at the tissue scale resolves the microscopic effects. The numerical

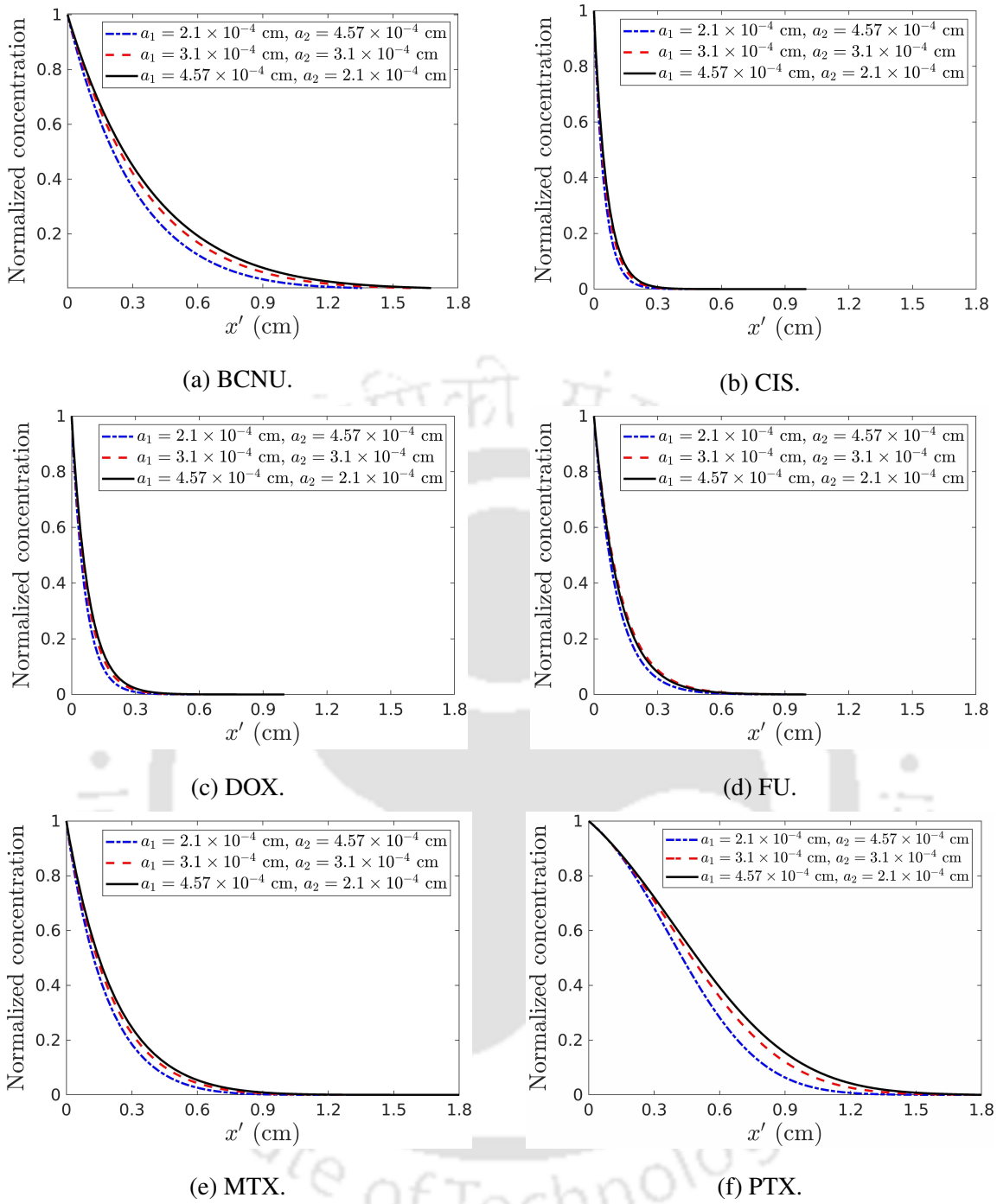

(a) BCNU. (b) CIS.

(c) DOX. (d) FU.

(e) MTX. (f) PTX.

Figure 7.11: Effects of cell geometry on drug penetration ($u_0' = 0.06$ cm/h).

results of the proposed model are in very good agreements with the experimental results.

A novel dimensionless number KT $= \frac{\text{Ka}}{\text{Th}^2}$ is introduced, where Ka and Th are Karlovitz and Thiele modulus numbers, respectively. It can be read as the ratio of time-scale of reaction rate to the cumulative time-scale of advection and diffusion processes. More precisely, it is a relationship between the elimination process (that decreases the penetration of a drug owing to either degradation or direct removal from the tissue) and drug transport due to the combined

effects of diffusion and advection. This parameter (KT) is useful to explain the results obtained due to the advection-diffusion-reaction processes.

It is found that BCNU penetrates maximum into the tissue, followed by PTX, MTX, FU, DOX, while CIS penetrates the least in the stipulated time 5 hours. However, on steady-state simulation, PTX penetrates deeper followed by BCNU and the order remains the same for other drugs. It is observed that the advection affects drug penetration. An increase in fluid velocity can increase the drug penetration. It is also noticed that the penetration of most of the chemotherapeutic drugs can be increased significantly on reducing the effects of elimination. Whereas, PTX shows negligible effects of elimination on its penetration owing to its lower elimination rate, which also makes it possible to penetrate deeper into the tissues.

From the numerical experiments, it is studied for the first time that the cell shape can affect the penetration of a chemotherapeutic drug. The experiment showed that the cell height has significant effects on penetration of chemotherapeutic drugs. However, the results obtained by varying the cell width showed very less effects on the penetration of chemotherapeutic drugs.

भारतीय प्रौद्योगिकी संस्थान गुवाहाटी
Indian Institute of Technology Guwahati

CHAPTER 8

CONCLUSIONS AND FUTURE SCOPE

8.1 Conclusions

Until now, single scale continuum models have mostly been used to model biological systems; however, these models do not accurately imitate the complex biochemical and biophysical processes that involve multiple scales. As a result, multiscale models with the ability to resolve different scales in the study at a particular level are in great demand.

In this thesis, a novel finite volume heterogeneous multiscale method (FV-HMM) is developed to study drug delivery in biological tissues. The FV-HMM is propounded in the framework of heterogeneous multiscale method (HMM), and it includes diffusion and partition phenomena as the first objective (Chapter 2). The model includes cell heterogeneity into the tissue scale investigation using a novel macro-micro coupling. In the thesis, the FV-HMM is improved continuously at several stages to incorporate the drug transport processes and employed to investigate the effects of various parameters such as drug particle size, cell geometry, cell membrane permeability, and the cell orientation on drug delivery. The effects of fluid flow and drug elimination on drug penetration and distribution into biological tissues are also studied. The FV-HMM is improved to the FVHMM-p that incorporates the passive diffusion of a drug across the cell membrane (Chapter 4). In the Chapter 5, the FVHMM-p is reconstructed to accurately simulate the effects of (elliptical) cell orientation on penetration and distribution of a drug in the tissue domain. Finally, advection and drug metabolism are incorporated in the drug transport model, and accordingly, the FVHMM-p is extended in Chapter 6. The model is simulated to study the penetration and distribution of several prominent chemotherapeutic

drugs in the tissue (in Chapter 7).

The following key findings are observed through the numerical investigations using the proposed models.

- The effects of drug particle size are prominent in drug delivery, and it is noticed that the smaller size particles penetrate deeper. Larger size particles can penetrate the tissue in fluid flow regions; however, in absence of advection, such particles may accumulate around the capillary.
- The partition coefficient of a drug can affect its penetration.
- Numerical investigations reveal that the solute permeability across the cell membrane affects drug penetration and distribution in tissues. The increase in permeability increases the penetration.
- The experiments conducted with different configurations of cell shape reveal that the drug penetration strongly depends on the microscopic structure of the tissue. It has been observed that despite the cell volume being kept fixed, drug penetration can be different owing to the cell geometry.
- The effects of cell orientation on penetration and distribution of drug in the biological tissues are investigated for the first time. It is observed that the orientation of cell is a prominent factor that can affect the penetration and distribution of drug in tissues significantly.
- It is found that the drug penetration can be affected by the fluid velocity. An increase in fluid velocity increases the penetration.
- On reducing the elimination rate, one may increase the penetration of a drug.
- Finally, the penetration and distribution of chemotherapeutic drugs, such as carmustine, cisplatin, doxorubicin, fluorouracil, methotrexate and paclitaxel, are studied. On comparison, it is found that carmustine penetrates deeper into the tissue, followed by paclitaxel, methotrexate, fluorouracil, doxorubicin, while cisplatin penetrates least.
- Paclitaxel shows negligible effects of elimination on its penetration owing to lower elimination rate, which also makes it possible to penetrate deeper into the tissues as compared to its peers.

From the findings of this thesis, it can be concluded that the penetration of a chemotherapeutic drug is strongly related to its diffusivity and elimination rate, which may hamper the desired concentration at the lesion site. Consequently, the treatment may get affected, and additionally, the chemotherapeutic drug may impact the healthy cells. The experiments on cell geometry shows that the tissue microenvironment can affect the drug delivery as well.

Furthermore, this work is comprehended with the sensitivity analysis of the proposed model to determine the dependency of the model response on the input parameters. It is found that the drug concentration is most sensitive to the parameters such as: fluid velocity, microscale domain size, and extracellular fluid diffusivity. Note that these parameters model the processes related to the extracellular space, which is the main medium of drug transport. The model is least sensitive to the parameters, such as the cell membrane permeability and intracellular diffusivity, which are related to the transport processes across the intracellular space.

The proposed model would be useful to identify the optimal strategies for drug penetration and distribution in the tissues. It may help the experimentalists to choose suitable in vitro models for drug testing.

8.2 Future scope

The proposed model can be used as the base model for future investigations, and further development could be potentially useful in drug delivery. The outcomes of the proposed models will undoubtedly aid in the evolution of future models by introducing more biological complexities and different modes of drug administration depending on how closely the objectives of the drug release phenomena adhere to the real situation. The model may be of interest for the application of drug delivery into different parts of an organism and personalized treatment.

The present study does not deal with the drug deactivation and immune clearance that can affect the nanoparticle penetration and distribution. This model does not also account for the effects arising from the surface charge of the nanoparticles. However, in the biological fluid, nanoparticles' interactions with biomolecules can form biocorona [48]; consequently, nanoparticles properties like shape, size, and surface charge can be altered. Further modification in the proposed model to include drug deactivation, immune clearance, and biocorona formation on nanoparticle surface will allow to have a more clear insight of drug penetration and distribution.

भारतीय प्रौद्योगिकी संस्थान गुवाहाटी
Indian Institute of Technology Guwahati

BIBLIOGRAPHY

[1] Assyr Abdulle and E Weinan. Finite difference heterogeneous multi-scale method for homogenization problems. *Journal of Computational Physics*, 191(1):18–39, 2003.

[2] Assyr Abdulle, E Weinan, Björn Engquist, and Eric Vanden-Eijnden. The heterogeneous multiscale method. *Acta Numerica*, 21:1–87, 2012.

[3] Farida B. Ahmad and Robert N. Anderson. The Leading Causes of Death in the US for 2020. *JAMA*, 325(18):1829–1830, 2021.

[4] Davide Ambrosi, Pasquale Ciarletta, Elena Danesi, Carlo de Falco, Matteo Taffetani, and Paolo Zunino. A multiscale modeling approach to transport of nano-constructs in biological tissues. In *Multiscale Models in Mechano and Tumor Biology*, pages 109–138. Springer International Publishing, 2017.

[5] Jessie L-S Au, Peng Guo, Yue Gao, Ze Lu, Michael G Wientjes, Max Tsai, and M Guillaume Wientjes. Multiscale tumor spatiokinetic model for intraperitoneal therapy. *The AAPS journal*, 16(3):424–439, 2014.

[6] Angelika Batta, Bhupinder Singh Kalra, and Raj Khirasaria. Trends in FDA drug approvals over last 2 decades: An observational study. *Journal of Family Medicine and Primary Care*, 9(1):105–114, 2020.

[7] Jean-Michel Bourget, Maxime Guillemette, Teodor Veres, François A Auger, and Lucie Germain. Alignment of cells and extracellular matrix within tissue-engineered substitutes. *Advances in biomaterials science and biomedical applications*, pages 365–390, 2013.

[8] S. Jonathan Chapman, Rebecca J. Shipley, and Rossa Jawad. Multiscale modeling of fluid transport in tumors. *Bulletin of Mathematical Biology*, 70(8):2334, 2008.

[9] Srikanth R Chary and Rakesh K Jain. Direct measurement of interstitial convection and diffusion of albumin in normal and neoplastic tissues by fluorescence photobleaching. *Proceedings of the National Academy of Sciences*, 86(14):5385–5389, 1989.

[10] Fulai Chen and Li Ren. Application of the finite difference heterogeneous multiscale method to the Richards' equation. *Water Resources Research*, 44(7):W07413, 2008.

[11] Joe Collis, Matthew E Hubbard, and Reuben D O'DEA. A multi-scale analysis of drug transport and response for a multi-phase tumour model. *European Journal of Applied Mathematics*, 28(3):499–534, 2017.

[12] Joseph O. Dada and Pedro Mendes. Multi-scale modelling and simulation in systems biology. *Integrative Biology*, 3(2):86–96, 2011.

[13] Valdemir Garcia Ferreira, Rafael A. B. de Queiroz, G. A. B. Lima, Rafael G. Cuenca, Cassio M. Oishi, João Luiz F. Azevedo, and Sean McKee. A bounded upwinding scheme for computing convection-dominated transport problems. *Computers & Fluids*, 57:208–224, 2012.

[14] Lisa E. Freed, Gordana Vunjak-Novakovic, Robert J. Biron, Dana B. Eagles, Daniel C. Lesnoy, Sandra K. Barlow, and Robert Langer. Biodegradable polymer scaffolds for tissue engineering. *Bio/Technology*, 12(7):689–693, 1994.

[15] K Fushimi and A S Verkman. Low viscosity in the aqueous domain of cell cytoplasm measured by picosecond polarization microfluorimetry. *Journal of Cell Biology*, 112(4):719–725, 1991.

[16] Aaron Z Garza, Sharon B Park, and Remek Kocz. Drug elimination. *StatPearls [Internet]*, 2021.

[17] C. William Gear, James M. Hyman, Panagiotis G Kevrekidid, Ioannis G. Kevrekidis, Olof Runborg, and Constantinos Theodoropoulos. Equation-Free, Coarse-Grained Multiscale Computation: Enabling Mocroscopic Simulators to Perform System-Level Analysis. *Communications in Mathematical Sciences*, 1(4):715–762, 2003.

[18] Xiaobo Gong, Zhaoxin Gong, and Huaxiong Huang. An immersed boundary method for mass transfer across permeable moving interfaces. *Journal of Computational Physics*, 278:148–168, 2014.

[19] Jordi Gonzalez-Molina, Joana Mendonça da Silva, Barry Fuller, and Clare Selden. The extracellular fluid macromolecular composition differentially affects cell-substrate adhesion and cell morphology. *Scientific Reports*, 9:8505, 2019.

[20] Stephanie E. A. Gratton, Patricia A. Ropp, Patrick D. Pohlhaus, J. Christopher Luft, Victoria J. Madden, Mary E. Napier, and Joseph M. DeSimone. The effect of particle design on cellular internalization pathways. *Proceedings of the National Academy of Sciences*, 105(33):11613–11618, 2008.

[21] Carl Henrik Heldin, Kristofer Rubin, Kristian Pietras, and Arne Östman. High interstitial fluid pressure–an obstacle in cancer therapy. *Nature Reviews Cancer*, 4(10):806–813, 2004.

[22] Huaxiong Huang, Kazuyasu Sugiyama, and Shu Takagi. An immersed boundary method for restricted diffusion with permeable interfaces. *Journal of Computational Physics*, 228(15):5317–5322, 2009.

[23] Ke Huang, Rena Boerhan, Changming Liu, and Guoqiang Jiang. Nanoparticles penetrate into the multicellular spheroid-on-chip: Effect of surface charge, protein corona, and exterior flow. *Molecular Pharmaceutics*, 14(12):4618–4627, 2017.

[24] Mohammad Aminul Islam, Sutapa Barua, and Dipak Barua. A multiscale modeling study of particle size effects on the tissue penetration efficacy of drug-delivery nanoparticles. *BMC Systems Biology*, 11(113):806–813, 2017.

[25] Yamir Islam, Andrew G Leach, Jayden Smith, Stefano Pluchino, Christopher R Coxon, Muttuswamy Sivakumaran, James Downing, Amos A Fatokun, Meritxell Teixidò, and Touraj Ehtezazi. Physiological and pathological factors affecting drug delivery to the brain by nanoparticles. *Advanced Science*, 8(11):2002085, 2021.

[26] Ratna S Katiyar and Prateek K Jha. Molecular simulations in drug delivery: Opportunities and challenges. *WIREs Computational Molecular Science*, 8(4):e1358, 2018.

[27] A.R.A. Khaled and K. Vafai. The role of porous media in modeling flow and heat transfer in biological tissues. *International Journal of Heat and Mass Transfer*, 46(26):4989–5003, 2003.

[28] Salman Khan, Binita Dahal, Faraz Siddiqui, Kim J Norville, and Apurwa Karki. Pulmonary spindle cell carcinoma: A rare case report. *Cureus*, 11(5), 2019.

[29] Munju Kim, Robert J Gillies, and Katarzyna A Rejniak. Current advances in mathematical modeling of anti-cancer drug penetration into tumor tissues. *Frontiers in Oncology*, 3:278, 2013.

[30] M. Kojic, M. Milosevic, N. Kojic, K. Kim, M. Ferrari, and A. Ziemys. A multiscale MD-FE model of diffusion in composite media with internal surface interaction based on numerical homogenization procedure. *Computer Methods in Applied Mechanics and Engineering*, 269:123–138, 2014.

[31] M. Kojic, M. Milosevic, N. Kojic, Z. Starosolski, K. Ghaghada, R. Serda, A. Annapragada, M. Ferrari, and A. Ziemys. A multiscale FE model for convective-diffusion drug transport within tumor and large vascular networks. *Computer Methods in Applied Mechanics and Engineering*, 294:100–122, 2015.

[32] Alastair H. Kyle and Andrew I. Minchinton. Measurement of delivery and metabolism of tirapazamine to tumour tissue using the multilayered cell culture model. *Cancer Chemotherapy and Pharmacology*, 43(3):213–220, 1999.

[33] Joseph A Leedale, Jonathan A Kyffin, Amy L Harding, Helen E Colley, Craig Murdoch, Parveen Sharma, Dominic P Williams, Steven D Webb, and Rachel N Bearon. Multiscale modelling of drug transport and metabolism in liver spheroids. *Interface Focus*, 10(2):20190041, 2020.

[34] Albert Leo, Corwin Hansch, and David Elkins. Partition coefficients and their uses. *Chemical Reviews*, 71(6):525–616, 1971.

[35] Richard M Martin, Pipasha N Biswas, Shayne N Freemantle, Gillian L Pearce, and Ronald D Mann. Age and sex distribution of suspected adverse drug reactions to newly marketed drugs in general practice in england: analysis of 48 cohort studies. *British Journal of Clinical Pharmacology*, 46(5):505–511, 1998.

[36] Marilyn N. Martinez. Factors influencing the use and interpretation of animal models in the development of parenteral drug delivery systems. *The AAPS Journal*, 13(4):632–649, 2011.

[37] MATLAB. *R2020a*. The MathWorks Inc., Natick, Massachusetts, 2020.

[38] H.V.R. Mittal and Rajendra K. Ray. Solving immersed interface problems using a new interfacial points-based finite difference approach. *SIAM Journal on Scientific Computing*, 40(3):A1860–A1883, 2018.

[39] Suguru Miyauchi, Shintaro Takeuchi, and Takeo Kajishima. A numerical method for mass transfer by a thin moving membrane with selective permeabilities. *Journal of Computational Physics*, 284:490–504, 2015.

[40] R. D. O'Dea, M. R. Nelson, A. J. El Haj, S. L. Waters, and H. M. Byrne. A multiscale analysis of nutrient transport and biological tissue growth in vitro. *Mathematical Medicine and Biology: A Journal of the IMA*, 32(3):345–366, 2015.

[41] Ewa Paluch and Carl-Philipp Heisenberg. Biology and physics of cell shape changes in development. *Current Biology*, 19(17):R790–R799, 2009.

[42] Suhas V. Patankar. *Numerical heat transfer and fluid flow*. Taylor & Francis, 1980.

[43] Sarah C Pearce, Arwa Al-Jawadi, Kunihiro Kishida, Shiyan Yu, Madeleine Hu, Luke F Fritzky, Karen L Edelblum, Nan Gao, and Ronaldo P Ferraris. Marked differences in tight junction composition and macromolecular permeability among different intestinal cell types. *BMC Biology*, 16(1):1–16, 2018.

[44] Feng Qian, Nicholas Stowe, Erin H Liu, Gerald M Saidel, and Jinming Gao. Quantification of in vivo doxorubicin transport from PLGA millirods in thermoablated rat livers. *Journal of Controlled Release*, 91(1-2):157–166, 2003.

[45] A. Rohatgi. Webplotdigitizer. `https://automeris.io/WebPlotDigitizer`, April, 2019.

[46] Yousef Saad. *Iterative methods for sparse linear systems*, volume 82. SIAM, 2003.

[47] Tracy L. Sandritter, Matthew McLaughlin, Michael Artman, and Jennifer Lowry. The interplay between pharmacokinetics and pharmacodynamics. *Pediatrics in Review*, 38(5):195–206, 2017.

[48] Abhilash Sasidharan, Jim E. Riviere, and Nancy A. Monteiro-Riviere. Gold and silver nanoparticle interactions with human proteins: impact and implications in biocorona formation. *Journal of Materials Chemistry B*, 3(10):2075–2082, 2015.

[49] Trevor R.H. Sherk. Numerical methods for simulating diffusion in cellular media. Master's thesis, Faculty of Science, University of Ontario Institute of Technology, 2011.

[50] Xinghua Shi and Falin Tian. Multiscale modeling and simulation of nano-carriers delivery through biological barriers–A review. *Advanced Theory and Simulations*, 2(1):1800105, 2019.

[51] Lyubov' E. Shimolina, Maria Angeles Izquierdo, Ismael López-Duarte, James A. Bull, Marina V. Shirmanova, Larisa G. Klapshina, Elena V. Zagaynova, and Marina K. Kuimova. Imaging tumor microscopic viscosity in vivo using molecular rotors. *Scientific Reports*, 7:41097, 2017.

[52] Rebecca J. Shipley and S. Jonathan Chapman. Multiscale modelling of fluid and drug transport in vascular tumours. *Bulletin of Mathematical Biology*, 72(6):1464–1491, 2010.

[53] Di Su, Ronghui Ma, Maher Salloum, and Liang Zhu. Multi-scale study of nanoparticle transport and deposition in tissues during an injection process. *Medical & Biological Engineering & Computing*, 48(9):853–863, 2010.

[54] Edward A. Swabb, Wei, and Pietro M. Gullino. Diffusion and convection in normal and neoplastic tissues. *Cancer Research*, 34(10):2814–2822, 1974.

[55] Matteo Taffetani, Carlo de Falco, Raimondo Penta, Davide Ambrosi, and Pasquale Ciarletta. Biomechanical modelling in nanomedicine: multiscale approaches and future challenges. *Archive of Applied Mechanics*, 84(9-11):1627–1645, 2014.

[56] Li Tang, Nathan P. Gabrielson, Fatih M. Uckun, Timothy M. Fan, and Jianjun Cheng. Size-dependent tumor penetration and in vivo efficacy of monodisperse drug–silica nanoconjugates. *Molecular Pharmaceutics*, 10(3):883–892, 2013.

[57] Bernard Testa and Stefanie D Krämer. *The Biochemistry of Drug Metabolism: Principles, Redox Reactions, Hydrolyses*. Wiley, 2010.

[58] James William Thomas. *Numerical partial differential equations: Finite difference methods*, volume 22. Springer-Verlag New York, 1995.

[59] Jonathan K Tunggal, David SM Cowan, Hafsa Shaikh, and Ian F Tannock. Penetration of anticancer drugs through solid tissue: a factor that limits the effectiveness of chemotherapy for solid tumors. *Clinical Cancer Research*, 5(6):1583–1586, 1999.

[60] Xiaolong Wang, Xiaobo Gong, Kazuyasu Sugiyama, Shu Takagi, and Huaxiong Huang. An immersed boundary method for mass transfer through porous biomembranes under large deformations. *Journal of Computational Physics*, page 109444, 2020.

[61] E Weinan and Bjorn Engquist. The heterognous multiscale methods. *Communications in Mathematical Sciences*, 1(1):87–132, 2003.

[62] Brent D Weinberg, Ravi B Patel, Agata A Exner, Gerald M Saidel, and Jinming Gao. Modeling doxorubicin transport to improve intratumoral drug delivery to RF ablated tumors. *Journal of Controlled Release*, 124(1-2):11–19, 2007.

[63] Roe E Wells and Edward W Merrill. Shear rate dependence of the viscosity of whole blood and plasma. *Science*, 133(3455):763–764, 1961.

[64] Michael Welter and Heiko Rieger. Interstitial fluid flow and drug delivery in vascularized tumors: a computational model. *PLoS ONE*, 8(8):e70395, 2013.

[65] Stephen Whitaker. Flow in porous media I: A theoretical derivation of Darcy's law. *Transport in Porous Media*, 1(1):3–25, 1986.

[66] Cliff Wong, Triantafyllos Stylianopoulos, Jian Cui, John Martin, Vikash P. Chauhan, Wen Jiang, Zoran Popović, Rakesh K. Jain, Moungi G. Bawendi, and Dai Fukumura. Multistage nanoparticle delivery system for deep penetration into tumor tissue. *Proceedings of the National Academy of Sciences*, 108(6):2426–2431, 2011.

[67] Nicole J Yang and Marlon J Hinner. Getting across the cell membrane: An overview for small molecules, peptides, and proteins. In *Site-Specific Protein Labeling*, pages 29–53. Springer, 2015.

[68] Xingye Yue and E Weinan. The local microscale problem in the multiscale modeling of strongly heterogeneous media: Effects of boundary conditions and cell size. *Journal of Computational Physics*, 222(2):556–572, 2007.

[69] Shadi Zaheri and Fatemeh Hassanipour. A comprehensive approach to the mathematical modeling of mass transport in biological systems: Fundamental concepts and models. *International Journal of Heat and Mass Transfer*, 158:119777, 2020.

[70] Mostafa Zakariapour, Mohammad Hossein Hamedi, and Nasser Fatouraee. Characteristics of interstitial fluid flow along with blood flow inside a cylindrical tumor: a numerical simulation. *Acta Scientiarum. Technology*, 40, 2018.

[71] Wenbo Zhan, Moath Alamer, and Xiao Yun Xu. Computational modelling of drug delivery to solid tumour: Understanding the interplay between chemotherapeutics and biological system for optimised delivery systems. *Advanced Drug Delivery Reviews*, 132:81–103, 2018.

[72] Wenbo Zhan and Chi-Hwa Wang. Convection enhanced delivery of chemotherapeutic drugs into brain tumour. *Journal of Controlled Release*, 271:74–87, 2018.

PUBLICATIONS

The following research articles are drawn from this thesis work:

1. K. S. Yadav and D. C. Dalal. The heterogeneous multiscale method to study particle size and partitioning effects in drug delivery, *Computers and Mathematics with Applications*, 92:134–148, 2021.

2. K. S. Yadav and D. C. Dalal, Effects of cell permeability on distribution and penetration of drug in biological tissues: A multiscale approach, *Applied Mathematical Modelling*, 108:355–375, 2022.

3. K. S. Yadav and D. C. Dalal, Effects of cell orientation on drug delivery into biological tissues: A computational study, *(Communicated)*.

4. K. S. Yadav and D. C. Dalal, A multiscale computational study of the effects of fluid flow and drug metabolism on drug delivery, *(Communicated)*.

5. K. S. Yadav and D. C. Dalal, Penetration and distribution efficacy of chemotherapeutic drugs in biological tissues, *(Communicated)*.